Density, Temperature and Magnetic Field Measurements in Low Density Plasmas.

Matthew Oliver
St Anne's College
University of Oxford

A thesis submitted for the degree of
Doctor of Philosophy

Hilary 2018

'To be honest Matthew in my limited knowledge of lasers they seem to be broken most of the time.....they are not very robust and certainly not to be relied upon.....anyway have a lovely time and try to find a bit of work to do!!!'
- Jill Oliver

For my family Jill, Andrew, Timmy and Mark.

Acknowledgements

First and foremost; I would like to thank my supervisor Professor Gianluca Gregori for the huge number of opportunities he has given me throughout my PhD. I am sure neither of us expected that I would still be his student seven years after he first began teaching me statistical mechanics. His support, guidance, admonishment and encouragement have been invaluable in producing the work presented here, and, dare I say, it making me the physicist I am today.

I have also been incredibly lucky to have the opportunity to be taught and guided by Professor Thomas White. Working alongside him has taught me an enormous deal about experimental physics. He has also answered the stupid questions I have been too embarrassed to ask Gianluca.

I must also mention goes to Alexandra Rigby, who I have worked alongside on experiments ranging from circuit theory in undergraduate labs to the search for ion acoustic waves at LCLS in california. (Circuit theory in undergraduate labs remains the least comprehensible experiment I have ever attempted.) She also received the questions too stupid for either Gianluca or Tom, and, by this point, those questions were pretty incomprehensible.

Thanks also goes to Archie Bott, Dr Paul Mabey, Dr Pawel Kozlowski, Dr Joe Cross, Dr Shamim Patel, Dr Paul Stubley, Alexander Savin and Dr Laura Chen for the discussions and distractions they have provided over the years. Many a low quality game of worms has been played with the above physicists.

Finally, I must of course thank my family, Jill, Andrew, Timmy and Mark Oliver, for the support and inspiration they provide, almost exclusively without realising it.

Abstract

Low density plasmas are found throughout the known universe. Therefore, accurate diagnostic methods have implications for our understanding of a variety of topics, ranging from star formation to the semi conductor industry.

Low density plasmas are ubiquitous in the material processing industry. However, measurements of the electron temperature and density, two of the most fundamental plasma properties, are not straightforward. In the laboratory, we create a low density, radio frequency, helium plasma with a bi-Maxwellian electron distribution, similar to those found in the semiconductor processing industry. We use optical emission spectroscopy to perform a non invasive measurement of the plasma conditions. We compare this to measurements obtained using a Langmuir probe, a commonly used invasive diagnostic. The optical emission spectroscopy is found to be insensitive to electron density but good agreement is found between the two techniques for values of the temperature of the hot electron component of the bi-Maxwellian.

Plasmas created with high-intensity lasers are able to recreate conditions similar to those found during astrophysical events. This development has led to these conditions being explored in laboratories around the world. An experiment was performed at the Rutherford Appleton Laboratory in Didcot, UK, investigating the properties of supersonic turbulent jets. For the first time a magneto-optic probe was used to measure the magnetic field in a low-density supersonic turbulent plasma. The results were compared to measurements taken using a magnetic-induction probe. Good agreement was found between measurements of the magnetic field strength within the plasma; however, the magnetic power spectra differ. We attribute this to the difference in integration length between the two measurements. Statistical properties of the velocity field are inferred from the magnetic field measurements, which compare favourably to astrophysical observations and hydrodynamic simulations.

Contents

List of Figures

Chapter 1

Introduction

1.1 Introduction

Famously, '99 % of the visible universe is composed of plasma'. With such a large amount of material available, one is spoiled for choice when selecting an area of study. Whilst early man was limited to observing the beauty of plasma emission from the distant stars, today plasma sources are abundant on earth. However, that is not to say astrophysical plasma sources have lost anything of their beauty or their scientific interest. The earliest observations of plasmas appear to have been efforts to discern whether the sun was riding through the sky on a barge or on a chariot [14, 15], a research area that has not generated a publication for so long that presumably the question has been abandoned for being too complicated. More current topics include: the interstellar medium, accretion discs, stars, and the solar wind - all of which are composed of plasma [16]. Closer to earth, the magnetosphere [17], the polar aurora [18] and lightning [19] are all examples of extra-terrestrial plasma. Even if the wonders of nature are not sufficient enough to stir our interest in plasma physics, more practical examples, including nuclear fusion devices [20], plasma televisions and the plasma sources [2] used to etch semiconductors, demonstrate the importance of plasma in our everyday lives. Clearly, even if a person has no interest in plasma physics themselves, they should be glad somebody somewhere does!

What exactly is a plasma? A plasma is a quasi-neutral ionised gas which, as a result of long range interactions, exhibits large-scale collective behaviour. It is this collective behaviour, mediated by electric and magnetic fields, which leads to plasma physics being such a rich area of study. This thesis is principally concerned with experimental methods used to investigate low-density plasmas. Experimental observations or measurements, whether made using a magnetic-induction probe in the laboratory or observing emission from a supernovae a universe away, form the bedrock of modern plasma physics. Experiments are the test bed for existing theories and simulations.

Whilst also providing the observations necessary to inspire new theories. Theories which, in the fullness of time, will once again require testing experimentally.

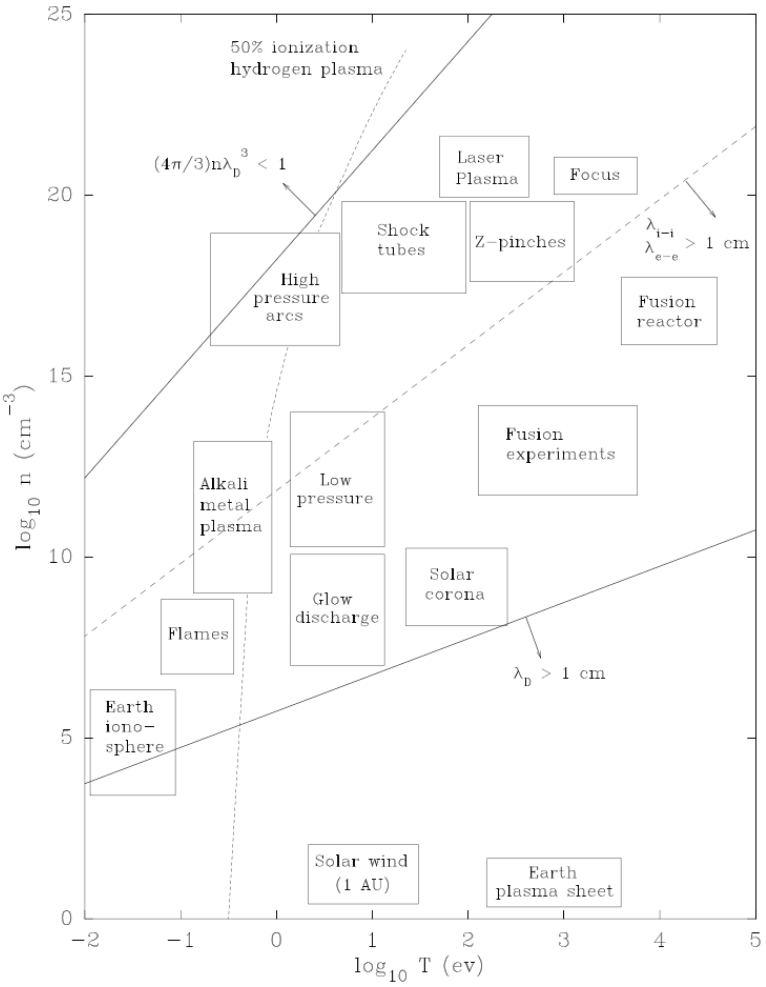

Figure 1.1: A Plasma phase diagram (reproduced from [1])

1.2 Thesis Overview

This thesis begins with a short chapter on fundamental plasma theory focusing on topics that are relevant to the theory and results presented in later chapters. Chapter 2 discusses theory specific to the radio frequency discharge and associated diagnostics. Initially, theoretical models of the discharge are discussed. Next, both

Langmuir probe techniques and optical emission spectroscopy are looked at in detail. This chapter includes a discussion on the ion current collection models used for the data analysis in Chapter 3. Chapter 3 commences with an explanation of the aims of the experiment into electron temperature and density measurements which used optical emission spectroscopy in a helium capacitively coupled radio frequency discharge. The experimental setup is presented, followed by the setup and results of each individual diagnostic. The chapter concludes with a comparison of the results of the two diagnostic methods and suggestions for future work. The results in Chapter 3 can be found in [21].

Chapter 4 introduces diagnostics used during a high power laser experiment into supersonic turbulence. Magnetic field measurements are discussed, and the magnetic induction and magneto-optic probes are introduced. Chapter 5 discusses magnetic field measurements made in a supersonic turbulent plasma. It begins by outlining the importance of supersonic turbulence before explaining the aims of the experiment- mainly to test the magneto-optic probe and to find the exponent of the velocity power spectra in a supersonic turbulent plasma experimentally. A relationship between the exponents of the velocity power spectra and the magnetic power spectra are derived before the experimental setup is presented. The results of each diagnostic are presented and the magnetic fields measured using the two different probes are compared. The inferred values for the exponents of the velocity spectra are discussed alongside observed values from the literature. The chapter again concludes with suggestions for future experiments into both the magneto-optic probe and supersonic turbulence. Results from this experiment can be found in both [11] and [8]. In Chapter 6 the conclusions of the thesis are summarised for completeness.

1.3 Fundamental Plasma Theory

1.3.1 The Debye Length

If a plasma is exposed to an electric field the the charged particles will redistribute themselves, effectively shielding the field. The screening is mainly performed by the more mobile electrons. How effectively the plasma can shield the electric field is important as approximations like quasi-neutrality will only hold at scales greater than the screening length. Imagine placing a single positive test charge into a neutral plasma with temperature T. The number density of the electrons inside the plasma a distance r from the positive test charge is given by the Boltzmann relationship [22]

$$n_e = n_0 \exp\left(\frac{q_e \phi(r)}{k_b T}\right), \tag{1.1}$$

where n_0 is the equilibrium number density, n_e is the electron density, q_e is the electron charge, $\phi(r)$ is the electrostatic potential at the point r and k_b is the Boltzman constant. Similarly the ion number density is given by

$$n_i = n_0 \exp\left(\frac{-q_e \phi(r)}{k_b T}\right). \tag{1.2}$$

In the case that the thermal energy is much larger than the electrostatic energy the charge excess ρ_e due to the test charge is

$$\rho_e = q_e(n_i - n_e) = -2\left(\frac{q_e^2 \phi}{k_b T}\right) n_0. \tag{1.3}$$

Inserting Equation (1.3) into Poissons equation, $\nabla^2 \phi = -\rho_e/\epsilon_0$, gives

$$\phi = \frac{q_e}{4\pi\epsilon_0 r} \exp\left(\frac{-r}{\lambda_D}\right), \tag{1.4}$$

where λ_d, the Debye length [22] is defined as

$$\lambda_D = \sqrt{\frac{\epsilon_0 k_b T}{2e^2 n_e}} \tag{1.5}$$

for $T_e = T_i$. Quasi-neutrality and the fluid approximations only apply at scales where $\lambda_D >> n_0^{-1/3}$ and thus the shielding is effective. The concept is useful as it gives an indication of the importance of collective behaviour within a plasma. The assumption that the plasma is quasi-neutral, ($n_e \sim n_i$) appears throughout plasma physics, it will be assumed several times throughout the remainder of this thesis.

1.3.2 The Plasma Frequency

Consider a cold, collision-less, uniform plasma where all of the electrons are displaced a distance δx from their initial position. As the ion mass is much greater than the electron mass the ions will remain stationary on short timescales. The electric field created by the charge separation will act to pull the electrons back towards the ions. The electron cloud overshoots its starting position leading to an oscillation within the plasma. The oscillation is called a Langmuir wave, and the frequency of oscillation is referred to as the plasma frequency denoted, ω_{pe} [22].The plasma frequency can be derived by considering a Gaussian surface within the plasma

$$EA = \frac{n_e q_e A \delta x}{\epsilon_0} \tag{1.6}$$

where E is the electric field, A is the area of the plasma surface perpendicular to δx and ϵ_0 is the permittivity of free space in a vacuum. Combining Equation (1.6) with Newton's second law gives

$$F = m_e \frac{d^2 x}{dt^2} = -q_e E = -\frac{n_e q_e^2}{\epsilon_0} \delta x, \tag{1.7}$$

where F is the force on the electrons and m_e is the electron rest mass. This equation describes a simple harmonic oscillator with a frequency

$$\omega_p = \sqrt{\frac{n_e e^2}{\epsilon_0 m_e}}. \tag{1.8}$$

This is the simplest example of wave behaviour within a plasma.

1.3.3 Electromagnetic Waves

One of the principal characteristics of a plasma is its ability to support a number of different types of wave. The Langmuir wave (with $T_e = 0$), whose frequency was derived above, is an example of an electrostatic wave, a wave in which the displacement current is equal and opposite to the conduction current. Electromagnetic waves can be an important method of energy transfer into a plasma. The dispersion relationship that describes the propagation of transverse plane waves is now outlined, starting from the differential form of Maxwell's equations [22]:

$$\nabla \times \mathbf{E} = -\frac{\partial \mathbf{B}}{\partial t}, \tag{1.9}$$

$$\nabla \times \mathbf{B} = \mu_0 \left(\mathbf{j} + \epsilon_0 \frac{\partial \mathbf{E}}{\partial t} \right), \tag{1.10}$$

$$\epsilon_0 \nabla \cdot \mathbf{E} = \rho, \tag{1.11}$$

$$\nabla \cdot \mathbf{B} = 0. \tag{1.12}$$

Where $\mathbf{B}$ is the magnetic field, μ_0 is the permeability of free space and $\mathbf{j}$ is the conduction current. We limit our analysis to plane wave solutions, thus allowing the electric and magnetic fields to be written as [2]

$$\mathbf{E} = \mathbf{E_0} e^{i(\omega t - \mathbf{k} \cdot \mathbf{r})}, \tag{1.13}$$

$$\mathbf{B} = \mathbf{B_0} e^{i(\omega t - \mathbf{k}\cdot\mathbf{r})}, \tag{1.14}$$

where ω is the time oscillating frequency and $\mathbf{k}$ is the wavenumber. Inserting these expressions back into Maxwell's equations allows the differential equations to be written in terms of the frequency, ω, and wavenumber, k

$$\begin{aligned} -i\mathbf{k} \times \mathbf{E_0} &= -i\omega \mathbf{B_0}, & (1.15)\\ -i\mathbf{k} \times \mathbf{B_0} &= \mu_0 \Big(\mathbf{j} + \epsilon_0 i\omega \mathbf{E_0} \Big), & (1.16)\\ -i\epsilon_0 \mathbf{k} \cdot \mathbf{E_0} &= \rho, & (1.17)\\ -i\mathbf{k} \cdot \mathbf{B_0} &= 0. & (1.18) \end{aligned}$$

Equation (1.16) is rewritten in terms of the dielectric constant (ϵ_p)

$$-i\mathbf{k} \times \mathbf{B_0} = i\omega \mu_0 \epsilon_p \mathbf{E_0}, \tag{1.19}$$

which depends on the transport properties of the plasma. Equations (1.15) and (1.16) can then be combined to give

$$\mathbf{k} \times (\mathbf{k} \times \mathbf{E_0}) = -\omega^2 \epsilon_p \mu_0 \mathbf{E_0}. \tag{1.20}$$

For a transverse wave $\mathbf{k} \cdot \mathbf{E} = 0$ and the dispersion relationship simplifies to

$$k^2 = \frac{\epsilon_p \omega^2}{\epsilon_0 c^2}. \tag{1.21}$$

This is the general dispersion relationship for transverse plane waves within a plasma. Precisely which waves the plasma is able to support then depends on the precise form of the plasma dielectric constant, for example Whistler modes and Alfvén waves [23] are common examples of transverse waves in a magnetised plasma. However, the next

section focuses on the dielectric constant of a plasma in a background gas, a situation common in low density plasma sources.

1.3.4 The Plasma Dielectric Constant

The dielectric constant relating the electric field to the current in the plasma is derived from Newton's second law [2, 24]. For a cold, uniform plasma in a background gas with an electric field pointing in the x direction ($\mathbf{E} = E\hat{\mathbf{x}}$), Newton's second law gives

$$m_e \frac{du_x}{dt} = -q_e E - m_e \nu_m u_x, \tag{1.22}$$

where ν_m is the electron neutral collision frequency and u_x is the electron velocity in the x direction. If the plasma is driven by a small amplitude oscillating electric field along the x axis E_x with a frequency ω

$$E_x = \mathrm{Re}(\tilde{E}_x e^{j\omega t}) \tag{1.23}$$

where $\tilde{E}_x$ is the complex amplitude of the field E_x. The corresponding velocity is written as

$$u_x = \mathrm{Re}(\tilde{u}_x e^{j\omega t}). \tag{1.24}$$

where $\tilde{u}_x$ is the complex amplitude of the velocity u_x. Combining Equations (1.23) and (1.24) the amplitude of the complex velocity is given in terms of the amplitude of the complex electric field as

$$\tilde{u}_x = -\frac{q_e}{m_e} \frac{1}{j\omega + \nu_m} \tilde{E}. \tag{1.25}$$

The total current within the plasma J is the sum of the displacement current and the conduction current

$$J = \epsilon_0 \frac{\partial E}{\partial t} - q_e n_e u_x. \tag{1.26}$$

The total complex current is therefore

$$\tilde{J} = \epsilon_0 \frac{\partial \tilde{E}}{\partial t} - q_e n_e \tilde{u}_x. \tag{1.27}$$

Which upon substitution of Equation (1.25) leads to an effective plasma dielectric constant

$$\epsilon_p = \epsilon_0 \Big(1 - \frac{\omega_p^2}{\omega(\omega - j\nu_m)} \Big). \tag{1.28}$$

From this we define the plasma conductivity, σ_p as

$$\sigma_p = \frac{\epsilon_0 \omega_p^2}{(j\omega + \nu_m)} \tag{1.29}$$

where $\tilde{J_T} = (\sigma_p + j\omega\epsilon_0)\tilde{E}$. In the limit that the frequency of the applied field is much larger than the collision frequency the dielectric constant simplifies to that of an ideal plasma

$$\epsilon_p = \epsilon_0 \Big(1 - \frac{\omega_p^2}{\omega^2} \Big). \tag{1.30}$$

Inserting Equation (1.30) into the dispersion relationship, Equation (1.31) gives

$$\omega^2 = \omega_p^2 + c^2 k^2, \tag{1.31}$$

the dispersion relationship for an ideal plasma. This shows that waves with frequencies less than the plasma frequency, (in the case where $\omega >> \nu_m$), cannot propagate within the plasma. This generally applies to radio frequency waves in low density plasma discharges. As the plasma frequency is a function of the electron density a

critical density $n_c = \omega^2 \epsilon_0 m_e / q_e^2$ can be defined when $\omega = \omega_p$ and waves can no longer propagate. A plasma described by the above equations can then be modelled as a capacitor, with capacitance $C_p = \epsilon_p A/l$, where A is the cross section of the plasma and l is the length along the x direction [2].

1.4 Magnetohydrodynamics

1.4.1 The Equations of Magnetohydrodynamics

The large number of particles inside a typical plasma make modelling the behaviour of each individual particle virtually impossible. Fortunately, in a large number of cases plasma behaviour can be explained effectively using a continuum fluid model. A model that can be applied on length scales larger than the mean free path. In a plasma the particle collisions are additionally mediated by electric and magnetic fields. Magnetohydrodynamics (MHD) [25,26] often treats the plasma as a single conducting fluid, this approximation leans heavily on the high electron mobility within a plasma. The mobile electrons cancel out any applied fields and carry current through the plasma. MHD is applicable if the plasma is large enough to contain many ions, (the continuum hypothesis) and the time scales of interest are longer than the electron or ion oscillation times, $\omega \ll \omega_{ci}$, where ω_{ci} is the ion cyclotron frequency. MHD is expressed as a series of equations describing the evolution of a fluid element. The continuity equation describes the conservation of mass and is given by

$$\frac{\partial \rho}{\partial t} + \nabla \cdot (\rho \mathbf{u}) = 0, \tag{1.32}$$

where ρ is the mass density and $\mathbf{u}$ is the velocity of the Lagrangian fluid parcel. Similarly, momentum conservation for the fluid parcel produces the following equation

$$\rho\Big(\frac{\partial}{\partial t} + \mathbf{u}\cdot\nabla\Big)\mathbf{u} = -\nabla p + \frac{1}{\mu_0}(\nabla\times\mathbf{B})\times\mathbf{B} + \theta\nabla^2\mathbf{u}, \tag{1.33}$$

where p is the fluid pressure, $\mathbf{B}$ is the magnetic field in the fluid and θ is the dynamic viscosity. The induction equation describes the evolution of the magnetic field and is given by

$$\frac{\partial\mathbf{B}}{\partial t} = \nabla\times(\mathbf{u}\times\mathbf{B}) + \eta\nabla^2\mathbf{B}. \tag{1.34}$$

for a constant magnetic diffusivity, η. Finally conservation of energy requires

$$\rho\Big(\frac{\partial}{\partial t} + \mathbf{u}\cdot\nabla\Big)\epsilon = -\nabla\cdot\mathbf{q} + \frac{\eta}{\mu_0}|\nabla\times\mathbf{B}|^2 + \theta\phi, \tag{1.35}$$

where ϵ is the internal energy of the fluid parcel, $\mathbf{q}$ is the heat flux and ϕ is the dissipation function, the rate at which mechanical energy is converted into heat. The heat flux can be written in terms of the plasma temperature gradient, $\mathbf{q} = -\kappa_T\nabla T$, where T is the temperature and κ_T is the heat diffusion coefficient.

1.4.2 The Invariance of the Magnetohydrodynamic Equations

In 1999 Ryutov formalised that a necessary but not sufficient condition for two hydrodynamic systems to be dynamically similar is that they need to share the same dimensionless parameter $R_y = U\sqrt{\rho^*/P}$ [27,28], where U is the characteristic velocity scale of the system, ρ^* is a characteristic mass density of the system and P is the characteristic pressure of the system. R_y is in effect the Mach number under idealised conditions (the system can be modelled by an ideal fluid). This is the similarity criteria for an inviscid fluid with zero thermal conductivity. Furthermore, Equations

(1.32) to (1.35) can be rewritten in a scale invariant form. Each variable, i.e $\mathbf{u}$ can be rewritten in terms of a dimensional and a dimensionless part, $\mathbf{u} = \tilde{\mathbf{u}}U$ where $\tilde{\mathbf{u}}$ is dimensionless [27, 28]. The momentum equation (1.33), can be rewritten in terms of the dimensionless Reynolds number

$$R_e = \frac{UL}{\nu} \tag{1.36}$$

where L is the characteristic length scale of the system and $\nu = \theta/\rho$ is the kinematic viscosity. R_e represents the ratio of inertial forces to viscous forces. On scales at which R_e is large, one assumes viscous forces can be ignored, for instance energy will not be dissipated due to viscosity at large R_e. The induction equation, (Equation 1.34) can be written in terms of the dimensionless parameter R_m, the magnetic Reynolds number

$$R_m = \frac{UL}{\eta}. \tag{1.37}$$

R_m is the ratio of magnetic induction to magnetic diffusivity. At low R_m the magnetic field diffuses out of the plasma more swiftly than it is advected. The conservation of energy (Equation (1.35)) can also be rewritten in terms of a dimensionless parameters. This introduces the new dimensionless variable the Peclet number

$$P_e = \frac{UL}{\chi\tau}. \tag{1.38}$$

where $\chi = \kappa_T/\rho$ is the kinematic thermal diffusivity and τ is the temperature scale. The Peclet number is the ratio of advective heat transport over the diffusive heat transport. Writing the MHD equations in terms of these dimensionless variables illustrates that the systems with the same R_e, R_m and P_e have dynamically similar behaviour (assuming the evolution of the system is described by the MHD equations). However, identical values for the dimensionless variable don't need to be achieved for

dynamic similarity. To see this consider the induction equation rewritten in a non-dimensional form

$$\frac{\partial \mathbf{B}^*}{\partial t^*} = \nabla \times (\mathbf{u}^* \times \mathbf{B}^*) + \frac{1}{R_m}\nabla^2 \mathbf{B}^*. \tag{1.39}$$

where $\mathbf{B}^* = \mathbf{B}/U\sqrt{\mu_0 \rho}$ and $t^* = tU/L$. If R_m is very large then the last term in Equation (1.39) is ~ 0 even if the exact values of R_m differ by orders of magnitude. The principles of scaling underpin the idea of laboratory astrophysics. This will be considered further in Section 1.4.4.

1.4.3 Plasma Turbulence

A physical understanding of turbulence is important in fields as disparate as aeronautical engineering and astrophysics [29]. Richard P. Feynman went so far as to claim, 'turbulence is the most important unsolved problem of classical physics'. Turbulence occurs in plasmas (and fluids) with large Reynolds numbers [30], $R_e \sim 10^3$, at lower Reynolds numbers turbulence is suppressed by viscous dissipation. The term turbulence refers to a plasma with an irregular and chaotic flow, it is often pictured physically as a large number of superimposed vortices. The most successful theory for incompressible (subsonic) turbulence is Kolmogorov's theory for freely decaying, fully developed turbulence [31]. The turbulent fluid is imagined as a series of fluid vortices or 'eddies' with sizes between the outer-scale l (the size of the largest eddies) and the Kolmogorov or dissipation scale η_k (the size of the smallest eddies). At these micro scales energy begins to be dissipated through viscous processes as $R_e \sim 1$. However at scales $> \eta_k$ energy cannot be lost in this manner. This leads to the picture of a turbulent cascade where energy 'cascades' down continuously through eddies of decreasing size. In this model the kinetic energy ΔE contained in eddies with inverse length scales between k_1 and k_2 can be described as

$$\Delta E = \int_{k_1}^{k_2} E(k)dk \tag{1.40}$$

where $E(k)$ is the one dimensional energy spectra and $k = 2\pi/l$, (where l is a length scale). One of the great successes of Kolmogorov's theory is the prediction for the power exponent of the one dimensional energy spectra $E(k) \sim k^{-\frac{5}{3}}$. Although variables, such as the instantaneous velocity, can appear to vary at random in a turbulent flow the statistical properties of turbulence are highly reproducible [29]. Thus turbulence is generally explored through its statistical properties. This will be discussed in detail in Chapter 5.

1.4.4 Laboratory Astrophysics

Studying astrophysical plasmas experimentally was first suggested by Dawson in 1964 [32]. Early experimental work focused on blast waves [33], electrostatic shocks [34] and supernovae [35, 36]. Clearly, recreating the the exact situations found in space in the laboratory is unfeasible due to the large scales synonymous with astrophysics. However recreating specific physical processes and analogous plasma dynamics can be achieved [37], as discussed in Section 1.4.2. Ryutov argued that the two systems must evolve according to the same set of equations, in particular the MHD equations set out in Section 1.4.1. As mentioned previously if R_y, R_e, P_e and R_m are similar for two systems they can be described by the same equations for arbitrary U, L, ν and η. In practice, experiments produce similar dynamical behaviour by forcing the scaling parameters to have appropriate orders of magnitude. For instance, above a Reynolds number of $R_e \sim 10^4$ a fluid is expected to be fully turbulent. If it is then, compared to a fluid with a Reynolds number $R_e \sim 10^7$, the behaviour of the two systems will share distinct features. To develop an experiment to investigate an astrophysical plasma in general the boundary conditions of the two situations must

also be considered. In laser experiments focused on turbulence, interest generally lies in fully developed turbulence [29]. Fully developed turbulence has evolved to a point where its behaviour is assumed to be independent of the initial conditions [29]. This is beneficial when comparing laboratory experiments to astrophysical objects. Many laboratory experiments have been performed investigating magnetic fields in subsonic turbulence [38, 39]. However, thus far, the experimental work on supersonic turbulence is limited to those in close proximity to boundary layers, for example in the aeronautical industry [40].

1.5 High Power Lasers

The first laser was invented in 1960 by Theodor Maiman, though the theoretical foundations were laid by a number of earlier competing scientists [41]. Maiman's laser operated by pumping a synthetic crystal using solid state flash lamps. Over the following five decades laser use has increased spread rapidly. Technological advantages such as Q-switching, mode locking and chirped pulse amplification [42–45] have allowed lasers to become ubiquitous in modern society, from bar-code scanners in supermarkets with powers ~ 1 mW to high power lasers at international facilities with output powers up to ~ 1 PW. Lasers now also contribute to discovery science where they have opened up whole new regions of phase space for exploration. Several high power laser facilities are now open to scientists from around the world including NIF (the National Ignition Facility), LULI (the Laboratory for the Utilization of Intense Lasers), JLF (the Jupiter Laser Facility) and RAL (the Rutherford Appleton laboratory). The experiments referred to in Chapters 4 and 5 were carried out at the Vulcan Laser Facility at the Rutherford Appleton Laboratory near Didcot. The Vulcan laser facility hosts two experimental areas one of which, the Vulcan Petawatt is a single high power beam line whilst the other 'target area west' comprises of eight in-

dividual beam lines, ideally suited to laboratory astrophysics experiments on plasma turbulence.

1.6 Laser Target Interactions

When a high energy laser impacts on a target foil a plasma is created at the incident surface. At laser intensities $\sim\ 5 \times 10^{14}$ Wcm^{-2}, the laser intensity used during the experiments outlined in Chapter 5, the majority of the absorbed laser energy is deposited within this plasma at electron densities below the critical density. At $I_L \sim\ 5 \times 10^{14}$ Wcm^{-2} there are three principal mechanisms for the laser energy to be absorbed by the target; inverse bremsstrahlung, resonant absorption and absorption due to ion acoustic turbulence, each of which will be described briefly below following [46, 47]. Which of the three mechanisms dominates depends on the specific target geometry and material.

1.6.1 Inverse Bremsstrahlung Absorption

As electrons oscillate in the electric field of the laser, momentum changing collisions with ions convert laser energy into thermal energy [48]. An approximation for the energy damping rate of the laser can be found by equating the kinetic energy gained by the oscillating electrons to the rate of energy loss of the beam

$$\nu_E\left(\frac{E_L^2}{8\pi}\right) = \nu_{ei}\left[\frac{n_e}{2} m_e \left(\frac{eE_L}{m_e \omega_L}\right)^2\right], \tag{1.41}$$

where ν_E is the rate of energy loss from the beam, E_L is the electric field of the beam, ν_{ei} is the rate of energy loss for an electron oscillating in the field E_L and ω_L is the frequency of the oscillating field. This equation can be simplified considerably to give the energy damping rate of the laser

$$\nu_E = \left(\frac{n_e}{n_c}\right)\nu_{ei}. \tag{1.42}$$

To find how the damping rate scales with the temperature and density of the coronal plasma an expression must be found for the electron-ion collision frequency. The collision frequency can be defined as as

$$\nu_{ei} = n_i \sigma v_{te}, \tag{1.43}$$

where σ is the collision cross section and v_{te} is the thermal velocity of the electrons [46]. The collision cross section is defined as $\sigma = \pi b^2$ where b is the distance of closest approach to the found by considering the conservation of energy

$$\frac{Ze^2}{b} = \frac{1}{2} m_e v_{te}^2, \tag{1.44}$$

where Z is the mean ion charge. Combining Equations (1.42) and (1.44) the damping rate scales as

$$\nu_E \propto \frac{Z n_e^2}{n_c T_e^{\frac{3}{2}}}. \tag{1.45}$$

This demonstrates that at low laser intensities, short laser wavelengths, and long laser pulses are optimal for inverse bremsstrahlung.

1.6.2 Resonance Absorption

A laser beam can excite a Langmuir wave in the coronal plasma if a component of the electric field oscillates in a direction which is parallel to the electron density gradient. Damping of the plasma oscillation then converts energy from the electric field into thermal energy. To see how this occurs consider Maxwell's equation when $\rho_e = 0$

$$\nabla \cdot (\epsilon_p \mathbf{E}) = 0, \tag{1.46}$$

where ϵ_p is given by

$$\epsilon_p = 1 - \frac{\omega_p^2}{\omega_L^2} = 1 - \frac{n_e}{n_c}, \tag{1.47}$$

where ω_L is the laser frequency. The oscillating electric field can create a charge density perturbation in the plasma. Expanding Equation (1.46) and substituting in Equation (1.47) gives

$$\nabla \cdot \mathbf{E} = \frac{1}{\epsilon_p n_c} \mathbf{E} \cdot (\nabla n_e). \tag{1.48}$$

If $\epsilon_p = 0$, ($\omega_L = \omega_p$) and $\mathbf{E} \cdot (\nabla n_e) \neq 0$ a resonance occurs which is able to drive a large electron plasma oscillation at the critical surface. The electric field of the laser must tunnel from the turning point to the critical surface in order to drive the Langmuir wave. As the turning point is given by $n_e = n_c \cos^2(\theta)$ the strength of resonant absorption is strongly dependent on the angle of incidence to the normal, θ. If theta is too large the electric field must tunnel a large distance and the Langmuir wave is therefore weakly driven, if θ is too small the component of the electric field parallel to the density gradient is small meaning the wave is again, weakly driven. For a density perturbation normal to the critical surface the optimal angle θ_b can be shown to be $\sin(\theta_b) \sim 0.8(c/\omega_L L)^{1/3}$ where L is the density scale length of the plasma. This shows that resonant absorption is depends on the angle of incidence, the laser polarisation and the plasma density scale length.

1.6.3 Absorption due to Ion Acoustic Turbulence

In the 1970's it was noticed that the coupling efficiency of laser light into a target could not be explained by resonant absorption and inverse bremsstrahlung alone. The elevated absorption was attributed to ion acoustic turbulence created within the target [49]. The energy of the incident laser beam causes a flux of thermal electrons to flow into the plasma. As charge neutrality must be maintained, a return current of slow electrons must flow back towards the laser. This return current excites ion acoustic waves within the plasma, enhancing laser absorption [50]. Ion acoustic absorption is most effective in the underdense plasma where the length scales are expected to be large [51] and therefore can act alongside other absorption mechanisms, increasing the overall absorption.

1.7 Role of the author

Chapters 1, 2 and 4 contain mainly experimental and theoretical work from pre-existing literature which the author of this thesis has relied upon. The work in Chapters 3 and 5 was mainly performed by the author with the help and guidance of others.

The radio frequency discharge used in Chapter 3 was constructed mainly by Dr Anthony Dyson with help from the author. All diagnostics and analysis discussed in Chapter 3 were set up and analysed by the author with guidance from Professor Gianluca Gregori.

The experiment described in Chapter 5 was conceived by Professor Gianluca Gregori and Dr Thomas White. The experiment was performed at the Rutherford Appleton laboratory with the support of the scientists and engineers thereof. The author was part of the experimental team alongside Dr Paul Mabey, Dr Marina

Kuhn-Kauffeidt and Leo Dohl which was led by Dr Thomas White. The magnetic - induction probe was built by Adam Baird and the data used for the calibration was taken by Dr Jena Meinecke. The theory linking the measured magnetic spectra to the velocity power spectra was derived by Professor Gianluca Gregori, Professor Alexander Schekocholin, Dr Thomas White and Archie Bott. The analysis of the experimental results were performed by the author with help and guidance from both Professor Gianluca Gregori and Dr Thomas White.

1.8 Summary

In this chapter some of the most basic aspects of plasma physics were discussed. The Debye length and plasma frequency were introduced, both of which will appear several times throughout the remainder of this thesis. The propagation of electromagnetic waves in a plasma was discussed and the dielectric constant of a plasma was introduced. In both the radio frequency plasma source and laser produced plasmas energy is deposited within the plasma due to interactions between electromagnetic waves and the plasma itself. Therefore the ideas initially presented in Section 1.3.3 and 1.3.4 appear again in Sections 1.6 and 2.1.2. Section 1.4.1 introduced the fluid description of a plasma, particularly relevant to the work presented in Chapter 5 on plasma turbulence. The scale invariance of the magnetohydrodynamic equations was explained leading to an introduction to laboratory astrophysics. The theoretical part of this chapter closed with an overview of the different laser energy absorption mechanisms again relevant to the experiment presented in chapter 5. Finally the role of the author in the work presented in this thesis was stated.

Chapter 2

Radio Frequency Plasma Sources and Diagnostic Methods

2.1 The Radio Frequency Discharge

Radio frequency (RF) plasma sources are widely used for etching in the processing industry and have therefore been of widespread interest throughout the past thirty years [2, 52–54]. To achieve the desired range of processing conditions, (electron densities $\sim 10^9 - 10^{12}$ cm^{-3}, electron temperatures $\sim$ 1 - 10 eV [2]), several different discharge operating regimes are required. These operating regimes rely on a variety of different physical mechanisms to sustain the plasma [2]. RF plasma devices include high density inductive and helical sources as well as low to moderate density capacitive coupled sources [4, 5, 55–57]. Here the focus is placed solely on capacitively coupled sources (as used in the experiments described in Chapter 3) [2,3,58,59]. Even capacitively coupled RF discharges have different operating modes, depending on the pressure, applied voltage and physical dimensions of the plasma source. Initially a brief outline of the 'α mode' is presented. This is the standard mode of operation which is discussed in detail in several text books [2, 53]. The later part of this section outlines the transition to the γ mode, the mode of operation in which the experiments are performed [3, 58].

Figure 2.1 (reproduced from reference [2]) shows a schematic diagram of the radio frequency discharge. An oscillating current flows between the two plates separated by a distance, d. Between the plates there exists a neutral helium gas with number density, n_g. When a sufficiently large alternating current is applied across the plates a plasma will form. Some electrons oscillating in the electric field near to the electrodes will be lost to the electrodes. Due to their larger inertia, and therefore smaller velocity, fewer ions than electrons will be lost from the system to the electrodes [2]. Therefore oscillating sheath regions with widths $s_a(t)$ and $s_b(t)$ are created parallel to both electrodes where the ion density is greater than the electron density. Heuristically one can imagine a stationary volume of ions sitting between the two electrodes

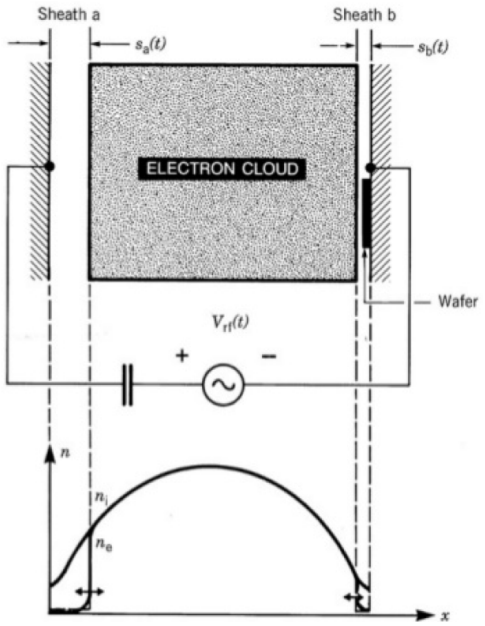

Figure 2.1: A schematic of a Radio frequency discharge (copied from reference [2]). An oscillating current is applied across the two electrodes leading to the formation of two sheaths. Between the two sheaths an electron cloud oscillates in the applied potential. The electron and ion density between the plates are plotted at the bottom of the figure. Within the sheath the electron density is lower than ion density due to the higher electron mobility.

whilst a slightly narrower electron cloud oscillates between them. The potential across the sheaths acts to confine the plasma. The width of the sheath oscillates between some maximum width, $s(t) = s_m$, normally ~ 1 cm and $s(t) = 0$. When the sheath has collapsed, $s(t) = 0$, there is no confining potential and more electrons are lost from the system to the electrodes. The region between the two oscillating sheaths is referred to as the bulk plasma. The bulk plasma is considered quasi-neutral with the ion density, n_i similar to the electron density, n_e and the potential within the bulk plasma is small. Only a small fraction of the neutrals between the electrodes become ionized, $\frac{n_e}{n_g} < 10^{-5}$ [2]. As the electrons within the bulk plasma oscillate, collisions with neutrals randomize some fraction of the electron motion heating the electrons to a temperature, T_e. Due to the large mass difference between the electrons and the neutrals/ ions the transfer of kinetic energy between them is inefficient. Therefore

the electron temperature is typically much greater than the ion temperature T_i or the neutral temperature, T_n. Due to the large neutral fraction and the highly efficient energy transfer between the ions and neutrals (as $M_i \sim M_n$), the ions remain at approximately the neutral temperature. As the neutrals generally remain close to room temperature, this leads to $T_i \sim T_n \sim 0.03$ eV.

A convenient set of control parameters; the driving current I, the driving frequency ω, the neutral number density n_g, and the electrode separation d, can theoretically be chosen to define the plasma parameters and sheath width of the discharge. Our experiments studied the time-averaged properties near the centre of the bulk plasma and therefore precise knowledge of the sheath conditions, which are difficult to obtain, were not required. The discharge used throughout the experiments was similar to that of Godyak [60] and operated in the γ mode, the mode of operation where the ionization is majoritatively due to high energy secondary electrons accelerated across the sheath. The similarity of the discharges is confirmed by the plasma parameters measured using the Langmuir probe.

2.1.1 Non Uniform Discharge Model

A realistic discharge model must be simulated computationally [54, 61–63]. A principal part of any model is the ionization balance. In simple cases this alone is enough to estimate the temperature within the RF discharge [2]. Therefore this section describes a simple model outlining the general procedure for deriving the plasma parameters theoretically. A very similar approach is used in relation to the γ mode, Section 2.1.3. Information for a variety of cases can be found in [2].

Consider the steady state diffusion equation within the bulk plasma. If the dis-

charge radius is much greater than the distance between the electrodes, $r_0 \gg d$

$$-D_a \frac{d^2 n(x)}{dx^2} = v_{iz} n(x) \tag{2.1}$$

where x is the distance from the discharge centre, D_a is the ambipolar diffusion from the bulk plasma to the electrodes, $n(x)$ is the spatially dependent plasma density and v_{iz} is the ionisation rate, the number of ionisations per second that the incident electron causes in the target population. Here, ionisation is assumed to be proportional to the electron density and the ionisation rate is assumed constant across the discharge. This equates to the assumption that the electron temperature is uniform throughout the discharge. The ambipolar diffusion coefficient is given by [2]

$$D_a \approx (1 + \frac{T_e}{T_i}) D_i, \tag{2.2}$$

where T_e is the electron temperature, T_i is the ion temperature and D_i is the ion diffusion coefficient. In a symmetric discharge with $n(\pm d/2) = 0$ with constant diffusion D_a, the solution has the form

$$n = n_0 \cos(\beta x) \tag{2.3}$$

where $\beta = (v_{iz}/D_a)^{\frac{1}{2}}$. The flux, $\Gamma(x)$, is then given by

$$\Gamma(x) = -D_a \frac{dn(x)}{dx} = D_a n_0 \beta \sin(\beta x). \tag{2.4}$$

The flux of the ions and electrons must be the same for the plasma to remain quasi neutral. In a symmetric discharge where the plasma density is zero at the electrodes the boundary condition $n(\pm d/2) = 0$ gives $\beta = \pi/d$, leading to a solution which is not self consistent. However as D_a and v_{iz} are both functions of electron temperature, solutions can be found to give an estimate for T_e. To find the density of the bulk

plasma the conservation of energy is considered. As the bulk plasma remains quasi-neutral the diffusion is ambipolar. Therefore for each ion lost from the system an electron is also removed. The total energy of an electron-ion pair leaving the system can be written as

$$\epsilon_T = \epsilon_c + 2T_e + \epsilon_i. \tag{2.5}$$

Here ϵ_c is the collisional energy needed to ionize a neutral within the discharge, $2T_e$ is the average kinetic energy lost per Maxwellian electron diffusing out from the plasma and ϵ_i is the mean kinetic energy lost per ion. The kinetic energy of the ions depends strongly on the sheath potential which can vary greatly depending on the exact discharge setup. In the steady state the total power leaving the discharge can be written as

$$S_{abs} = 2e\epsilon_T\Gamma_i(\frac{l}{2}), \tag{2.6}$$

where the factor of 2 accounts for the flux of ions out of the discharge at both $\pm\frac{l}{2}$. Substituting Equation (2.4) into Equation (2.6) gives an expression for the bulk plasma density

$$n = \frac{S_{abs}}{2\pi D_a e\epsilon_T}. \tag{2.7}$$

While this derivation gives the basic outline of the method used to create an analytical model of the discharge, the majority of the physical processes are hidden in the constants. In Equation (2.1) the ionisation was assumed to be constant throughout the discharge. Whilst this may be a reasonable assumption for a low pressure discharge sustained by Ohmic heating (Section 2.1.2), it is rarely compatible with

stochastic heating or a discharge sustained in the γ mode. The absolute power reaching the bulk plasma, S_{abs}, depends strongly on the heating mechanism. The two most important heating mechanisms controlling the electron temperature in capacitively coupled discharges are outlined in the following section.

2.1.2 Heating Mechanisms

To illustrates the physical processes involved, the heating mechanisms below are derived for the case of a discharge with a uniform ion density.

Ohmic Heating

Ohmic heating is due to collisions between the oscillating electrons and the neutrals within the bulk plasma. To calculate the heating due to this effect consider the time-averaged power per unit volume absorbed by the plasma P_{ohm} [2]

$$p_{ohm} = \frac{1}{T}\int_0^T J_T(t).E(t)dt = \frac{1}{2}\mathrm{Re}(\tilde{J}_T\tilde{E}^*), \tag{2.8}$$

where J_T is the total current through the plasma and $E(t)$ is the electric field within the bulk plasma (although the electric field itself is small it still plays an important role in Ohmic heating). The total current is found from the momentum equation in the plasma and taking into account electron-neutral collisions is given by [2]

$$\tilde{J}_T = (\sigma_p + j\omega\epsilon_0)\tilde{E} \tag{2.9}$$

where σ_p is the plasma conductivity (Section 1.3.4) and ω is the applied RF frequency. Substituting Equation (2.9) into Equation (2.8) gives the power absorbed due to Ohmic heating as

$$p_{ohm} = \frac{1}{2}|\tilde{J}_T|^2 \frac{1}{\sigma_{DC}}. \tag{2.10}$$

For the case where the driving frequency, ($\omega = 2\pi f$) is much less than the plasma frequency ω_p and collision frequency v_m the plasma conductivity is given by the direct current plasma conductivity, $\sigma_{dc} = e^2 n/m_e v_m$.

Stochastic Heating

The second important heating mechanism within the discharge is stochastic heating due to electron reflection off the high voltage sheaths. This is typically modelled as the elastic collision of a hard sphere with a moving wall [2]

$$u_r = -u + 2u_{es}, \tag{2.11}$$

where u_r is the velocity after the collision, u is the incident velocity of the electron reaching the sheath and u_{es} is the expansion velocity of the sheath. The power transferred per unit area in the electron velocity interval du from stochastic heating is the power of the reflected electron minus the power of the incoming electron

$$dS_{stoc} = \frac{1}{2} m_e (u_r^2 - u^2)(u - u_{es}) f_{es}(u,t) du \tag{2.12}$$

where $(u - u_{es}) f_{es}(u,t) du dt$ is the number of electrons colliding with the sheath, per unit area in a time dt. Substituting Equation (2.11) into Equation (2.12) the total power heating the plasma per unit area is given by

$$S_{stoc} = -2m_e \int_{u_{es}}^{\infty} u_{es}(u - u_{es})^2 f_{es}(u,t) du. \tag{2.13}$$

In the uniform discharge model,

$$\int_{-\infty}^{\infty} f_{es}(u,t)du = n_0 = \text{constant}. \tag{2.14}$$

A Maxwellian electron distribution is assumed to further simplify the calculation. Then if the sheath has an oscillating velocity of

$$u_{es} = u_0 \cos(\omega t), \tag{2.15}$$

then the time averaged power deposited in the plasma, due to Ohmic heating, is given by

$$\bar{S}_{stoc} = \frac{1}{2} m_e u_0^2 n_e \bar{\nu}_e. \tag{2.16}$$

Recasting Equation (2.16) in terms of the total current through the plasma, one finds

$$\bar{S}_{stoc} = \frac{1}{2} \frac{m_e \bar{\nu}_e}{e^2 n_e} J_T^2. \tag{2.17}$$

The two heating mechanisms give rise to an approximately bi-Maxwellian electron energy distribution within the RF discharge [60,64]. The electrons created within the bulk plasma undergo Ohmic heating. These electrons do not, however, have a high enough energy to overcome the potential wall in the pre-sheath region and reach the oscillating sheaths [2]. These electrons cannot therefore undergo stochastic heating and remain at a lower temperature. The small fraction of electrons that do have an energy high enough to overcome the potential barrier, and therefore reach the sheaths, are heated stochastically and reach a higher, distinct temperature.

2.1.3 The γ Mode

The radio frequency source used in these experiments was operated in the γ mode [60]. The hallmarks of the γ mode are high bulk plasma densities and low bulk electron

temperatures. At high sheath voltages (> 200 V), ionization caused by the emission of secondary (γ) electrons starts to dominate over other ionization mechanisms, such as ionization performed by the bulk plasma electrons [3]. Ions undergoing collisions with the electrodes cause electrons to be emitted from their surface. The electrons then accelerate across the sheath colliding with the neutral particles, which produces an 'avalanche' of secondary electrons. These very high energy ~ 100 eV secondary electrons enter the bulk plasma and dissipate energy, mainly through inelastic collisions with neutral particles. The number of γ electrons is very small and cannot usually be detected using a Langmuir probe [3, 65]. Ionization by the swarm of secondary electrons is the principle source of ionization sustaining the bulk plasma in the γ mode. The electrons within the bulk plasma undergo Ohmic heating [2]. These electrons do not, however, have a high enough energy to overcome the potential wall in the pre-sheath region and reach the oscillating sheaths [2, 65]. These electrons cannot therefore undergo stochastic heating and remain at a low temperature, ≤ 1 eV. A small fraction of electrons that do have an energy high enough to overcome the potential barrier and reach the sheaths are heated stochastically and reach a higher, distinct temperature, ≥ 2 eV. Ionization caused by secondary electrons can be introduced by the addition of an extra term in the diffusion equation, Equation (2.1) [3]

$$D_a \frac{d^2 n(x)}{dx^2} + v_{iz} n(x) + G(x) = 0. \tag{2.18}$$

The additional term, $G(x)$, accounts for the ionisation due to the γ electrons. Diffusion of the secondary electron population, $G(x)$, is assumed to be of the form [3, 66]

$$G(x) = \Lambda e^{-\frac{x}{\lambda_\gamma}} \tag{2.19}$$

where λ_γ is a characteristic length scale for the γ electron and Λ is a constant determined by the the number of electrons created in the sheath per ion reaching an electrode. In a symmetrically driven discharge, where the electron mean free path for ionization is much smaller than either the radius of the discharge or the distance between the electrodes, Equation (2.18) leads to an expression for the variation in the axial density, (see Appendix A)

$$Y = \cos(\frac{mx}{d}) - Y_1 \frac{\Gamma \lambda_\gamma v_i 2\cosh(x/\lambda_\gamma)}{D_a \exp(\frac{d}{\lambda_\gamma})}. \tag{2.20}$$

Y_1 is the density at the sheath normalised by the central density, Γ is the number of ionisations performed by γ electrons per ion reaching an electrode, v_1 is the velocity of the ions ejected from the plasma into the sheaths and the distance between the sheaths is $2d$. The variable m is defined in terms of R, d, v_{iz} and D_a as

$$\left(\frac{m}{d}\right)^2 + \left(\frac{2.4}{R}\right)^2 = \frac{v_{iz}}{D_a}. \tag{2.21}$$

Equation (2.20) can be rewritten in terms of m, Γ, λ_γ and d only. For a given Γ, λ_γ and d, the variable m is given by

$$\frac{\lambda_\gamma}{d} m \tan(m) = \frac{1-\Gamma}{\Gamma}. \tag{2.22}$$

Figure 2.2 shows the electron density variation between the two sheaths in a symmetric discharge. The green line shows the variation of the normalized density between the sheaths when the discharge is operating in the α mode, ($\Gamma = 0$). The blue line shows the variation of the density between the sheaths when the discharge is operating in the γ mode, ($\Gamma = \Gamma_{max} = 1.3$). The orange line shows the density variation in a transitional operating mode, $\Gamma = 1.1$.

In the γ mode the density is raised near the sheaths as this is where the secondary electrons deposit most of their energy. The transition to the γ operating regime is

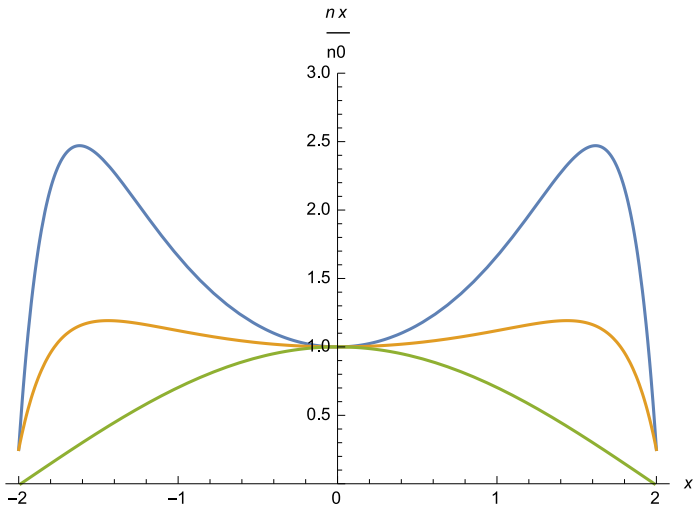

Figure 2.2: The axial variation in density within the RF discharge, (modified from [3]). The density is normalized to 1 in the center of the discharge. The blue curve shows the density density variation in the γ mode, $\Gamma = 1.3$, the orange curve shows the density density variation in a transitional mode, $\Gamma = 1.1$ and the green curve shows the density variation within the α mode, $\Gamma = 0$.

abrupt and accompanied by a sharp rise in the electron density of the bulk plasma and an accompanying drop in electron temperature. The sudden nature of the transition is due to the avalanche of γ electrons caused by ions impacting on the electrodes. When the electron density increases the sheath narrows, preventing the number of accelerated ions from increasing further. Though the plasma is sustained by ionization due to the γ electrons, the bulk electron temperature is still determined by Ohmic heating. The rise in the electron density, caused by the secondary electrons, decreases the electric field strength within the plasma. As the majority of electrons within the plasma are heated Ohmically ($n_e/n_\gamma \sim 10^{-4}$), a decrease in the electric field in turn leads to a decrease in the bulk electron temperature. In helium plasmas this leads to a very low bulk electron temperatures, $T_e \sim 0.1 - 1$ eV and high electron densities, $n_e \sim 10^{11}\text{cm}^{-3}$ [65].

2.2 Langmuir Probe Theory

2.2.1 Introduction

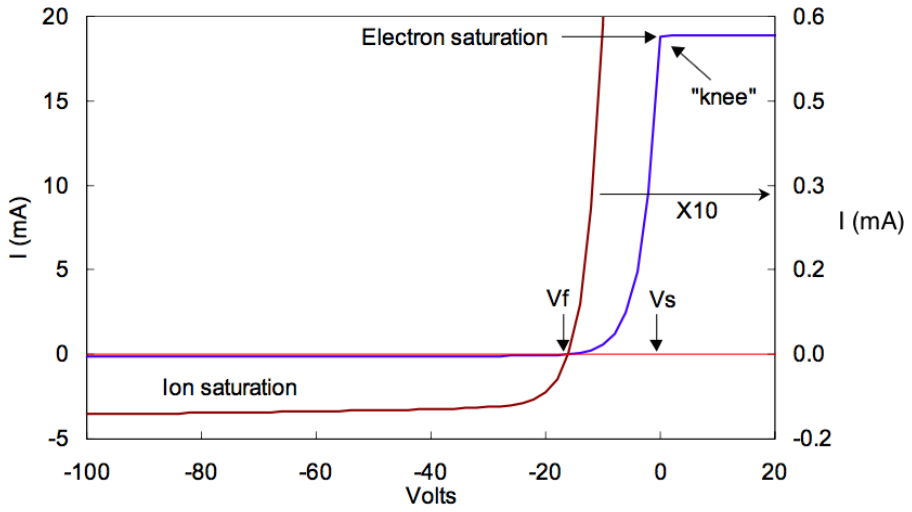

Figure 2.3: An idealised Langmuir probe trace. Reproduced from [4]. The total current curve (blue line), the ion current only (light red line), the ion current on a magnified scale (dark red line).

Simplistically a Langmuir probe consists of a conducting wire placed inside a plasma with a voltage applied across it. The current drawn from the plasma, through the wire is then measured, thus providing information about the plasma conditions. Unfortunately relating the plasma parameters to the resultant current - voltage curve inside of an RF discharge is not trivial as a number of physical processes can affect the curve [4]. These include fast electrons, a non-Maxwellian electron distribution and collisions within the sheath. Figure 2.3 (reproduced from [4]) shows the principle features associated with an ideal I-V curve. The blue line shows the full current trace whilst the dark red line focuses on the curve below the floating potential. The floating potential V_f, is the potential at which the measured current is 0 and the electron current is equal to the ion current. The ion saturation region refers to the region of the curve where there is a large negative applied voltage. Within this region no electrons overcome the potential barrier around the probe and the current is due to

ions alone. The dark red curve shows the current starting to rise steeply around -20 V as electrons start to contribute to the current. The plasma potential V_p, also referred to as the "knee" of the curve is the point at which the electron current saturates. The transition region is the part of the curve between the floating potential and the space potential, in which the ion current is almost negligible. For a Maxwell-Boltzmann electron distribution the electron current in the transition region is given by [2, 4]

$$I_e = I_0 \exp\Big[\frac{q_e(V_{probe} - V_{plasma})}{k_B T_e}\Big], \tag{2.23}$$

where I_0 is the current at the plasma potential. This provides a robust method of finding the plasma temperature. If the electron current is plotted on a semi-logarithmic plot and a straight line is fitted to the linear transition region, the gradient of the line will be $\propto 1/T_e$. The subtraction of the ion current affects only the high energy tail of the electron distribution, and thus the electron temperature found in this way is almost independent of the ion current subtraction. The electron density is found to be [4]

$$n_e = \frac{I_0}{q_e A_{probe}\sqrt{(k_B T_e)/(2\pi m_e)}}. \tag{2.24}$$

The subsequent Langmuir probe theory describes the model used to fit the ion current. A bi-Maxwellian electron distribution is eventually recovered from the measured I-V curve presented in the results Section 3.3.1. Clearly, for a bi-Maxwellian distribution an accurate subtraction of the ion current is needed to find the temperature of the hotter electrons.

2.2.2 Ion Current Collection Models

The ion current model used to analyze ion collection in a collisional sheath was that of Zakrzewski and Kopiczynski [67]. It is based on two earlier theoretical models for

collisionless ion current: that of Allen, Boyd, and Reynolds (ABR) [68] and that of Bernstein, Rabinowitz and Laframboise [69]. All three models will be briefly outlined below. As both the BRL theory and the ABR theory require the solution to relatively complicated equations, [4] the parameterised curves of Narasimhan and Steinbruchel [70] and Klagge and Tichy [71] were utilised. The expressions for the parameterised curves themselves are presented in Appendix A.

Allen-Boyd-Reynolds (ABR) Theory

ABR theory is based on a simplified model of ion collection in which the initial ion temperature is set to zero, $T_i = 0$. The result is that all of the ions move radially inwards towards the probe with the azimuthal velocity component set to zero. Neglecting orbital motion, the ion velocity is found from the conservation of energy. Assuming the potential V is zero at $r = \infty$, the ion velocity in the region surrounding the probe v_i is given by

$$v_i = \left(\frac{2q_eV}{M_i}\right)^{\frac{1}{2}}. \tag{2.25}$$

Then, given $I_i = q_e n_i v_i$, the ion density is

$$n_i = \frac{I_i}{2\pi r}\left(\frac{-2q_e}{M_i}\right)^{\frac{1}{2}}. \tag{2.26}$$

Whilst the ion current is being measured the negative probe potential means the electron density within the vicinity of the probe is small and the electron energy distribution function (EEDF) is Maxwellian. The electron density near the probe, n_e, can therefore be given by the Boltzmann distribution [68]

$$n_e = n_{e0}e^{\frac{q_eV}{k_BT_e}}. \tag{2.27}$$

Poisson's equation in a cylindrical geometry, suitable for the probe is given by

$$\frac{1}{r^2}\frac{\partial}{\partial r}\left(r^2\frac{\partial V}{\partial r}\right) = -4\pi q_e(n_i - n_e). \tag{2.28}$$

Inserting Equations (2.26) and (2.27) into Equation (2.28) leads to the differential equation

$$\frac{1}{r^2}\frac{\partial}{\partial r}\left(r^2\frac{\partial V}{\partial r}\right) = -\frac{q_e}{\epsilon_0}\left[\frac{I_i}{2\pi r}\left(\frac{2q_eV}{M_i}\right)^{12} - n_0 e^{\frac{eV}{k_BT_e}}\right]. \tag{2.29}$$

New variables are now defined; the normalised probe radius $\zeta = r/\lambda_D$, the normalised probe potential $\eta = -\frac{q_eV(\zeta)}{k_BT_e}$ and the normalised probe current

$$J = \frac{q_eI_i}{2\pi k_bT_e}\sqrt{\frac{M_i}{2\epsilon_0 n_0}}. \tag{2.30}$$

Thus Equation (2.29) can then be recast in terms of these new variables giving

$$\frac{\partial}{\partial\zeta}\left(\zeta\frac{\partial\eta}{\partial\zeta}\right) = J\zeta^{-\frac{1}{2}} - \zeta e^{-\eta}. \tag{2.31}$$

Numerical integration creates a family of J-η curves for a particular probe radius ζ. Assuming the electron temperature T_e is known (from the electron characteristic), the electron density can then be used as a fitting parameter.

Bernstein-Rabinowitz-Laframboise (BRL) Theory

BRL theory [69, 72] attempts to account for the orbital motion of a Maxwellian distribution of ions. The original theory for mono-energetic ions was the work of Bernstein and Rabinowitz [69]. The theory was extended to a Maxwellian ion EEDF by Laframboise, though this correction is often not necessary in an RF plasma due to the low ion temperature, $T_i \sim 0.03$ eV. The plasma density is related to the I-V

curve. Following a similar process as in ABR theory, the electron and ion density are found and then substituted into Poisson's equation. The distribution function is found to depend only on the energy E, and angular momentum J, both of which are constants of motion in a collisionless plasma. For a cylindrical probe convenient constants of motion are [69]:

$$E_{perp} = \frac{1}{2}m_i(\dot{\rho}^2 + \rho^2\dot{\theta}^2) + Ze\phi(\rho), \tag{2.32}$$

$$E_{parellel} = \frac{1}{2}m_e\dot{z}^2, \tag{2.33}$$

$$J = m\rho^2\dot{\theta}, \tag{2.34}$$

where $\dot{\rho}$ is the radial ion velocity, $\dot{\theta}$ is the azimuthal ion velocity, $\dot{z}$ is the polar ion velocity and $\phi(\rho)$ is the radial potential due to the probe at a distance ρ from the probe. The angular momentum can be treated as an effective potential barrier the ion must overcome to fall into the probe. Rearranging Equation (2.34) to give $\dot{\rho}$ in terms of J and E_{perp} leads to both a positive and a negative root

$$\dot{\rho} = \pm\left(\frac{2}{m}\Big(E_{perp} - Ze\phi(\rho)\Big) - \frac{J^2}{m_i^2\rho^2}\right)^{\frac{1}{2}}. \tag{2.35}$$

To account for this the distribution function, written in terms of E and J, splits into two terms

$$f(E,J) = f^+(E,J) + f^-(E,J) \tag{2.36}$$

corresponding to $\dot{\rho}$ greater than and less than zero, where it has been assumed that the particle populations are independent of the signs of $\dot{\theta}$ and $\dot{z}$. Therefore, when integrating over the distribution function, care must be taken to not count ions twice. Ions reaching the probe contribute to $f^-(E,J)$ only. Ions which orbit the probe will

contribute twice, once as they approach the probe in $f^{-}(E,J)$ and once as they move away from the probe in $f^{+}(E,J)$. The ion density n_i is found from integrating over the distribution function, where the electron density is again given by Equation (2.27). The expression for n_i and the subsequent integrations are given in [69], substituting n_i and n_e into Poisson's equation leads to the differential equation

$$\frac{1}{\zeta}\frac{\partial}{\partial\zeta}\left(\zeta\frac{\partial\eta}{\partial\zeta}\right) = 1-\frac{1}{\pi}\sin^{-1}\left(\frac{\iota/\zeta^2}{1+\eta/\beta}\right)^{\frac{1}{2}} \text{ for } \zeta<\zeta_0 \tag{2.37}$$

$$= \frac{1}{\pi}\sin^{-1}\left(\frac{\iota/\zeta^2}{1+\eta/\beta}\right)^{\frac{1}{2}} \text{ for } \zeta>\zeta_0 \tag{2.38}$$

where $\beta = E_0/Zk_BT_e$ and the dimensionless probe current ι is given by

$$\iota = \frac{1}{\pi}\frac{Ze^2}{k_bT_e}\frac{m_i}{2E_0}\frac{I^2}{n_0}. \tag{2.39}$$

Other variables have the same meaning as in ABR theory. Due to difficulties in achieving convergence, Equation (2.38) is usually approximated by a curve paramaterised in terms of ζ [71].

Ion Collection in a Collisional Sheath

The two collisionless theories outlined above can be combined to produce a collisional theory of ion collection. In this simplified model collisions between ions and neutrals in the sheath both destroy orbital motion and scatter ions elastically out of the sheath. The difference between the ABR current and BRL current within the sheath is therefore attributed to orbital motion. In the case where the sheath width is greater than the ion mean free path $s/\lambda_i > 1$, and the current at the sheath edge

is approximated by ABR theory the increase in the ion collection current due to collisions is approximated as $\gamma_1 \sim I_{ABR}/I_{BRL}$. Alternatively the decrease in ion current due to elastic scattering is estimated as [67]

$$\gamma_2 = \frac{3 - e^{-s/\lambda_i}}{2(1 + s/\lambda_i)}. \tag{2.40}$$

Therefore the total collisional ion collection current is written in terms of the collisionless currents as

$$I_{col} = \gamma_1 \gamma_2 I(BRL). \tag{2.41}$$

The ion currents found in Section 3.3.1 were obtained by fitting parameterized curves calculated by Klagge and Tichy to the experimental data [71]. The expressions for the parameterized curves are given in Appendix A.

2.3 Optical Emission Spectroscopy

2.3.1 Introduction

Neglecting opacity, the emissivity of a plasma at a specific wavelength in units of [photons cm^{-3} s^{-1} $\cdot$ steradians] is given by [73, 74]

$$\epsilon_{ij} = (4\pi)^{-1} n(i) A_{ij} \tag{2.42}$$

where $n(i)$, is the population density of the excited state i, and A_{ij} is the rate coefficient for a spontaneous transition between the levels i and j. Thus, theoretically a measurement of the emissivity gives the population of the excited state $n(i)$, assuming A_{ij} is known. Similar measurements for different transitions could, therefore, determine the population densities across all of the relevant excited states. The pho-

ton number measured by a charged coupled device (CCD) camera looking at such a plasma in terms of emissivity is

$$I_{photon}(\lambda_{ij}) = \epsilon_{ij} V \Omega T(\lambda_{ij}) \eta(\lambda_{ij}), \tag{2.43}$$

where λ_{ij} is the wavelength of the emitted photon, V is the plasma volume, Ω is the solid angle subtended by the collection optics, $T(\lambda_{ij})$ is the transmission of detection system at wavelength λ_{ij} and $\eta(\lambda_{ij})$ is the quantum efficiency of the CCD camera at the wavelength λ_{ij}. All the quantities other than the emissivity are characteristic of the detection system and can be measured. Plasma parameters are often found by taking the ratio of emission intensities of two different wavelengths. Taking the ratio of emission lines removes the dependence on the solid angle and volume, whilst also making an absolute calibration of the spectrometer unnecessary.

The intensity ratio between two emission lines $I_{photon}(\lambda_{ij})$ and $I_{photon}(\lambda_{kl})$ is

$$\frac{I_{photon}(\lambda_{ij})}{I_{photon}(\lambda_{kl})} = \frac{\epsilon_{ij} T(\lambda_{ij}) \eta(\lambda_{ij})}{\epsilon_{kl} T(\lambda_{kl}) \eta(\lambda_{kl})} = \frac{1}{F_R} \frac{\epsilon_{ij}}{\epsilon_{kl}}, \tag{2.44}$$

where F_R is a calibration factor which can be found using a calibrated white light source. Finding plasma parameters from the ratio of two emission lines requires a model to relate the excited state populations to the plasma parameters. For example consider the steady state corona (SSC) model based on the conditions found within the suns' corona [75]. This model assumes that due to low plasma density, emitted radiation escapes the system, allowing stimulated emission and absorption to be ignored. Therefore upwards transitions are caused only by electron impact excitation. Furthermore at low electron densities the majority of the electrons remain in the ground state and thus only upwards collisions from the ground state are considered. Downwards transitions however, occur through spontaneous emission as the density is too low for collisional de-excitation to be important. The rate equation for the

population densities in the corona model is given by

$$\frac{dn(i)}{dt} = n_e C_{1i} n(1) - \sum_{j<i} A_{ij} n(i) \tag{2.45}$$

where C_{1i} is the rate coefficient for electron impact excitation from the ground state to the excited state $n(i)$, and $n(1)$ is the population of the ground state. In the steady state $\frac{dn(i)}{dt}$ can be set to zero, allowing the population density to be written as

$$n(i) = \frac{n_e C_{1i} n(1)}{\sum_{j<i} A_{ij}}. \tag{2.46}$$

Substituting the population density back into the equation for the emissivity gives

$$\epsilon_{ij} = (4\pi)^{-1} B_{ij} n_e C_{1i} n(1), \tag{2.47}$$

where $B_{ij} = \frac{A_{ij}}{\sum_{j<i} A_{ij}}$ is the branching ratio. Substituting Equation (2.47) into Equation (2.44) gives

$$\frac{I_{photon}(\lambda_{ij})}{I_{photon}(\lambda_{kl})} = \frac{1}{F_R} \frac{B_{ij} C_{1i}}{B_{kl} C_{1k}}. \tag{2.48}$$

Thus, this ratio can be used to find the electron temperature since the rate coefficient for electron impact excitation from the ground state C_{1i} is a function of electron temperature.

2.3.2 Collisional Radiative Models

The corona model predicts the electron temperature of a radio frequency plasma up to electron densities of $n_e \sim 10^{10}$ cm^{-3} with reasonable accuracy [76]. Above this collisional and radiative processes not considered in the corona model start to become important, such as excitation transfer between excited states. At higher densities,

to find plasma parameters from the line ratios, a collisional radiative (CR) model replaces the steady state corona model. A CR model is a series of rate equations for the population densities [77–79]. The rate of change of population in state i is given by

$$\begin{aligned}\frac{dn(i)}{dt} &= \sum_{j<i} n(i) n_e C_{ji} + \sum_{k>i} n(k)(n_e C_{ki} + A_{ki}) \\ &- n(i)\left[\sum_{j<i}(n_e C_{ij} + A_{ij}) + n_e S_i + \sum_{k>i} n_e C_{ik}\right] + n_e n^* R_i \end{aligned} \tag{2.49}$$

where S_i is the ionization rate coefficient, n^* is a charged state and R_i is the recombination rate. Each rate coefficient must either be measured or calculated theoretically. Simulations are often performed with a specified mass density and therefore the electron density is calculated using the equilibrium ionisation balance. The ionisation balance takes the form of a set of equations similar to [78]

$$\begin{aligned}\frac{dN_{1s^2\ ^1S}}{dt} &= -n_e\ (S_{1s^2\ ^1S\rightarrow 1s\ ^2S} + Q_{1s^2\ ^1S\rightarrow 1s2s\ ^3S} + X_{1s^2\ ^1S\rightarrow 1s2s\ ^3S})\ N_{1s^2\ ^1S} \\ &+ n_e\ R_{1s\ ^2S\rightarrow 1s^2\ ^1S}\ N_{1s\ ^2S} \\ &+ n_e\ (Q_{1s2s\ ^3S\rightarrow 1s^2\ ^1S} + X_{1s2s\ ^3S\rightarrow 1s^2\ ^1S})\ N_{1s2s\ ^3S}, \end{aligned} \tag{2.50}$$

with a separate equation for the ground state, metastable states and ionic states. X and Q are the metastable and parent metastable cross coupling coefficients. Here we use the commercially available collisional radiative code PrismSPECT [80]. PrismSPECT is capable of creating synthetic emission spectra for a grid of input plasma parameters. The processes accounted for by the model include; collisional ionization, recombination, excitation, de-excitation, photoionization, photoexcitation, stimulated emission, spontaneous decay, radiative recombination, dielectronic recombination, au-

toionization, and electron capture. PrismSPECT accounts for states up to the $n = 10$ level. The model is widely used to find plasma parameters from optical emission spectroscopy [39,80]. The code is, however, not purpose built to simulate RF plasmas and does not account for the loss of charged particles to the electrodes, the diffusion of charged particles out of the discharge or ionization due to γ electrons.

Steady state solutions for the population densities can be found by setting $\frac{dn(i)}{dt} = 0$. After $n(i)$ is calculated it can be substituted back into Equation (2.44) similarly to when $n(i)$ was found using the corona model (SSC). However, in this case, as absorption and stimulated emission are not necessarily negligible, a correction has to be made to account for the opacity of the plasma. This is done by introducing an extra variable into the emissivity equation

$$\epsilon_{ij} = (4\pi)^{-1} n(i) \Lambda(\lambda_{ij}) A_{ij} \tag{2.51}$$

where $\Lambda(\lambda_{ij})$ is the optical escape factor at the wavelength λ_{ij}.

2.3.3 Helium Emission Lines

In helium the triplet and singlet excitation cross sections for electron impact excitation have very different temperature dependences [5]. Therefore in the SSC model singlet, triplet line ratios are generally chosen to measure electron temperatures. Early attempts to calculate the electron temperature in low density helium plasmas focused on the 492/471 line ratio [81]. However this method was shown to be inapplicable to plasmas with densities above $n_e \sim 10^{10}$ cm^{-3} due to the effects of metastable states [76]. Spin-changing collisions such as

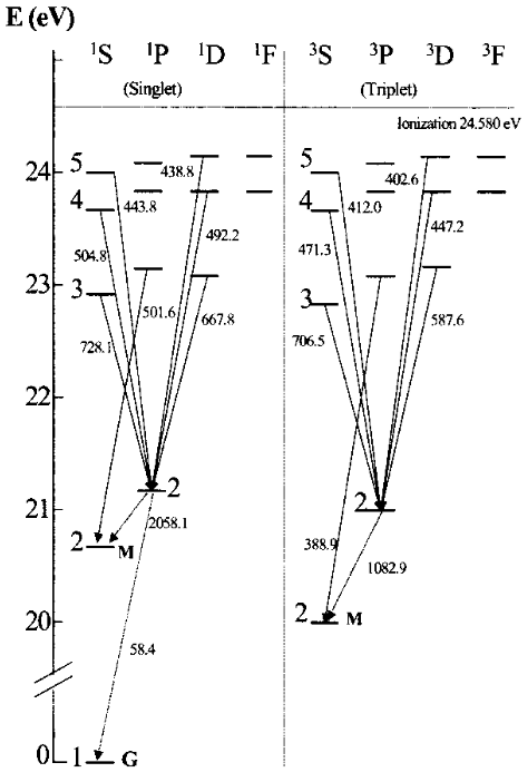

Figure 2.4: Partial Grotian diagram for atomic Helium showing transitions for states up to $n = 5$. Reproduced from [5]

$$e^-_{cold} + He(2^1S) \rightarrow e^- + He(2^3S) + 0.79 \text{ eV}, \tag{2.52}$$

lead to an increased population of the 2^1S metastable at the expense of the 2^3S metastable [82]. The excitation transfer cross sections for spin-changing collisions are small compared to the excitation transfer cross sections for spin-conserving transitions (when comparing states with the same principle quantum number). Therefore the increased population of the 2^3S metastable leads to an increased population of the triplet system.

Boivin used the ratio 504/471 ($4^1S \rightarrow 2^1P/4^3S \rightarrow 2^3P$) to perform tempera-

ture measurements in a helicon plasma source at densities slightly higher than those studied here using a CR model [5]. This ratio was chosen to minimise dependance on the electron density by minimising the effects of the metastable 2^1S, 2^3S states. S-S excitation transfer transitions are forbidden, and therefore the transition cross-sections are small. Boivin performed further investigations into the ratios $4^1S \rightarrow 2^1P$ (504.8 nm)/ $4^3S \rightarrow 2^3P$ (471.3 nm), $4^1D \rightarrow 2^1P$ (492.2 nm)/$4^3S \rightarrow 2^3P$ (471.3 nm) and $4^1D \rightarrow 2^1P$ (492.2 nm)/ $4^1S \rightarrow 2^1P$ (504.8 nm) at higher plasma densities [55]. These ratios involve transitions in the same spectral region, with similar branching ratios, for which the plasma was optically thin [5, 55]. The CR models 'found significant differences at low densities [55] for both the $4^1D \rightarrow 2^1P$ (492.2 nm)/$4^3S \rightarrow 2^3P$ (471.3 nm) and $4^1D \rightarrow 2^1P$ (492.2 nm)/ $4^1S \rightarrow 2^1P$ (504.8 nm) ratios, though good agreement was found for the $4^1S \rightarrow 2^1P$ (504.8 nm)/ $4^3S \rightarrow 2^3P$ (471.3 nm) ratio. It was suggested differences between the theoretical predictions and the experimental data may have been due to excitation transfer between the 2^3S metastable and the 4^1D not being accounted for correctly by the model or the lack of high quality atomic data for shells with $n > 5$.

The ionisation balance equation (Equation (2.50)) is not formulated to account for particle diffusion out of the discharge, this affects the population densities of the metastable states. Therefore we choose also to avoid emission lines which have a strong dependence on metastable states. As S-S excitation transfer is forbidden, and the $n = 4$ states have a large energy gap from the metastable states, they are likely to be the least affected, (emission from states higher than $n = 4$ is too weak to detect [5]).

Langmuir probe data, presented in Section 3.3.1 will illustrate that the plasma produced by our RF source had a bi-Maxwellian electron distribution. Saski *et al* studied bi-Maxwellian helium plasmas at higher densities and temperatures than those studied here [73], $T_e^{cold} \sim 5$ eV, $T_e^{hot} \sim 20$ eV and $n_e \sim 10^{11} - 10^{13}\text{cm}^{-3}$. The Langmuir

probe results they presented gave only the cold electron temperature, whereas emission spectroscopy results give both hot and cold electron temperatures. Both the hot and cold electron temperatures measured by the spectroscopy match within error, whilst they are both significantly higher than the electron temperature measured by the Langmuir probe. Saski *et al* suggest that at cold electron temperatures, below 10 eV, the hot electrons have a large effect on the ratios. This is expected as many excitation cross sections decrease rapidly at low temperatures. Clearly the hot electrons are spectroscopically important within the RF discharge as is demonstrated during the experiments performed in the next chapter.

2.4 Summary

In Chapter 2 the essential theory for understanding the work described in Chapter 3 was presented. The radio frequency plasma source was introduced alongside the two heating mechanisms responsible for producing the bi-Maxwellian electron energy distribution. The ion collection models used to extract the electron current curve from the Langmuir probe measurements were outlined and the method used to extract the electron densities and temperatures of the bi-Maxwellian electron energy distribution function were described. Optical emission spectroscopy is introduced as a method of inferring the parameters within a plasma. The line ratio technique is discussed in detail and the need for collisional radiative models is explained. Finally the chapter closed with a detailed discussion of the specific lines of neutral helium which were chosen for inferring the plasma parameters in the experiment in Chapter 3.

Chapter 3

Electron Temperature and Density Measurements Using Optical Emission Spectroscopy in a Helium Capacitively Coupled Radio Frequency Discharge

3.1 Introduction

The ability to make non-invasive measurements of the electron temperature and density is clearly desirable in any plasma source. This is often achieved using optical emission spectroscopy (OES) [75]. An optical emission spectroscopy diagnostic has a number of benefits, it is non-invasive, requires little maintenance and is experimentally simple. However, at even moderate electron densities finding the plasma parameters from the measured spectra is a complex task, particularly at low temperatures. The analysis relies on complicated collisional radiative models which must be solved computationally [83, 84]. Capacitively coupled RF plasma sources, having electron densities from 10^9 cm^{-3} to 10^{12} cm^{-3} and electron temperatures from 0.1 eV to 10 eV are widely used for etching in the processing industry, and have been over the past 30 years [2, 52]. Accurate electron temperatures and densities can be calculated from Langmuir probe measurements [85,86]. However, probe measurements are invasive and cause perturbations within the plasma, which can prohibit their use in certain applications [87]. Furthermore, non-invasive diagnostics [75] are specifically required in both tokamaks and space propulsion systems [88–90].

This chapter outlines a spectroscopic method used to measure the temperature and density of a bi-Maxwellian electron distribution inside a helium, capacitively coupled, radio frequency discharge using optical emission from the neutral n = 4 transitions [91]. Three ratios $4^1S \rightarrow 2^1P$ (504.8 nm)/ $4^3S \rightarrow 2^3P$ (471.3 nm), $4^1D \rightarrow 2^1P$ (492.2 nm)/$4^3S \rightarrow 2^3P$ (471.3 nm) and $4^1D \rightarrow 2^1P$ (492.2 nm)/ $4^1S \rightarrow 2^1P$ (504.8 nm) were calculated for measured spectra and synthetic spectra created using the collisional radiative model PrismSPECT [80]. The synthetic ratios were fitted to the experimental data using the method of least squares. The method is based predominantly on the previous work of Boivin *et al* [5, 55, 78], carried out in a helicon source. Previous attempts to model the emission from RF helium sources have achieved variable success [5, 55, 78] with disparities between experiment and simulations at-

tributed to inaccuracies in the models. Attempts to model the emission lines with a bi-Maxwellian plasma have found a large discrepancy between OES measurements and Langmuir probe measurements [73].

The previous chapter outlined the theoretical background of both the radio frequency discharge itself as well as the diagnostics used during the experiment. Some aspects of collisional radiative modelling were discussed alongside the relevant literature. This chapter commences with details of the plasma source used, as well as the set up of the diagnostics. The results are presented and a comparison is made between hot and cold electron temperatures and densities measured by both a Langmuir probe and optical emission spectroscopy. While good agreement is found between the two diagnostics for the hot electron temperature the other parameters were not inferred accurately from the OES data. The line ratio sensitivity to electron density was found to be too weak to infer densities using OES and the atomic cross sections appear to be inaccurate at very low electron temperatures T_e $\sim$0.1 eV.

3.2 Experimental Setup

3.2.1 Radio Frequency Discharge

The experiments were performed in a cylindrical, aluminium vacuum chamber (diameter $\sim$ 120 cm, height $\sim$ 40 cm). Figure 3.1 shows a schematic of the experimental setup. The plane parallel, capacitively coupled discharge sits in the centre of the chamber. Both the driven (top) and grounded (bottom) aluminium electrodes had a 16 cm diameter and 0.5 cm thickness. The bottom electrode was grounded to the chamber floor and the distance between the two plates was 4 cm. The base pressure of the system was 1×10^{-5} mbar and all measurements were performed with a helium fill pressure of 1 ± 0.05 mbar. The pressure was measured using an MKS instruments Se-

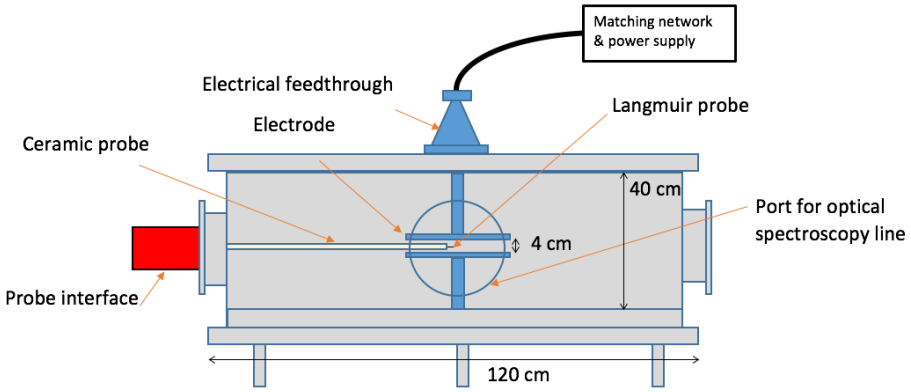

Figure 3.1: The vacuum chamber and plasma source.

ries 910 DualTrans MicroPirani gauge attached near the top of the chamber above the driven electrode. Power was supplied to the driven electrode by an AE CESAR 1310 radio frequency power generator [92] with maximum power output of 1000 W. The power supply was mounted above the chamber and grounded to the same baseplate as the chamber and the discharge. The output frequency of the power supply was 13.56 MHz. The power generator was operated in auto-tune mode and attached to an Advanced Energy Navio matching network [93]. The close proximity of the plasma source, power generator and matching network reduced RF pickup in the cables. The power reflected back to the generator after the matching unit never exceeded 1 % of the output generator power. The input and reflected power were measured by the CESAR generator and, although the losses through the system cannot be neglected, the powers referred to in the results section are those generated by the power supply.

All of the measurements were performed 1.8 $\pm$ 0.1 cm above the grounded plate. The optical emission spectrometer imaged a point that was a radial distance r = 0.0 $\pm$ 0.1 cm from the discharge centre. The end of the Langmuir probe tip was a radial distance r = 1.0 $\pm$ 0.1 cm from the discharge centre. Spectra were taken when the

probe both was and was not in operation, with no discernable difference between the two cases.

3.2.2 Langmuir Probe

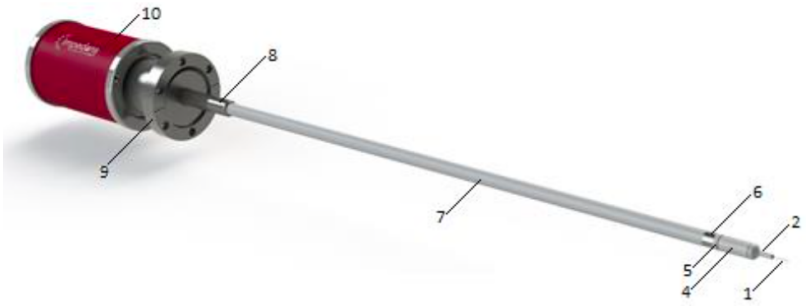

Figure 3.2: The impedans Langmuir probe used to measure the I-V curve (reproduced from [6]): 1. The tungsten probe tip. 2. The ceramic probe tip housing. 4. The RF compensation electrode. 5. The ceramic ring to isolate the RF compensation electrode. 6. The direct current compensation electrode (this compensates for the perturbation to the bulk plasma caused by biasing the probe). 7. The ceramic probe shaft. 9. The vacuum flange attachment. 10. The computer probe interface.

The Langmuir probe used to perform the experiments was supplied by Impedans [6]. The I-V trace was directly recorded on a dedicated windows computer. During the experiments the probe tip length was 2 cm and the probe tip radius was 0.2 mm. An image of the probe is shown in Figure 3.2 reproduced from [6]. The probe was attached to a CF 40 flange at the edge of the vacuum chamber. The ceramic probe shaft was 60 cm long and the tungsten probe tip was situated a radial distance $r = 1.0 \pm 0.1$ cm from the discharge centre and a height of 1.8 ± 0.1 cm above the lower electrode.

As the probe was being operated in an RF plasma, RF compensation was built into the probe to allow the trace to be analyzed using standard techniques. In effect this was done by building a frequency filter into the probe tip [94], a schematic of the

setup is shown in Figure 3.3. The aim is to force the impedance between the probe and the ground Z_s to be much larger than the impedance between the probe and the plasma Z_p at the RF frequency (13.56 MHz). In effect this creates a potential divider and the probe tip floats at the plasma potential [94]. Z_s is increased by adding RF chokes as close as possible to the probe tip, the chokes should have a large impedance at the RF frequency. The chokes are situated as close as possible to the tip to decrease the stray capacitance [94]. Z_p is also minimised by capacitively coupling the probe to the plasma (labeled 4 in Figure 3.2).

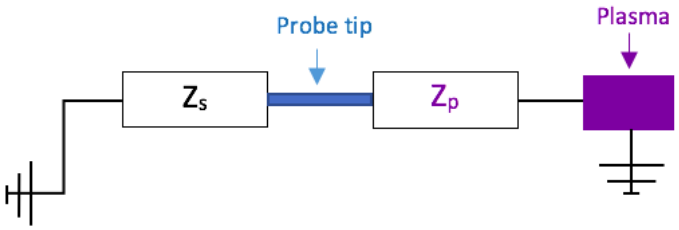

Figure 3.3: RF compensation in the Langmuir probe Z_s is the impedance between the probe and the ground whilst Z_p is the impedance between the probe and the plasma.

To perform a measurement the probe voltage was swept between - 60 V and 40 V, with a sweep time of 1 ms. Each measurement was an integration of 10 such traces. Three measurements were performed at each input RF power.

3.2.3 Spectrometer

The spectroscopy diagnostic was performed with an Aryelle 200 Echelle spectrometer coupled to an intensified Andor iStar CCD camera with a 1 μs gate width. The entrance apeture had a 40 μm radius. A simplified schematic of the optical path is shown in Figure 3.4. The overall magnification between the object and the image

formed on the entrance aperture was 0.36. A blazed 'Echelle' grating diffracted the light, causing a large dispersion at high orders and leading to a large overlap between adjacent orders. A second grating is then used to separate the overlapping orders, the final spectra is pieced together from several different orders by the spectrometer software. This process achieves a high spectral resolution over a large wavelengths range.

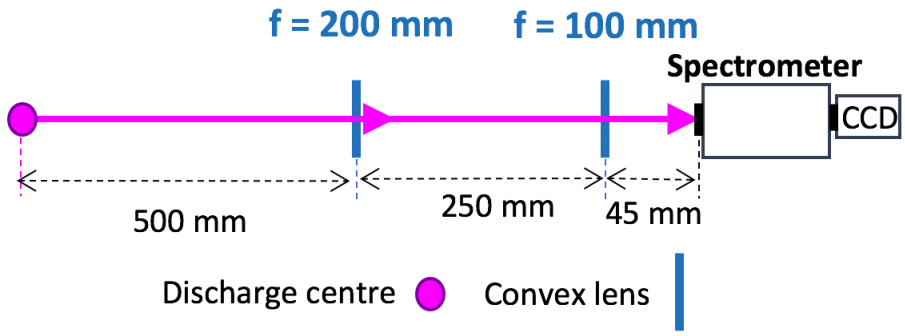

Figure 3.4: Experimental setup of the optical spectroscopy line. All lenses had a two inch diameter.

To correct for the effects caused by the transmission/reflection of optics, and for any spatial variation in the camera sensitivity, the spectrometer was calibrated using a calibrated white light source. The relative calibration was performed by placing a known white light source (operating temperature T = 2800 K) in the region where the plasma is formed, and directing it along the optical path between there and the spectrometer. The resultant measured spectrum can then be divided by the known emission curve of the source, producing a correction factor to be applied to the data. The white light spectrum and correction curve are shown in Figure 3.5. The sensitivity of the spectrometer decreases at the edges of each diffracted order leading to an oscillatory pattern when the separate orders are spliced together.

In order to find the instrument function of the spectrometer a Gaussian was fitted

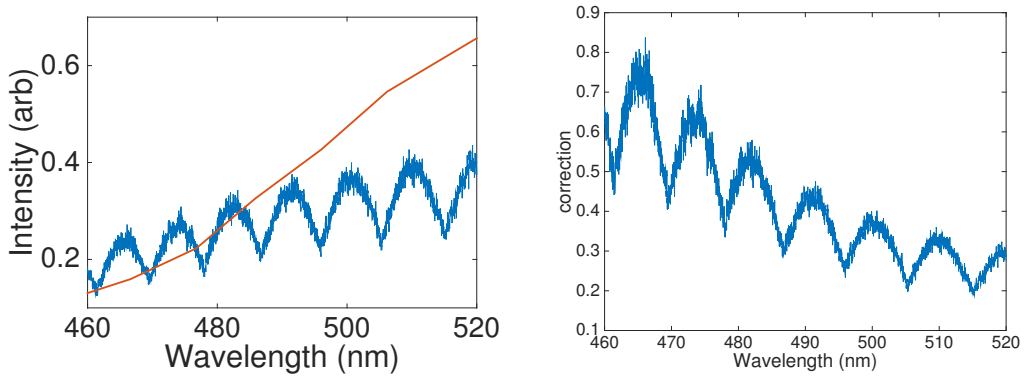

(a) (b)

Figure 3.5: a) The measured white light spectra (blue data) plotted alongside the known spectra of the calibrated white light source (orange data). b) The correction curve

to the peak of a mercury spectral line at 546.2 nm using a least mean squared fit. The Gaussian fitted to the data is shown in Figure 3.6. The full width half maximum of the peak was found to be ≈ 0.11 nm, giving a spectral resolution of $\lambda/\Delta\lambda \approx 5000$.

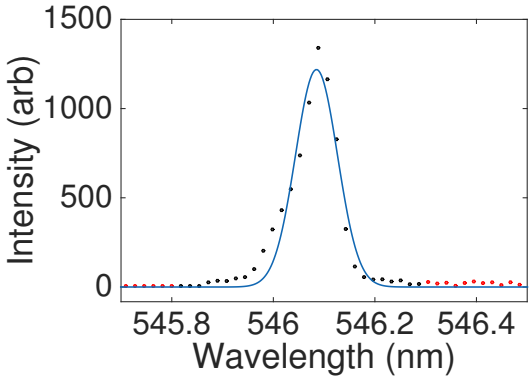

Figure 3.6: A Gaussian curve (blue line) fitted to the mercury peak (black data points) at 546.1 nm, the red data points have been excluded from the fit.

3.3 Results

3.3.1 Langmuir Probe

The RF discharge was characterised using a Langmuir probe. An example of a raw I-V curve measured at an input power of 500 W and a helium fill pressure of 1 mbar is shown in Figure 3.7. This data will be used throughout this section to demonstrate the analysis procedure. The ion current is subtracted from the total I-V curve and the remaining electron current is used to find the electron temperature and density.

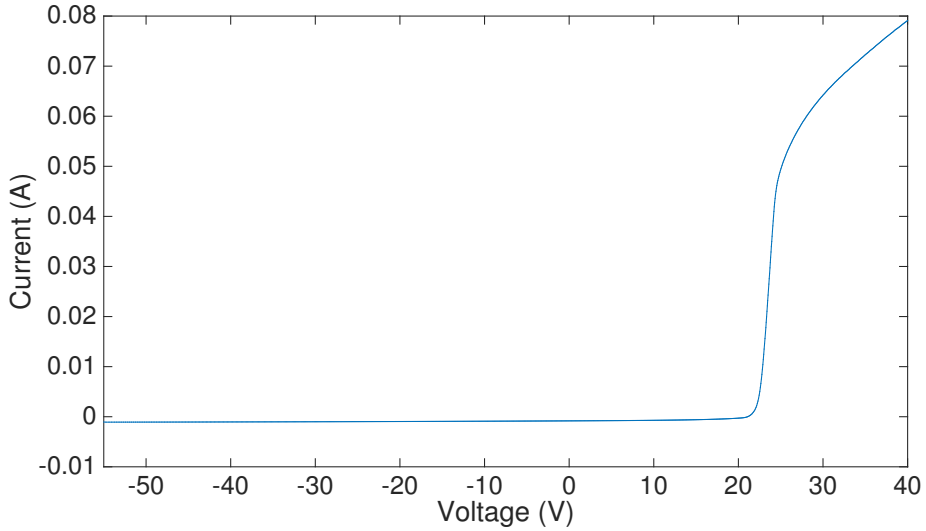

Figure 3.7: An example raw I-V curve. Measured at an input power of 500 W and a helium gas fill pressure of 1 mbar.

3.3.1.1 Ion Current

In order to calculate plasma conditions from the I-V curve the current contributions due to both the electrons and the ions have to be separated. The analytical model used to find the ion current in the collisional sheath is described in appendix A. A sample of the fitted data is shown in Figure 3.8.

The curve was fitted using a least mean squares fit between -55 V and -5 V, and

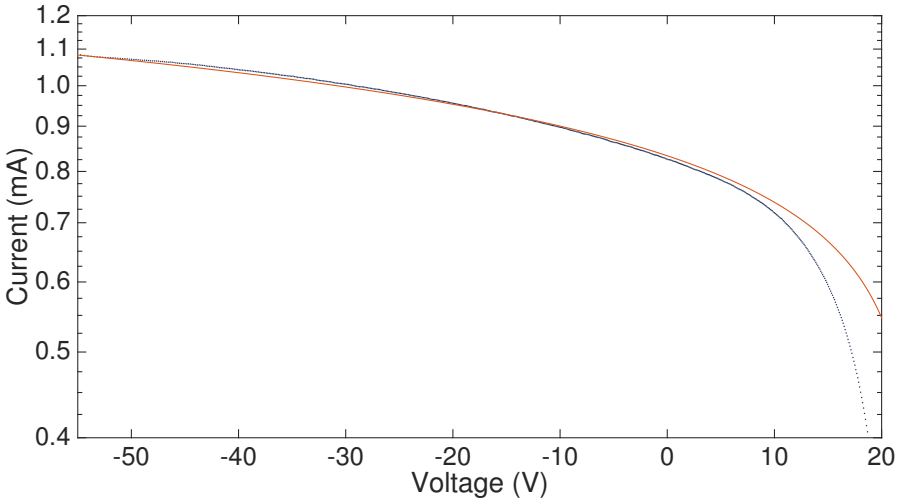

Figure 3.8: The measured I-V curve at 500 W (blue dotted line). The analytic curve for ion collection fitted to the measured I-V curve fitted from -50 V to -5 V (red line). At these voltages only the ion current makes a significant contribution to the curve. Fitting the analytical curve to the data gave an electron temperature, $T_e = 0.4$ eV and an electron density, $n_e = 6 \times 10^{10}$ cm^{-3}.

within this range the current contribution due to the electrons was assumed to be negligible. The analytic curve was calculated using an electron temperature, $T_e = 0.4 \pm 0.1$ eV. Fitting the bulk electron temperature to the linear section of the I-V curve on a semilogarithmic plot is effectively independent of the ion current, $T_e = 0.4 \pm 0.1$ eV is recovered either before or after subtraction of the ion current. The fit gives an electron density of $n_e = 6 \pm 1 \times 10^{10}$ cm^{-3}. The error in the electron density is calculated by allowing the RMS fitting error to vary by 20 % from the minimum error. However finding the electron density from fitting an analytical curve to the ion current is highly inaccurate and the above result is an order of magnitude estimate for the true electron density [4]. The ion current for each data set was calculated and subtracted independently.

3.3.1.2 Electron Current

A change in variables often used in the literature is now introduced such that U = V_{probe} - V_{plasma}, where V_{probe} is the probe potential and V_{plasma} is the plasma potential. The electron current is shown in Figure 3.9. The electron energy probability function calculated following the Druyvesteyn method [2, 7] is shown in Figure 3.10. With the ion current subtracted the Bi-Maxwellian electron distribution is clear in both Figures 3.9 and 3.10 [4, 58, 86, 95]. In Figure 3.9 there are two distinct linear sections

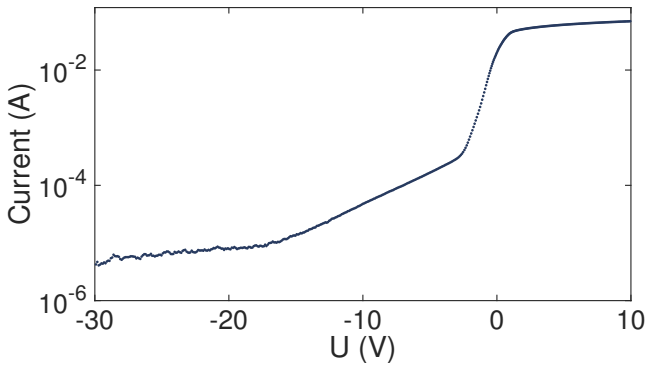

Figure 3.9: The electron current contribution to the I-V curve found from subtracting the fitted ion current from the total curve.

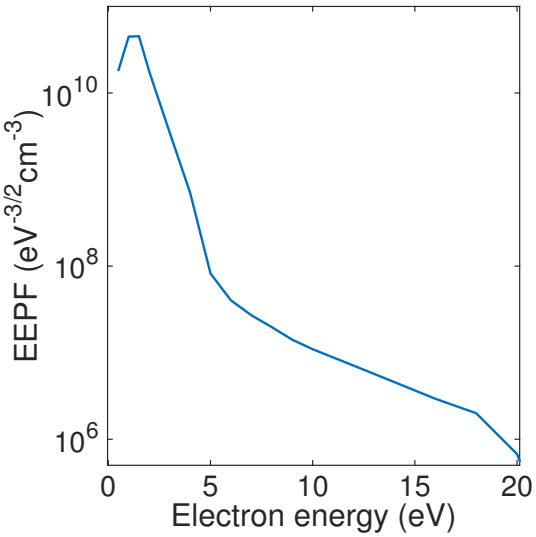

Figure 3.10: The electron energy probability function calculated following the Druyvesteyn method [2, 7].

of the curve, one between $\sim$ -15 V and -3 V attributed to the hotter electrons and a second between $\sim$ -3 V and 0 V attributed to the colder, bulk electrons [4]. To find the hot and cold electron temperatures and densities analyses similar to that described in [95] were performed. A theoretical curve of the form

$$I_e = i_e^{cold} \mathrm{e}^{\frac{q_e U}{T_e^{cold}}} + i_e^{hot} \mathrm{e}^{\frac{q_e U}{T_e^{hot}}}, \tag{3.1}$$

where i_e^{cold} and i_e^{hot} are the cold and hot electron currents when the plasma potential is equal to the probe potential, and T_e^{cold} and T_e^{hot} are the temperatures of the hot and cold electron populations. i_e is related to the density of the electron fraction by

$$n_e = \frac{i_e}{q_e A_{probe} \sqrt{(k_B T_e)/(2\pi m_e)}}. \tag{3.2}$$

A fitted curve is plotted in Figure 3.11. A least mean squared fit was performed from U = -0.7 V to -15 V in MATLAB. The fit gives electron temperatures, $T_e^{cold} = 0.4$ eV, $T_e^{hot} = 3.9$ eV and electron densities, $n_e^{cold} = 1.3 \times 10^{11}$ cm^{-3}, $n_e^{hot} = 7.5 \times 10^{8}$ cm^{-3}. The fitting procedure gave an RMS fitting error of 0.03 which was typical of the RMS error, whose values ranged from 0.017 to 0.05. The fitting error decreased as the power supplied to the discharge increased. The variation between repeat measurements was far larger than the errors given by the fitting.

The probe holder can lead to a depletion in the plasma density [96]. To correct for the the electron densities are scaled by a factor of $(1 + \frac{r_h}{\lambda_e}) \approx 3$, where $r_h = 0.2$ cm, is the radius of the probe holder and $\lambda_e \approx 0.1$ cm, is the electron mean free path [97,98]. The variation of the cold electron temperature and density with power are shown in Figure 3.12. The data points show the mean values at each power and the error bars represent the standard deviation calculated using three repeat measurements. The measured temperature of the cold electron population remained 0.5 $\pm$ 0.1 eV as the power was varied between 300 W and 700 W. This is because the low temperature

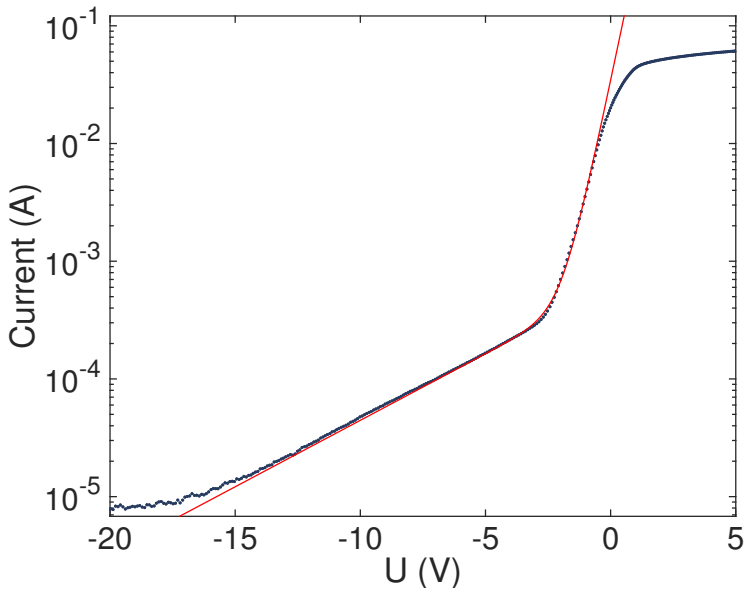

Figure 3.11: The analytical curve (Equation (3.1)) fitted to the electron current. The fit gives electron temperatures $T_e^{cold} = 0.4$ eV, $T_e^{hot} = 3.9$ eV and electron densities $n_e^{cold} = 1.3 \times 10^{11}$ cm^{-3}, $n_e^{hot} = 7.5 \times 10^{8}$ cm^{-3}.

electrons are heated ohmically and increasing the power does not significantly alter the electric field within the discharge in the γ mode. The weak dependence of the bulk electron temperature on power was expected, and agrees with previous work [2, 3]. The density grew from $9.9 \pm 1.2 \times 10^{10}$ cm^{-3} at 300 W to $8.7 \pm 4.8 \times 10^{11}$ cm^{-3} at 700 W. The increase in error may be due to a slight decrease in plasma stability at higher powers. The measured temperature of the hot electron population grew from 3.0 ± 0.1 eV at 300 W to 4.0 ± 0.3 eV at 700 W. The density grew from $1.9 \pm 0.2 \times 10^{9}$ cm^{-3} at 300 W to $2.8 \pm 0.5 \times 10^{9}$ cm^{-3} at 700 W. These trends are similar to the results found in other helium γ mode discharges [3].

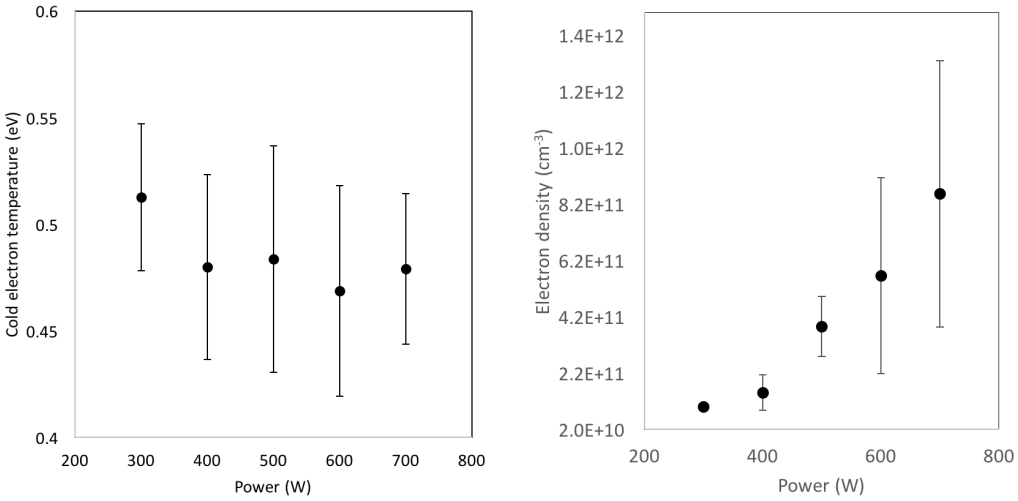

(a) (b)

Figure 3.12: The variation of plasma parameters with input power. a) The temperature of the cold electron population. b) The density of the cold electron population.

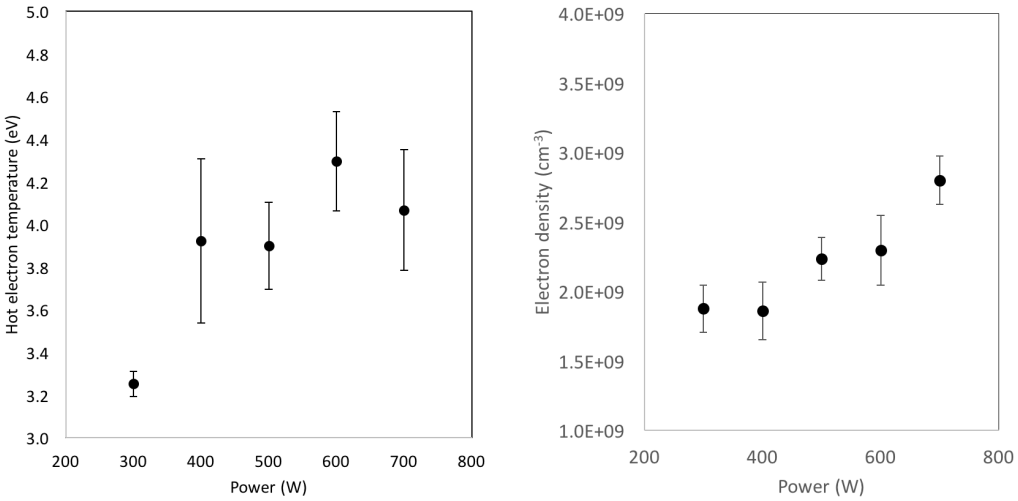

(a) (b)

Figure 3.13: The variation of plasma parameters with input power. a) The temperature of the hot electron population. b) The density of the hot electron population.

3.3.2 Emission Spectroscopy

Labeled emission spectra measured at input powers of 300 W and 700 W are shown in Figure 3.14. The spectrum shows the optical emission from the discharge between 470 nm and 510 nm. This range includes four transitions from neutral helium,

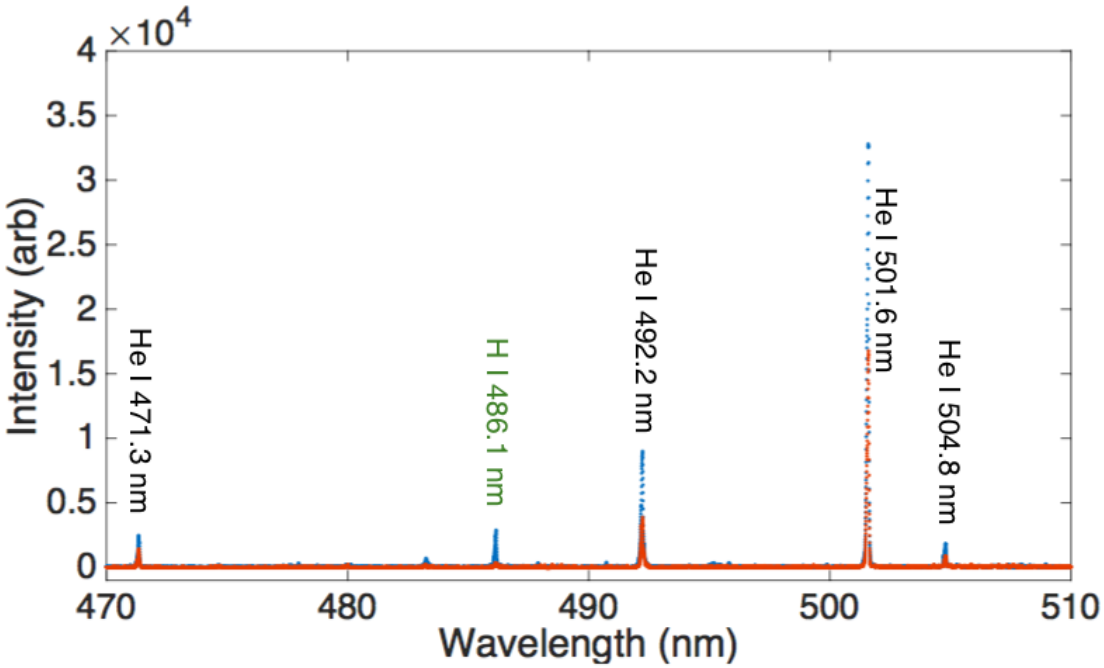

Figure 3.14: Emission spectra of the discharge taken at both 700 W (blue data points) and 300 W (orange data points). Helium emission lines are labeled in black whilst emission from hydrogen emission lines are labeled in green. The emission lines are: He I 471.3 nm triplet- $4^3S \rightarrow 2^3P$, He I 492.2 nm singlet- $4^1D \rightarrow 2^1P$, He I 501.6 nm singlet- $3^1P \rightarrow 2^1S$, He I 504.8 nm singlet- $4^1S \rightarrow 2^1P$ and H I $4^1D \rightarrow 2^1P$.

three of which have an upper state with a principle quantum number, $n = 4$: the $4^3S \rightarrow 2^3P$ transition at 471.3 nm, the $4^1D \rightarrow 2^1P$ at 492.2 nm and the $4^1S \rightarrow 2^1P$ transition at 504.8 nm. The most intense emission line is from the He I transition $3^1P \rightarrow 2^1S$ at 501.6 nm ending on a metastable state. Emission from neutrals dominates the spectra due to the low electron density and electron temperature attained within the discharge. The neutral hydrogen line at 486.1 nm is due to an unknown contamination source within the chamber. As neither the source nor the relative number fraction of the hydrogen was known this line was not used for diagnostic purposes.

Four emission spectra were measured at each input power. Figure 3.15 shows the mean absolute peak intensity of the He I emission lines as a function of input power. The error bars indicate the standard deviation between the repeated measurements.

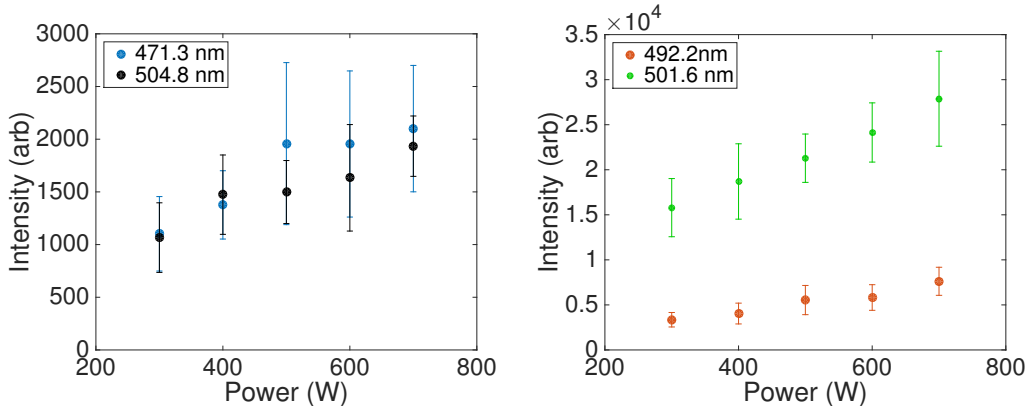

(a) (b)

Figure 3.15: The mean peak absolute intensities of the He I emission lines as a function of input power. a) Blue data points - 471.3 nm triplet $4^3S \rightarrow 2^3P$, black data points - 504.8 nm singlet $4^1S \rightarrow 2^1P$. b) Orange data points - 492.2 nm singlet $4^1D \rightarrow 2^1P$, green data points - 501.6 nm singlet $3^1P \rightarrow 2^1S$. The error bars show the standard deviation over the four repeat measurements.

The intensity of the $4^3S \rightarrow 2^3P$, 471.3 nm emission line increased with power between 300 W and 500 W, however above 500 W the emission remained fairly constant. A similar trend can be seen in the $4^1D \rightarrow 2^1P$, 492.2 nm emission line. The 501.6 nm emission line ($3^1P \rightarrow 2^1S$) demonstrated a steady growth, appearing to grow almost linearly with power. The intensity of the singlet emission line ending on the metastable is around an order of magnitude greater than the intensity of the other emission lines. This is because the rate coefficients for electron excitation from the ground state to the 3^1P state is much larger than the rate coefficients for electron excitation to the $n = 4$ states from the ground state [99].

The ratios calculated were the ratio of the integrated intensity under each individual emission line. Figure 3.16 shows the mean value and standard deviation of the three ratios investigated to find plasma parameters at powers between 300 W and 700 W. As suggested by Boivin [5], the ratios calculated from the steady state corona (SSC) model are shown in Figure 3.17 for comparison. The electron impact excitation rate coefficient C_{ij} for a bi-Maxwellian can be written as [73]

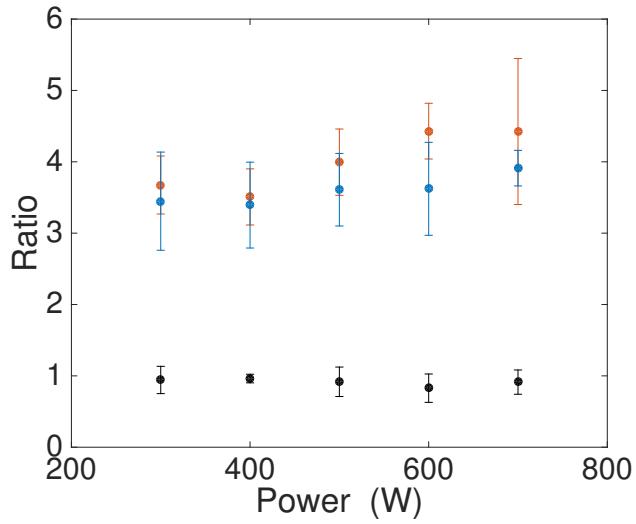

Figure 3.16: Line ratios as a function of input power. The points show the mean value of the ratio and the error bars show the standard deviation: black data points $4^1S \rightarrow 2^1P$ (504.8 nm) / $4^3S \rightarrow 2^3P$ (471.3 nm), orange data points $4^1D \rightarrow 2^1P$ (492.2 nm) / $4^3S \rightarrow 2^3P$ (471.3 nm), blue data points $4^1D \rightarrow 2^1P$ (492.2 nm) / $4^1S \rightarrow 2^1P$ (504.8 nm).

$$C_{ij} = (1-\alpha)C_{ij}(T_e^{cold}) + \alpha C_{ij}(T_e^{hot}). \tag{3.3}$$

The electron impact excitation rate coefficient from the ground state to the states with $n = 4$ decreases rapidly at low temperatures. The atomic cross sections calculated by Kondratyev and Vainshtein [99] give $C_{ij}(0.5\text{ eV})/C_{ij}(2\text{ eV}) < 10^{-7}$ and thus the cold electron fraction in the SSC model can be ignored. The SSC ratios for both $4^1D \rightarrow 2^1P$ (492.2 nm) / $4^3S \rightarrow 2^3P$ (471.3 nm) and $4^1D \rightarrow 2^1P$ (492.2 nm) / 504.8 nm clearly do not match the measured ratios. However the measured line ratio $4^1S \rightarrow 2^1P$ (504.8 nm) /$4^3S \rightarrow 2^3P$ (471.3 nm) is only slightly smaller than the ratio predicted by the SSC model. The mean experimental value of the line ratio is $\sim 0.91 \pm 0.3$ whilst the SSC model predicts ratios between 1 and 1.2 from 2 eV to 5 eV. Values for the ratio $4^1D \rightarrow 2^1P$ (492.2 nm) / $4^3S \rightarrow 2^3P$ (471.3 nm) vary from 3.5 $\pm$ 0.4 to 4.4 $\pm$ 1 and values for the line ratio $4^1D \rightarrow 2^1P$ (492.2 nm) / $4^1S \rightarrow 2^1P$ (504.8 nm) 3.4 $\pm$ 0.6 to 3.9 $\pm$ 0.3. The maximum error on a ratio was $\pm$ 25 %.

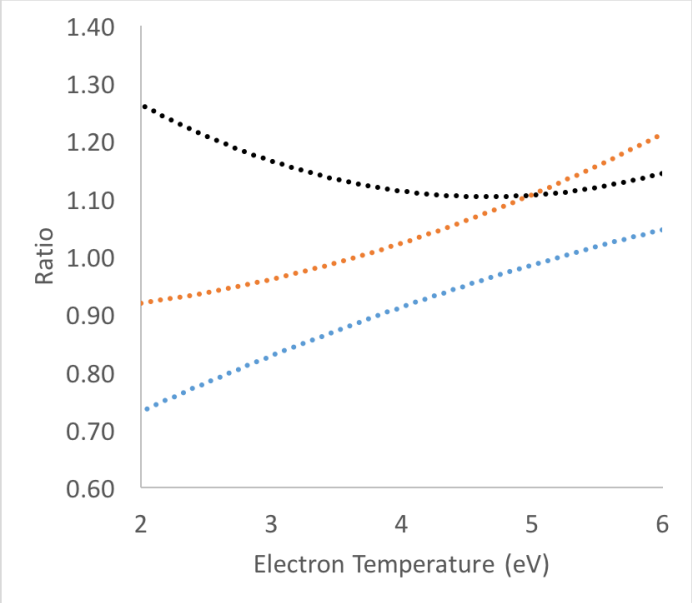

Figure 3.17: Line ratios calculated using the SSC model, black data points $4^1S \rightarrow 2^1P$ (504.8 nm) / $4^3S \rightarrow 2^3P$ (471.3 nm), orange data points $4^1D \rightarrow 2^1P$ (492.2 nm) / $4^3S \rightarrow 2^3P$ (471.3 nm), blue data points $4^1D \rightarrow 2^1P$ (492.2 nm) / $4^1S \rightarrow 2^1P$ (504.8 nm)

Non-LTE, synthetic spectra were created using the collisional radiative model PrismSPECT. The electron distribution function was modelled as a bi-Maxwellian with the two temperature components, T_1 varied from 0.1 eV to 1 eV and T_2, varied from 0.1 eV to 6 eV. Choosing two independent electron densities was not possible. The ratio of the two electron populations, $\Theta = n_e(T_2)/n_e(T_1)$, was varied from 5×10^{-9} to 5×10^{-4}. PrismSPECT accounts for states up to the $n = 10$ level. The simulation has a helium pressure of 1 mbar and a plasma width of 15 cm, matching the conditions within the discharge.

The three ratios $4^1S \rightarrow 2^1P$ (504.8 nm)/ $4^3S \rightarrow 2^3P$ (471.3 nm), $4^1D \rightarrow 2^1P$ (492.2 nm)/$4^3S \rightarrow 2^3P$ (471.3 nm) and $4^1D \rightarrow 2^1P$ (492.2 nm)/ $4^1S \rightarrow 2^1P$ (504.8 nm) were calculated for each synthetic spectra. The synthetic ratios were fitted simultaneously to the data ratios using the method of least squares. Figures 3.18 and 3.19 show examples of synthetic spectra created with PrismSPECT fitted to measured emission spectra, (normalized to the $4^1D \rightarrow 2^1P$ 492.2 nm emission line, Figures 3.18

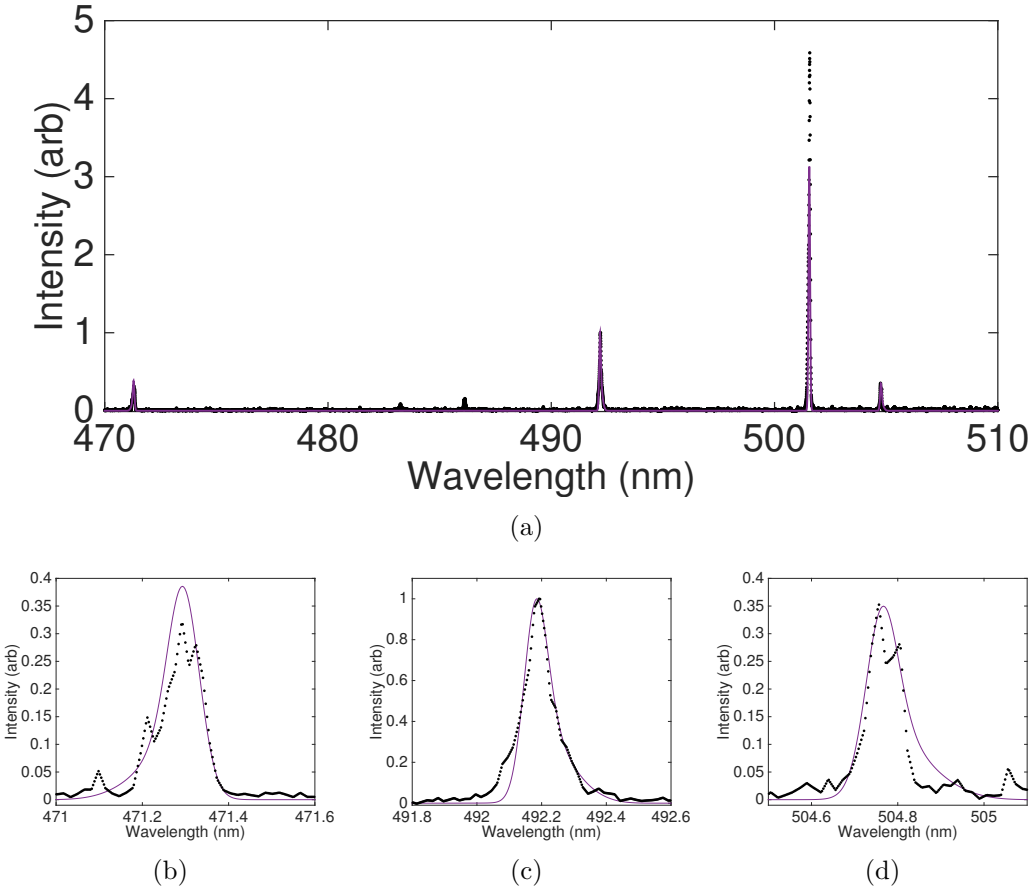

Figure 3.18: A synthetic spectra created with $T_1 = 0.1$ eV, $T_2 = 3.0$ eV $\Theta = 5 \times 10^{-7}$ (purple line) fitted to the data at 400 W (black points). a) The complete spectra. b) Focusing on the emission line at 471.3 nm, ($4^3S \rightarrow 2^3P$). c) Focusing on the emission line at 492.2 nm ($4^1D \rightarrow 2^1P$). d) Focusing on the emission line at 504.8 nm ($4^1S \rightarrow 2^1P$).

c and 3.19 c). The resulting fits are a good match to the data for the $n = 4$ transitions, the differences in line shape are attributed to the variation of the instrument function from a Gaussian. Figures 3.18 b-d and 3.19 b-d focus on individual emission lines. The sensitivity of the extracted parameters to the fit were found by allowing the RMS fitting error to double. The average error on the fitted temperature was found to vary between $T_2^{error} = \pm$ 0.4 eV and $T_2^{error} = \pm$ 0.9 eV, depending on the input power. The error in Θ is a factor of 10 both above and below the fitted value. Figure 3.20 shows the variation of the simulated lines with T_2 and Θ. The black points show

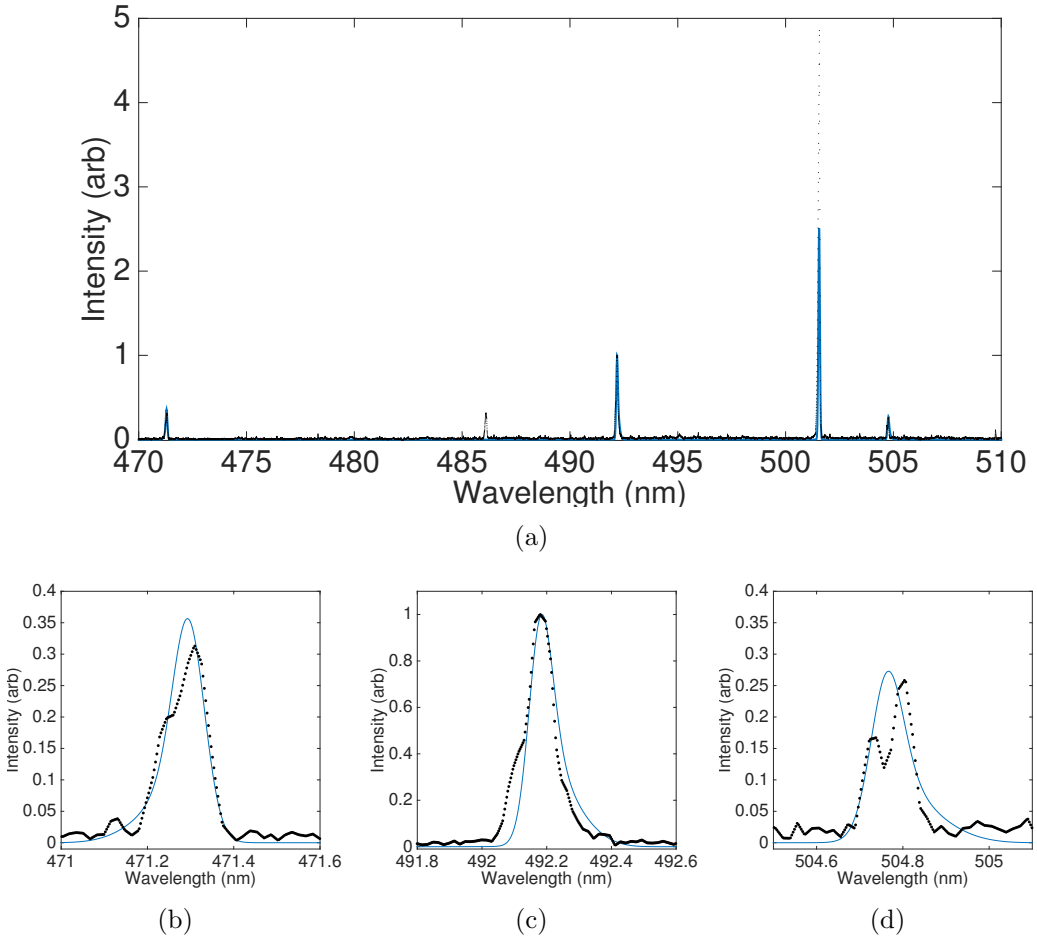

Figure 3.19: A synthetic spectra created with $T_1 = 0.1$ eV, $T_2 = 3.0$ eV, $\Theta = 5 \times 10^{-6}$ (blue line) fitted to the data at 600 W (black points). a) The complete spectra. b) Focusing on the emission line at 471.3 nm ($4^3S \rightarrow 2^3P$). c) Focusing on the emission line at 492.2 nm ($4^1D \rightarrow 2^1P$). d) Focusing on the emission line at 504.8 nm ($4^1S \rightarrow 2^1P$).

a dataset taken at 600 W, where all of the simulated and measured spectra in the figure are normalised to the line at $4^1D \rightarrow 2^1P$ 492.2 nm (not shown in the figure). Figures 3.20 a and 3.20 b show the fitted spectra (blue line), as well as simulations $\pm$ 0.4 eV above the fitted T_2. Figures 3.20 c and 3.20 d show the fitted spectra (blue line), as well as simulations with hot electron fractions 10 times smaller and greater than the fitted Θ. A variation of about 0.4 eV in the simulated electron temperature changes the magnitude of the simulated lines by approximately the same amount as an order of magnitude variation in the hot electron fraction.

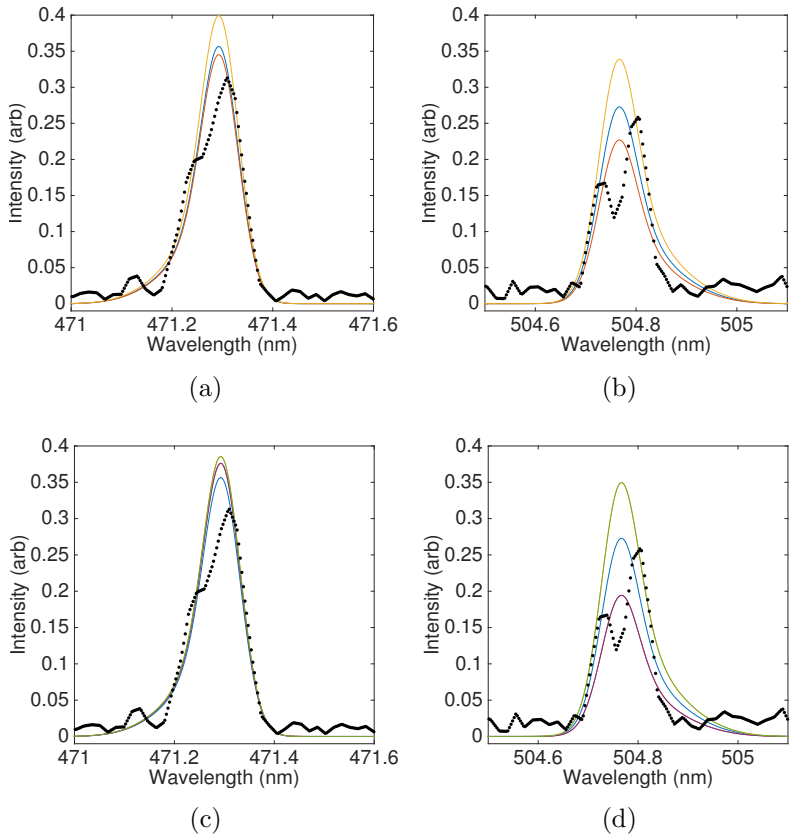

Figure 3.20: The variation in the synthetic spectra with changing electron temperature and density. The synthetic spectra ($T_1 = 0.1$ eV, $T_2 = 3.0$ eV $\Theta = 5 \times 10^{-6}$, blue line) fitted to a data set taken at 600 W (black points). a & b) Show the variation of the synthetic spectra with electron temperature. (orange line: $T_1 = 0.1$ eV, $T_2 = 3.4$ eV, $\Theta = 5 \times 10^{-6}$). (yellow line: $T_1 = 0.1$ eV, $T_2 = 2.6$ eV, $\Theta = 5 \times 10^{-6}$).c & d) Show the variation of the synthetic spectra with hot electron fraction, Θ. (purple: $T_1 = 0.1$ eV, $T_2 = 3.0$ eV, $\Theta = 5 \times 10^{-5}$). (purple line: $T_1 = 0.1$ eV, $T_2 = 3.0$ eV, $\Theta = 5 \times 10^{-7}$).

It is clear in both Figures 3.18 and 3.19 that the 501.6 nm line was not reproduced accurately at the same plasma parameters which simulated the other lines. The most likely reason for this is the strong dependence of the 501.6 nm line on the population density of the metastable level. As discussed in the theory section the ionisation balance equation that is solved in PrismSPECT calculates an equilibrium ionisation based on the bi-Maxwellian EEDF. However it does not account for the diffusion of metastable out from the discharge and therefore the calculation does not find the

metastable densities accurately. The $n = 4$ states discussed above have been chosen to minimise the effects of this, however it clearly has a large effect on the 501.6 nm emission line ending on the 2^1S metastable.

All of the simulated spectra above have $T_1 = 0.1$ eV. When T_1 was increased above 0.1 eV the intensity of both the $4^1S \rightarrow 2^1P$ (504.8 nm) emission line and the $4^3S \rightarrow 2^3P$ (471.2 nm) emission line decreased rapidly. The abrupt disappearance of both the $4^1D \rightarrow 2^1P$ (492.2 nm) and the $4^3S \rightarrow 2^3P$ (471.3) nm emission lines suggests this is a problem with the atomic models. This may be due to errors in the rate coefficients at very low electron temperatures due either to insufficient atomic data or errors in the theoretical models. Figure 3.21 shows a synthetic spectra created with $T_1 = 0.5$ eV, $T_2 = 3.6$ eV and $n_e = 10^{11}$ cm^{-3}, matching the conditions measured by the Langmuir probe. The $4^1S \rightarrow 2^1P$ 504.8 nm emission line and the $4^3S \rightarrow 2^3P$ 471.2 nm emission line are no longer simulated by the model.

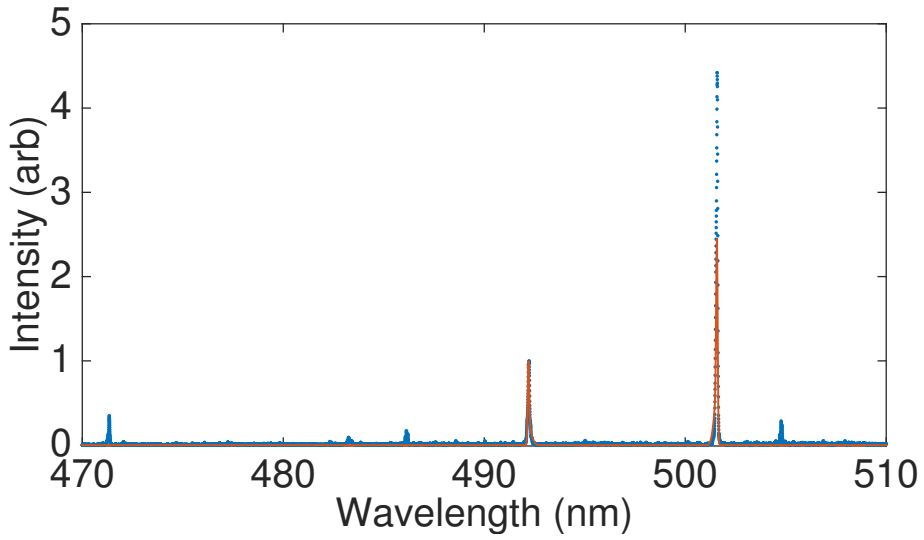

Figure 3.21: A synthetic spectra created with $T_1 = 0.5$ eV, $T_2 = 3.6$ eV, $n_e = 10^{11}$ cm^{-3} fitted to the data at 400 W.

Figure 3.22 a shows the hot electron temperature found for each data set plotted against discharge power. The black data points with error bars show the average of the individual data sets and the standard deviation between them. The hot electron

temperature remains similar across all input powers. The temperature variation due to the fitting error is larger than the error between repeat measurements, giving a minimum combined error of 0.4 eV at 600 W and a maximum combined error of 0.9 eV at 700 W.

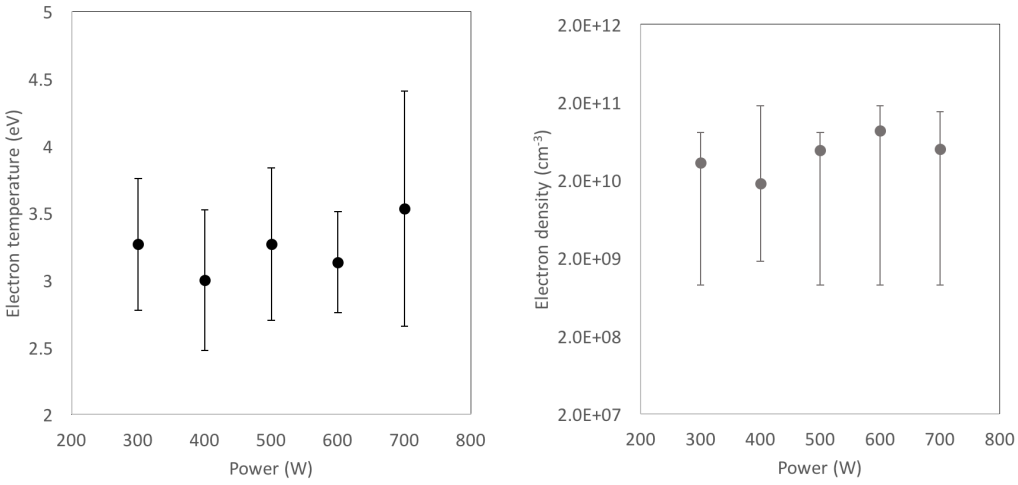

(a) (b)

Figure 3.22: a) The electron temperature vs discharge power. The black data points with error bars show the average hot electron temperature and its standard deviation. b) The cold density vs discharge power. The grey data points with error bars show the average cold electron density, the error bars show the minimum and maximum value.

The measured line ratios only have a very weak dependence on electron density. This is demonstrated as a variation in Θ by a factor of 100 was found by accepting a doubling of the RMS fitting error for an individual spectra. This led to calculated values for the cold electron density between 2×10^{11} cm^{-3} and 9×10^{8} cm^{-3} and calculated values for the hot electron density between 10^{5} cm^{-3} and 10 cm^{-3}. Collisional-Radiative models used by both Sasaki [73] and Boivin [55] found a very weak dependence of the line ratios from the $n = 4$ emission lines at $T_e = 5$ eV and 20 eV below a density $\sim 10^{11}$ cm^{-3}. This can be explained by the dominance of spontaneous emission over collisional de-population processes at low densities $< 10^{11}$ cm^{-3} for the $n = 4$ levels. Individual rate coefficients were calculated by PrismSPECT. The

dominant population methods for $n = 4$ state was electron impact excitation from the ground state and spontaneous emission from states $n > 4$. To find the electron density a ratio should be taken between an emission line from which collisional de-excitation is significant and an emission line which decays predominantly radiatively at a given density [77]. We found this was not provided by the n = 4 levels examined throughout this section.

3.4 Conclusion

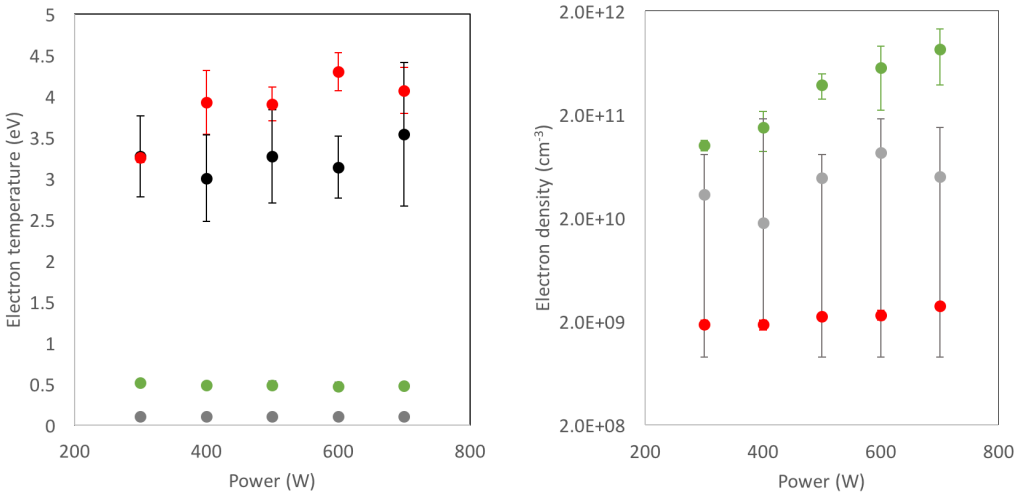

(a) (b)

Figure 3.23: a) The electron temperature vs discharge power. The hot electron temperature inferred using emission spectroscopy (black data points), the hot electron temperature measured by the Langmuir probe (red data points), the cold electron temperature measured by the Langmuir probe (green data points) and the cold electron temperature inferred using OES (grey data points). The error bars on the Langmuir probe data are not visible due the the scale of the y axis. b) The electron density vs discharge power. The cold electron density inferred using emission spectroscopy (grey data points), the hot electron density measured by the Langmuir probe (red data points), cold electron density measured by the Langmuir probe (green data points). The error bars on the Langmuir probe data are not visible due the the scale of the y axis. The error bars on the OES density values show the highest and lowest inferred value.

Figure 3.23a compares the results for the electron temperature found from both

the Langmuir probe and the emission spectroscopy. The hot electron temperatures, T_2 and T_e^{hot} are in good agreement. This suggests that optical emission spectroscopy of particular $n = 4$ states can be analysed by the CR model PrismSPECT to find useful information about a non-equilibrium plasma. Although this technique provides larger errors than the Langmuir probe, the fact that it is non-invasive still provides an important advantage for several applications.

The success of the method appears to rely on the choice of the high neutral states of helium in order to minimise the effects of the metastable states within the discharge. This reliance is suggested by the large error found in modelling the 501.6 nm emission line. To accurately predict the intensity of other emission lines would most likely require a model which accounts correctly for the ionisation mechanisms sustaining the discharge. This model may need to include both the ionisation due to γ electrons and the losses due to electron diffusion of both the hot and cold electron population. The cold electron temperature inferred from the optical emission spectroscopy, $T_1 \sim 0.1$ eV, is lower than the cold electron temperature measured by the Langmuir probe, $T_e^{cold} \sim 0.5$ eV. The abrupt disappearance of both the $4^1D \rightarrow 2^1P$ 492.2 nm and the $4^3S \rightarrow 2^3P$ 471.3 nm emission lines above 0.1 eV suggests the low inferred temperature is due to a problem with the atomic models. This may be caused by errors in the rate coefficients at very low electron temperatures due either to insufficient atomic data or errors in the theoretical models. The line ratios cannot be used to accurately infer the electron and the ratios are also not correctly predicted by the SSC model. At low densities, $< 10^{11}\text{cm}^{-3}$, both Saski *et al* and Boivin *et al* found their simulated ratios to have a very weak dependence on electron density. As the method is insensitive to the electron density, as reproduced here, it has the benefit that the hot electron temperature can be found without the electron density being known. OES can be used to detect variation in the plasma parameters even if they cannot be measured directly. This may be particularly useful in industrial applica-

tions. The plasma could initially be diagnosed with a Langmuir probe, which would then be removed. Any variation from the initial parameters could then be detected using the spectroscopy diagnostic.

3.5 Future Work

Whilst the method presented above found the hot electron temperate with reasonable accuracy, it was less successful in inferring the plasma density and the cold electron temperature. Boivin [55] used a collisional radiative model to find reasonable results for spectroscopic electron densities without considering diffusion or cascades from levels higher than $n = 5$. As PrismSPECT accounts for levels up to $n = 10$, it could give better results than found previously. The low value for the cold electron temperature is most likely due to inaccuracies in the atomic models, but, in the majority of helium plasma sources, the electron temperature is greater than 1 eV. The increase in the ionisation fraction that could be achieved using a different plasma source would also be significant, $\sim 10^3$. Other sources where a similar approach may be appropriate are at the edge of fusion plasma devices [73], where significantly higher temperatures can be achieved.

Successful measurements of the electron densities in γ mode discharges using optical emission spectroscopy requires a more tailored model. The model would have to allow for a bi-Maxwellian temperature distribution with the addition of an external ionisation source, as well as electron diffusion out of the discharge. Whilst this is currently achievable, it is beyond the scope of this investigation.

Chapter 4

Plasma Diagnostics

4.1 Magnetic field diagnostics

4.1.1 Introduction

Magnetic fields play an important role in plasma dynamics and particle acceleration in astrophysics [100–105]. This has led, in the past decade, to a wide range of laboratory experiments aimed at examining the amplification, structure, and dissipation of these fields [38, 39, 106–109]. Clearly, the understanding of the property of the magnetic fields in a plasma requires accurate diagnostics. The magnetic induction (B-dot) probe is a practical, accurate and sensitive instrument, able to make well-resolved field measurements [110]. However, there are several drawbacks. First of all, the B-dot is a mechanical probe that must be inserted into the plasma. This inevitably perturbs the properties of the plasma. To compensate for this, the probe is often miniaturised, such that its linear dimensions are smaller than the relevant spatial scales of interest. A suitable B-dot probe for use in laboratory astrophysics experiments also requires a bandwidth which is fast enough to resolve the dynamics of the flow [110]. These requirements mean a suitable probe is difficult to construct, therefore optical diagnostics may be advantageous. While the Zeeman effect, for example, offers an entirely non-invasive method of measuring the field, the spectral line splitting for typical plasma conditions in these experiments is of the order of other line broadening mechanisms, such as Doppler or Stark broadening [111, 112]. Considering an emission line with wavelength $\lambda = 400$ nm, a $B = 200$ G field gives an induced broadening, due to the Zeeman effect, of $\frac{\Delta\lambda}{\lambda} \sim 10^{-6}$. Faraday rotation of a probe laser is another commonly used technique for the measurements of magnetic fields [113]. However, for optical wavelengths, this requires the product of the magnetic field and plasma density to be large enough, typically requiring electron plasma densities $n_e \sim 10^{18}$ cm^{-3} for an appreciable rotation. For instance in a 1 cm long plasma with a uniform electron density of $n_e = 10^{18}$ cm^{-3} and a uniform magnetic

field $B = 200$ G, the change in the polarisation rotation angle for a 532 nm probe beam would be less than 0.001° [113], which is challenging to measure. Another alternative is the Hanle effect [114], due to the depolarisation of scattered light in atomic transitions involving magnetic sublevels, which may also be used to measure fields in turbulent plasma. This has been applied to diagnose magnetic field in the solar atmosphere. The Hanle effect has the advantage that, while the Faraday rotation cancels out on average in a turbulent magnetic field, the depolarisation does not. However, when considering laboratory plasma conditions, for $n_e \sim 10^{18}$ cm^{-3}, it produces a measurable signal only for fields $B > 1$ kG [115]. In presence of smaller magnetic fields, Faraday rotation measurements are still possible, but they require the use of a small birefringent crystal placed within the plasma to increase the rotation. Magneto-optical probes, relying on this enhancement of the Faraday rotation, have been tested with large current-driven magnetic fields [116–118]. However, to the authors knowledge, they have not yet been used to measure smaller fluctuating magnetic fields in plasmas, nor tested against other diagnostic methods in a plasma. The remainder of this chapter will outline the magneto-optic probe and the magnetic-induction probe. Both of which are used during the experiment discussed in the following chapter.

4.1.2 The Magneto-Optic Probe

As for the usual Faraday rotation, the magnitude of the rotation inside of the crystal depends on the line integral of the component of the magnetic field along the laser path. The rotation angle, Φ, of an electromagnetic wave traveling along the axis of the crystal is given by

$$\Delta\Phi = V \int B(l) dl, \tag{4.1}$$

where V is the Verdet constant, $B(l)$ is longitudinal component of the magnetic field, and l is the length of the crystal. We used a terbium gallium garnet (TGG)

crystal [119], which has $V = 190$ rad/T $\cdot$ m at $\lambda = 532$ nm, the wavelength of probe laser used in our experiment. The average field along the length of the crystal (L) is therefore

$$\langle B \rangle = \Delta\Phi / VL. \tag{4.2}$$

The probe beam was linearly polarised before entering the crystal and split by a 50/50 beam-splitter after passing through the crystal. The polarisation of light after the crystal is given simply by

$$\Phi = \arctan \sqrt{\frac{\epsilon I_s}{I_p}}, \tag{4.3}$$

where I_s and I_p are the intensities of the two orthogonal polarisations, and ϵ is a factor accounting for different losses in each polarisation due to differences in the optical path and varying detector responses. The factor ϵ is found by setting $\epsilon I_s = I_p$ when no magnetic field is present. The polarisation of the probe beam was rotated using a half-wave plate to ensure it was at 45° to the optical axis of the beam-splitter before it passed through the crystal.

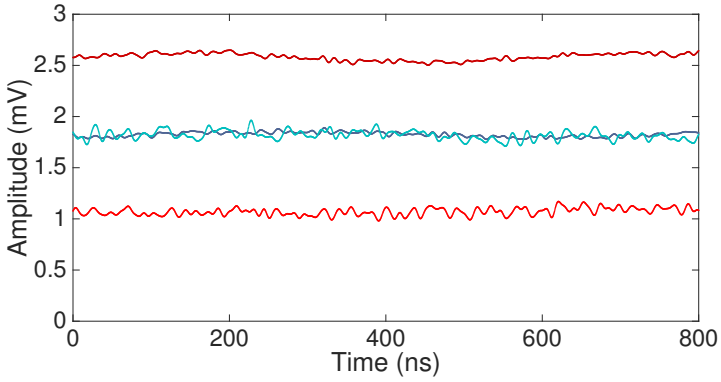

Figure 4.1: Measurements of the light intensity in both the horizontal and vertical polarisations. The dark and light blue lines show the intensities of the horizontal and vertical polarisations when no magnetic field is present. The dark and light red lines show the the horizontal and vertical intensities of the polarisations in the presence of a 1100 ± 10 G permanent magnetic field, (reproduced from [8]).

Figure 4.1.2 shows the response of the magneto optical probe in the 1100 ± 10 G test field of a permanent magnet. The field produced by the permanent magnet

at the location of the Verdet crystal was measured using a Hall probe. The change in the intensity of each polarisation can be seen clearly in Figure 4.1.2 (blue lines no field present, red lines field present). The change in rotation angle as calculated using Equation (4.3) to be $\Delta\Phi \approx 0.2^{rad}$. The magnetic field obtained from Equation (4.2) is $\langle B \rangle \approx 1120 \pm 80$ G, in very close agreement to what expected from the Hall probe measurement. While this calibration was done in DC mode, we also expect that the frequency response of the crystal to be uniform over the range of interest, $f < 100$ MHz.

4.1.3 The Magnetic Induction Probe

The magnetic induction probe used in this experiment was designed and calibrated based on the work by Everson [110]. At its most basic, a magnetic induction probe is no more than a coil of wire protected by a dielectric tube that can be placed inside the plasma. The voltage induced in the coil is then measured to find the magnetic field perpendicular to the plane of the coil. However, a usable probe requires a more sophisticated design. The loop is formed from a pair of wires twisted together, this results in equal but opposite voltages being induced across the two loops due to the magnetic field, however the voltages induced by the electrostatic potentials have the same polarity. This means that when the two signals are subtracted the electrostatically induced voltages cancel. This allows the measured voltage across the loop to be found as a function of the magnetic field. The relationship between the induced voltage and the magnetic field being measured is given by [110]

$$\frac{V_{meas}(\omega)}{B(\omega)} = aN\frac{\omega}{1+(\omega\tau_s)^2}[\omega\tau_s + i] \tag{4.4}$$

where a is the area of the coil, N is the number of turns of wire in the coil, ω is the angular frequency and τ_s is a characteristic response time of the circuit. $\tau_s = \frac{L_s+M}{R_s}$

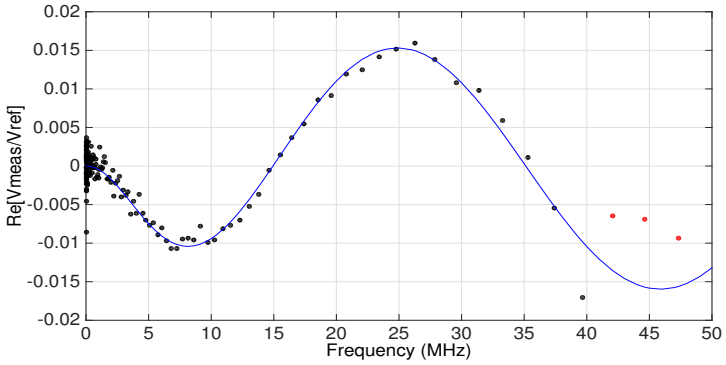

(a)

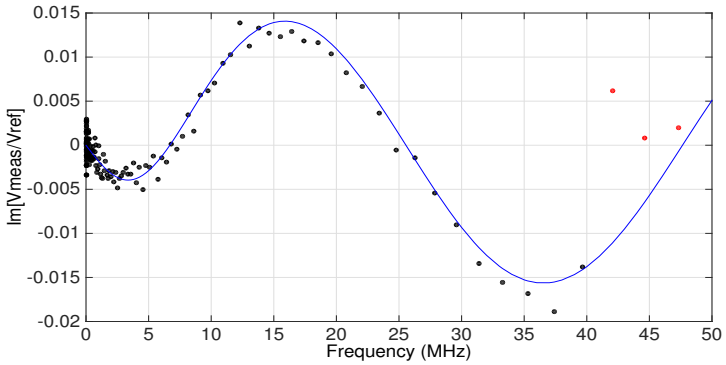

(b)

Figure 4.2: The B-dot probes frequency response plotted from 0 to 50 MHz. The black points indicate data to which the curve was fitted (below 40 Hz). The red points show data outside of this window. The blue curve shows the fitted theoretical curve. a) shows the real part of the data. Fitting parameters: $a = 2.84 \times 10^{-7}$ m^{-2}, $\tau = -22.5$ ns and $\tau_s = 17.8$ ns. b) shows the imaginary part of the data. $a = 2.91 \times 10^{-7}$ m^{-2}, $\tau = -21.6$ ns and $\tau_s = 18.5$ ns.

where L_s is the self inductance of a loop, M is the mutual inductance between the loops and R_s is the load resistance on the loop. The constants a and τ_s must be found experimentally for an individual probe. This is done using a network analyser and a Helmholtz's coil. The network analyser sends an oscillating voltage through the Helmholtz coil while also measuring the voltage across the coil. The voltage measured across the coil is taken as the 'reference voltage' which equates to a reference magnetic field as

$$B(\omega) = (\frac{4}{5})^{3/2} \frac{\mu_0}{r R_p} (2V_{ref}(\omega)), \tag{4.5}$$

where r is the radius of the Helmholtz coil and R_p is the load resistance of the loop. The network analyser also measures the frequency response of the probe when it is placed in the centre of the Helmholtz coil. The calibration is then performed by fitting a theoretical curve to the measured voltage over the reference voltage

$$\frac{V_{meas}}{V_{ref}} = aNg\frac{16}{5^{3/2}}\frac{\mu_0}{rR_p}\frac{\omega}{1+(\omega\tau_s)^2}[\omega\tau_s\cos(\omega\tau) - \sin(\omega\tau) + i(\omega\tau_s\sin(\omega\tau) + \cos(\omega\tau))], \tag{4.6}$$

where a, τ_s and τ (the time delay between the measured and reference signals due to the cable length) are the fitting parameters, g is the gain of the differential amplifier and μ_0 is the permittivity of free space. The real and imaginary parts of the theoretical curve are fitted to the data separately using non-linear least squares analysis in MATLAB. For both the real and the imaginary part of the data the theoretical curve was fitted up to 40 MHz. The fitted calibration data is shown in Figure 4.2. In both cases after 40 MHz the theoretical curve no longer fits the data. Though there is a possibility this is due to the self inductance of the Helmholtz coil at higher frequencies and not due to the B-dot probe itself. As the magnetic field is calculated directly from Equation (4.4) the calibration shows that the bandwidth of the B-dot probe is at least 40 MHz. The differences in the fitting parameters between the real and imaginary parts of the curve are $< 5\%$. We find a = 2.9 $\pm$ 0.7 $\times 10^{-7}$ m^{-3} and $\tau_s = 18 \pm 0.5$ ns found from the above fitting. The small probe area means that in effect the B-dot probe provides almost a point measurement of the field although the glass tube is large.

4.2 Spectroscopy

Information can also be obtained from the plasma by considering the broadening of individual emission lines. The final line width will be given by the convolution of the

several different line broadening mechanisms. In many cases broadening mechanisms can be shown to be negligible due to finite experimental resolution. In Section 5.4 spectral broadening is examined to find the turbulent velocity of the plasma.

4.2.1 Natural Broadening

The most fundamental of all broadening mechanisms is natural broadening which can be seen as an effect of the uncertainty principle, $\Delta E \Delta t \leq \hbar/2$. Letting the lifetime of an excited state be Δt the full width half maximum of natural broadening at a wavelength λ_{ij} is given by [77]

$$\frac{\Delta\lambda_{ij}}{\lambda_{ij}} = \frac{\lambda_{ij}}{2\pi c}\Big(\frac{1}{\Delta t_i} + \frac{1}{\Delta t_j}\Big), \tag{4.7}$$

where Δt_i and Δt_j are the lifetimes of the upper and lower state of the transition. Equation (4.7) can be rewritten in terms of spontaneous emission rate as

$$\frac{\Delta\lambda_{ij}}{\lambda_{ij}} = \frac{\lambda_{ij}}{2\pi c}\Big(\sum_{l<i} A_{li} + \sum_{l<j} A_{lj}\Big), \tag{4.8}$$

where the sum over all transition probabilities with $l < i, j$ accounts for all radiative transitions from the upper state. In the optical region values of $\Delta\lambda_{ij}$ are typically of the order ≈ 5 fm. Therefore natural broadening is orders of magnitude smaller than the instrument function of the spectrometer (typically ~ 0.1 nm) and generally negligible.

4.2.2 The Stark Effect and Electron Impact Broadening

The electrons and ions within a plasma act to perturb emitters due to long range Coulomb interactions. As the perturbation is caused by the Coulomb force it is often

modelled as a collisional process. The perturbation is considered in the two distinct limits defined relative to the natural lifetime of the emitter [120]. Electron impact broadening is due to rapid collisions which have durations shorter than the natural lifetime of a level. Conversely the Stark effect or quasi-static broadening is due to the presence of relatively slow moving ions.

In electron impact broadening the shape of the line is Lorentzian and the full width half maximum frequency can be expressed in terms of elastic and inelastic collision rates. For emission between the states l and h

$$\Delta\omega_{\frac{1}{2}} = N\int_0^\infty \nu f(\nu)d\nu\left(\sum_{l\neq m}\sigma_{lm} + \sum_{h\neq g}\sigma_{hg} + \sigma_{el}\right), \tag{4.9}$$

where N is the density of the perturbers, m and g are the perturbing levels, σ_{lm} is the inelastic collision cross section and σ_{el} is the elastic collision operator, ν is the relative velocity between the emitter and perturber and $f(\nu)$ is the electron Maxwellian velocity distribution [77, 121].

In the quasi-static approximation the electric field due to the ions is considered constant throughout the radiative decay process. The hamiltonian of the perturbation is therefore given by

$$H_{electric} = -\mathbf{E}\cdot\mathbf{D}, \tag{4.10}$$

where $\mathbf{E}$ is the electric field and $\mathbf{D}$ is the electric dipole moment of the atom or ion [120]. Finding the Stark broadening of the spectral lines is complex due in part to the different Stark regimes e.g. linear, quadratic. The first attempt was made by Holtsmark [122] who considered the locations of the perturbing ions all to be statistically independent whist calculating the 'plasma microfield'. The wings of the line profile decay as

$$L(\omega - \omega_{ij}) = \frac{1}{(\omega - \omega_{ij})^{5/2}}, \tag{4.11}$$

slightly faster than a Lorentzian [77].

Electron impact and Stark broadening are accounted for by the collisional radiative code PrismSPECT [80] in our analysis. However an order of magnitude approximation for the full width half maximum of the 429.9 nm CII emission line in a carbon plasma at an electron temperature of 4.3 eV, and an electron density of 10^{17} cm^{-3} is given by [121] as ~ 0.15 nm.

4.2.3 Doppler Broadening

The key broadening mechanism in the experiment described in Chapter 5 is Doppler broadening. A non-relativistic Doppler shift is caused by variations in the velocity of the emitting particles along the line of sight of the spectrometer [77]. When the particles are traveling at a range of positive and negative velocities with respect to the detector, the effect results in a broadening of the emission lines. The relative velocities between the emitters and the detector can be caused by either thermal or bulk motions within the plasma. The example of bulk motion we will consider is turbulence. The full width half maximum of the thermal broadening for a Maxwell-Boltzmann distribution is given by

$$\Delta\lambda = \lambda \sqrt[2]{\frac{8 k_b T_\alpha \ln(2)}{m_\alpha c^2}}, \tag{4.12}$$

where T_α and m_α are the temperature and mass of the emitting particle, α. For a low temperature carbon plasma, ion temperature $T_i \approx 4$ eV, a transition at a wavelength of 400 nm is broadened by $\Delta\lambda = 0.2$ nm. The standard approach to turbulent broadening is to treat it as an additional Gaussian line profile, which can

be convolved with the thermal broadening. The total Doppler broadening velocity, v_{tot}, is thus found by adding the two contributions in quadrature [123]

$$v_{tot}^2 = v_{turb}^2 + v_{th}^2, \tag{4.13}$$

where v_{turb}, is the turbulent velocity and v_{th} is the thermal velocity. With both line profiles approximated by Gaussians the full width half maximum of the convolved profile is simply

$$\Delta\lambda = \lambda\sqrt[2]{\frac{8k_b T_\alpha ln(2)}{m_\alpha c^2} + \frac{v_{turb}^2}{c^2}}. \tag{4.14}$$

It is possible to find both the thermal and turbulent velocities by considering emission lines from ions with distinct masses. Inspection of Equation (4.14) shows the thermal broadening for each ion will depend on its mass whereas turbulent broadening is mass independent. This allows broadening from each individual effect to be uniquely identified.

4.2.4 Zeeman Broadening

The Zeeman effect is caused by the misalignment of a magnetic field and the magnetic moment of an ion [77]. While the exact broadening depends on the energy level being observed, an order of magnitude estimate for a 200 G field at 400 nm (similar to the conditions produced in the experiment described in Chapter 5) is given by

$$\Delta\lambda \approx \frac{\lambda^2 eB}{4\pi mc^2} \approx 10^{-4} \text{ nm}. \tag{4.15}$$

Which is two orders of magnitude smaller than the thermal broadening in the experiment.

4.3 Interferometry

A typical Mach-Zender interferometer is shown in Figure 4.3. An incoming probe beam is split by a 50/50 beam splitter directing half of the light through each of the two arms. The object beam passes through the region containing the plasma before being recombined with the reference beam by a second beam splitter, the resulting interference pattern due to a small offset between each path in the system can then be detected. In order to find the electron density of the plasma the fringe shift which occurs when a plasma is formed in the lower arm must be found [124]. The change in the optical path length $\Delta\delta$ due to a plasma in the beam is given by

$$\Delta\delta = L\ \Delta\mu, \tag{4.16}$$

where L is the path length and $\Delta\mu$ is the change in the refractive index caused by free electrons. Ion density variations also change the refractive index, however, as $\frac{m_i}{m_e} \approx 2000$, the contribution due to the ions is negligible. In the case where $\omega^2 \gg \omega_p^2$, the refractive index of the free electrons is given by

$$\mu = \sqrt{1 - \frac{\omega_p^2}{\omega^2}} \approx 1 - \frac{1}{2}\frac{\omega_p^2}{\omega^2}, \tag{4.17}$$

where the terms beyond the quadrature have been dropped. Assuming that initially there are no free electrons in the lower arm, the initial refractive index is one and

$$\Delta\delta = L\ \Delta\mu = L(\mu - 1) = -\frac{L}{2}\frac{\omega_p^2}{\omega^2}. \tag{4.18}$$

From interferagrams a phase shift $\Delta\phi$ is found which can be related to the optical path difference by

$$\Delta\phi = \frac{2\pi\Delta\delta}{\lambda}. \tag{4.19}$$

The rest of this section will describe how the phase change $\Delta\phi$ can be recovered from an interferogram [9].

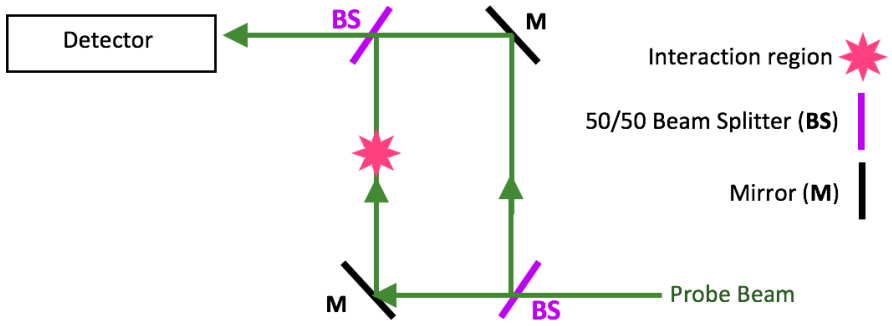

Figure 4.3: A simple Mach-Zender interferometer.

The intensity in the plane of the detector, $I(x, y)$,can be written as

$$I(x, y) = a(x, y) + b(x, y)\cos(\zeta(x, y)), \tag{4.20}$$

where a(x,y) is the background signal, b(x,y) is the amplitude of the interference fringes and $\zeta(x, y)$ is the phase modulation often referred to as the spatial carrier. Considering the case of fringes parallel to the y axis, $\zeta(x, y)$ becomes $\zeta(x) = 2\pi u_0 x$ where u_0 is the carrier frequency. This is the frequency of the fringe pattern when no plasma is present in the object beam, induced by a slight offset of the wavefronts between the reference and object beam. When a plasma is formed in the object beam an additional phase shift occurs, the intensity at the detector becomes

$$I(x, y) = a(x, y) + b(x, y)cos(\zeta(x) + \Delta\phi(x, y)) \tag{4.21}$$

where $\Delta\phi(x, y)$ is the optical phase encoding the electron density in the plasma. Here $\Delta\phi(x, y)$ is found from Equation (4.21) using Fourier transform demodulation. $I(x, y)$

can be rewritten as

$$I(x,y) = a(x,y) + \frac{b(x,y)}{2}(e^{i(\zeta(x)+\Delta\phi(x,y))} + e^{-i(\zeta(x)+\Delta\phi(x,y))}), \tag{4.22}$$

$$= a(x,y) + c(x,y) + c^*(x,y). \tag{4.23}$$

Taking the Fourier transform of both sides one finds

$$\tilde{I}(u,v) = \tilde{a}(u,v) + \tilde{c}(u,v) + \tilde{c}^*(u,v). \tag{4.24}$$

Figure 4.4 a shows raw interferometry sample data and 4.4 b shows the sample data in frequency space at this stage of the analysis. Three distinct features can be seen, the central feature, at the origin, is the first order spectra $\tilde{a}(u,v)$. The two other features are $\tilde{c}(u,v)$ and $\tilde{c}^*(u,v)$. A transfer function, $H(\tilde{u},v)$, can then be applied to $\tilde{I}(u,v)$ such that

$$H(\tilde{u},v)\tilde{I}(u,v) = \tilde{c}(u,v). \tag{4.25}$$

$\Delta\phi(x,y)$ modulo 2π can be found from $\tilde{c}(u,v)$ with knowledge of $b(x,y)$ and the carrier frequency. The unwrapped phase is found modulo 2π due to the periodicity of the inverse trigonometric functions used in the demodulation. The analysis outlined above constrains the allowed carrier frequencies. In Fourier space $\tilde{c}$ will be a distance u_0 from the first order spectra, $\tilde{a}(u,v)$. Therefore u_0 must be large enough such that there is no overlap between the first and second order function, to allow the transfer function to be applied. The carrier frequency must also satisfy the Nyquist-Shannon sampling theorem, $u_0 < \frac{1}{2p_x}$, where p_x is the pixel size of the detector [125].

In order to produce a total phase map (i.e. not modulo 2π) $\Delta\phi(x,y)$ must be unwrapped. Due to the broken fringes caused by the turbulent plasma the phase unwrap was performed using the branch cut method [126, 127]. The branch cut method finds and avoids broken fringes which would otherwise produce errors which

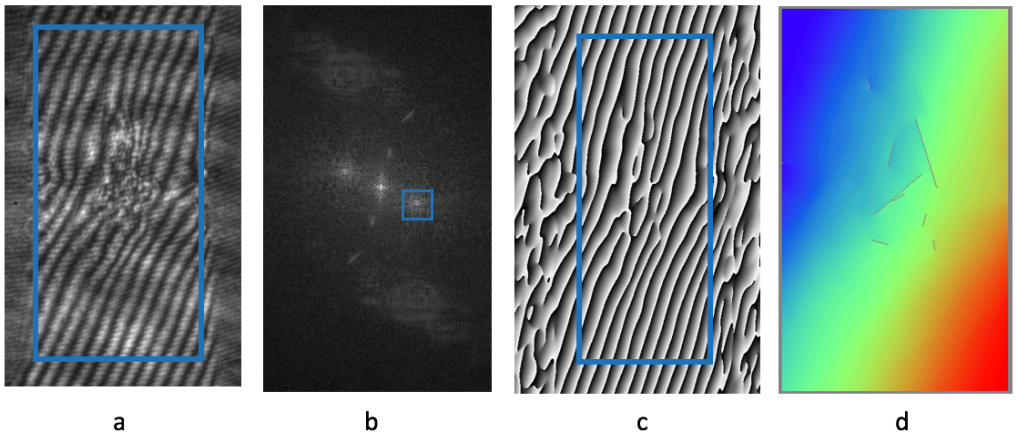

Figure 4.4: An example of data analysed using using the IDEA software [9]. a) Part of a raw interferogram with plasma present, the magnets can be seen on the left and right of the image. The blue box shows the area selected for analysis. b) The Fourier transform of the selected area in image a. The blue box selects a single first order feature from FFT to unwrap. c) The unwrap module 2 π, the same mask is then applied as in a. d) The completed unwrap, several branch cuts can be seen in the centre.

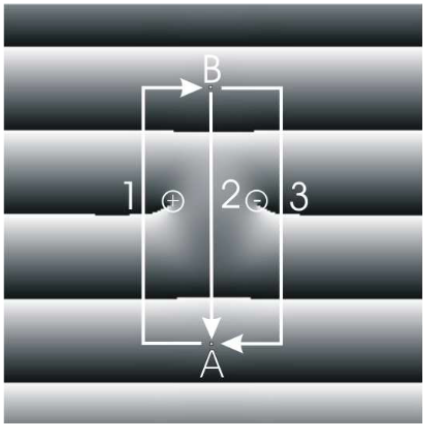

Figure 4.5: Diagram showing the use of the branch cut method to avoid broken fringes. Paths through the broken fringes can thus be avoided, (taken from the IDEA manual [9]).

then propagate through the analysis. To find the broken fringes the number of fringe discontinuities along a closed loop between two points are calculated. Figure 4.5 shows two possible paths between points A and B. Following the path clockwise defined by the arrows labeled 1 and 2, 3 fringe discontinuities are counted along path 1 and 2 fringe discontinuities are counted along path 2. This leads to a residual of +1.

Proceeding clockwise from A to B traveling up path 2 and down path 3, again counting the fringe discontinuities, 2 up and 3 down a residue which is this time negative, -1 is found. These residuals indicate a broken fringe, the branch cut method connects positive and negative residuals and avoids these connections or 'cuts' in the following analysis. Figure 4.4d shows a phase unwrap using the branch cut method [9, 128]. Once paths to ignore have been selected, the phase can then be unwrapped following in effect the 2D scan method. The method counts the number of fringes across an image and shifts the phase by 2π accordingly. The process up to this point is performed on both a data image and a reference image i.e., an image without plasma in the lower arm. The reference image is used to cancel $b(x, y)$ allowing the final phase shift $\Delta\phi(x, y)$ to be found. For radially symmetric plasmas it is usual to Abel invert the line integrated density measurement to find the density distribution. However, as the plasma is turbulent the interferometry results are left as line integrated densities.

4.4 Schlieren Imaging

Gradients in the refractive index of a low density plasma will cause small deflections to a probe beam passing though it. These deflections can be detected using Schlieren imaging and then related back to the free electron density gradients in the plasma. A simple Schlieren imaging system taken from [10] is shown in Figure 4.7. A collimated beam of light, passes through the plasma (test section) and is then brought to focus. If an opaque obstacle is placed at the point of focus the undeflected portion of the beam is blocked and only light refracted within the plasma reaches the screen. Often the unrefracted light is blocked using a 'knife edge', this has the advantage that it is only sensitive to density gradients in the direction orthogonal to the knife-edge. As the electron density n_e, is much less than the critical density n_{crit}, and therefore the refractive index $\mu_r \sim n_e$, the intensity $I(x, y)$ is given by

$$I(x,y) \propto \int \frac{\partial n_e}{\partial x} \mathrm{d}z, \tag{4.26}$$

where x and y are the image plane spatial coordinates, and z is the direction normal to the image plane. To show this we follow the derivation given in [10] for light traveling through a fluid. Consider two points on a wavefront, initially traveling in the z direction, separated by a short vertical distance, z, y and $z, y + \Delta y$. After an interval $\Delta\tau$ the distance traveled by the wavefront is given by

$$\Delta z = \Delta\tau \frac{c_0}{\mu_{RI}(y)} \tag{4.27}$$

where c_0 is the speed of light in a vacuum and $\mu_{RI}(z, y)$ is the refractive index at a point in the fluid. Consider the case where the refractive index is independent of z, but varies in the y direction, $\mu_{RI}(z, y) = \mu_{RI}(y)$. The variation in the refractive index will cause the wavefront to change direction by a small angle $\Delta\alpha$, where $\Delta\alpha$ is given by

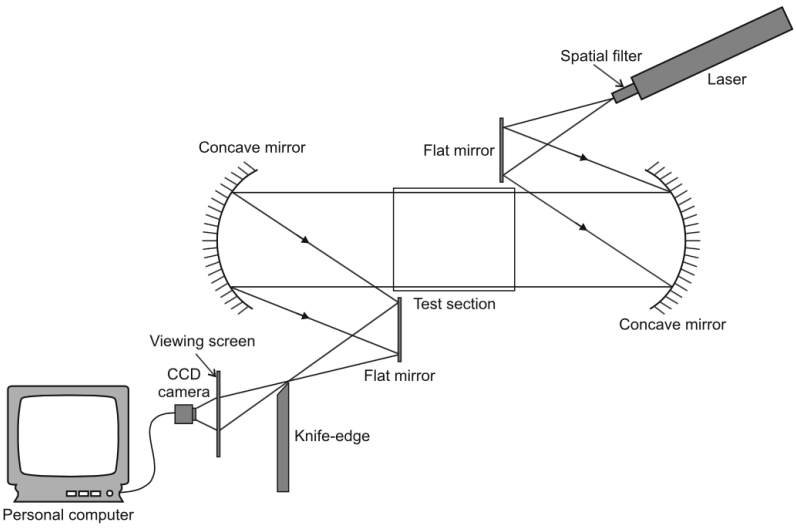

Figure 4.6: A simple setup for performing Schlieren imaging, (Reproduced from [10]). A collimated beam of light passes through the test section. The undeflected light is then blocked using a knife-edge. The deflected light forms an image on the CCD camera.

$$\Delta\alpha \approx \tan(\Delta\alpha) = \frac{\Delta(\Delta z)}{\Delta y}. \tag{4.28}$$

Equation (4.28) can be recast in terms of the refractive index $\mu_{RI}(y)$ as

$$\Delta\alpha \approx -\mu_{RI}(y)\Delta z\frac{\Delta(1/\mu_{RI}(y))}{\Delta y}. \tag{4.29}$$

Considering the limiting case, $\Delta y \to 0$, we find

$$d\alpha = \frac{\partial}{\partial y}\Big(\ln(\mu_{RI}(y))\Big)dz. \tag{4.30}$$

Performing the integral over the length of the fluid, in our case a plasma, we find the total change in angle as the wavefront passes through the plasma

$$\alpha = \int_0^L \frac{\partial}{\partial y}\Big(\ln(\mu_{RI}(y))\Big)dz. \tag{4.31}$$

As the contrast at the detector is proportional to the deflection through the test section, (as long as $1/\mu_{RI}$ does not undergo large variations through the test section [10]), we find

$$I(y) \propto \int \frac{\partial(\mu_{RI}(y))}{\partial y}dz. \tag{4.32}$$

In a plasma $\mu_{RI} \sim n_e$ leading to the expression given in Equation (4.32).

4.5 Summary

This chapter outlines the suite of plasma diagnostics used to study supersonic turbulent jets as discussed in Chapter 5. It began with an introduction on magnetic field measurement techniques and described the calibration of the magnetic induction and the magneto-optic probe, both used to make in-situ field measurements in supersonic

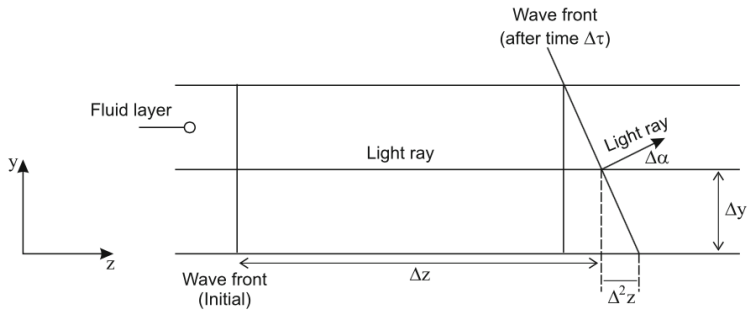

Figure 4.7: The change in direction of a wavefront travelling through a fluid, (Reproduced from [10]).

turbulent plasma. It then continued with outlines of the other diagnostics used during the experiment mainly, interferometry, optical emission spectroscopy and Schlieren imaging. These diagnostics provided information on the density, temperature and velocities within the plasma. The motivation behind the experiment, as well as the results and conclusions drawn, are presented in the next chapter.

Chapter 5

Magnetic Field Measurements in Supersonic Turbulent Jets

5.1 Summary

This chapter discusses an experiment performed on target area west at the Rutherford Appleton Laboratory into magnetic field measurement techniques and supersonic turbulence. Both the magnetic-induction probe and the magneto-optical probe are used to make magnetic fields measurements in low density, supersonic jets. The results of the two measurement techniques are compared. The magnetic-induction probe is then used in calculations of the scaling exponent of the velocity correlation functions. The scaling exponent of the velocity correlation function was found by relating the velocity power spectra to the magnetic power spectra. A suite of diagnostics were used to measure a range of plasma parameters which illustrate that the experiment is comparable to astrophysical situations, i.e. to supersonic turbulence in the interstellar medium (ISM). The results are discussed in relation to astrophysical observations as well as hydrodynamic simulations from the literature. After a short introduction explaining the motivation behind the experiment the experimental setup is presented before the results of each diagnostic are outlined. Finally the experimental conclusions are discussed in detail. The work in this chapter appears in [11] and [8].

5.2 Introduction

The dynamical behaviour of many astrophysical objects are determined by the properties of supersonic turbulence (turbulent Mach number $M_{turb} > 1$). Turbulent velocities in the compressible interstellar medium range from transonic ($M_{turb} \sim 1$) in the warm ionised regions to highly supersonic in molecular clouds, where turbulent Mach numbers can reach up to 20 [129]. In the ISM supersonic turbulence plays a vital role in a number of processes associated with star formation i.e. the rate of star formation triggered by gas compression, the efficiency of star formation itself and the initial mass distribution of stars [130–132]. Self-gravity, magnetic fields,

chemistry, cooling, heating, and radiative transfer all play a role in the dynamics of molecular clouds [133]. However, due to the complexity, studies focusing purely on the hydrodynamic aspects of the problem remain extremely valuable [133–135].

Current analytical models of star formation are based on both the density probability distribution function and velocity power spectra $E(k)$ of the gas, (as a proxy for first order velocity structure function) [132, 136, 137]. Attempts to characterise the statistics of supersonic turbulence have previously been limited to theoretical predictions, numerical simulations and astrophysical observations. Burgers theoretical model for turbulence gives $E(k) \sim k^{-2}$ [138, 139]. A major challenge of the computational approach has been running hydrodynamic simulations large enough to provide sufficient separation between the driving scale and the dissipation scale to allow extraction of the power law exponents for the spectra [133]. Simulations have found a velocity spectrum, $E(k) \sim k^{-2}$ with $M_{turb} \geq 1$ [135] in one dimension and E(k) $\sim k^{-1.8}$ with $M_{turb} \sim 17$ [134] in three dimensions, these results agree well with observations of the Perseus molecular cloud, E(k) $\sim k^{-1.81 \pm 0.1}$, with $M_{turb} \sim 6$ [136].

Previous experimental work has concentrated mainly on the large gradient velocity flows present at compressible turbulent boundary layers relevant to supersonic propulsion [40]. To the authors knowledge, no experimental studies have investigated the statistical properties of boundary-free supersonic turbulence. This chapter describes an experiment to find the scaling exponent of the velocity spectra, E(k), for a supersonic, compressible turbulent flow. Two counter-propagating supersonic jets were launched through laser irradiation of thin fluorinated plastic foils, with the collision forming a central region of strong compressible turbulence, primarily via Kelvin-Helmholtz shearing instabilities. The scaling exponent of the velocity fluctuation power spectrum in the plasma was found by utilising the advection of the externally applied magnetic field as a dynamically unimportant tracer. The exponent of the spatial velocity spectra is obtained through its relationship to the exponent

of the temporal magnetic power spectra as derived in Section 5.4. The ratio of the magnetic energy of the plasma to the kinetic energy of the plasma in the experiment was $\sim 10^{-4}$ showing that the magnetic field was indeed dynamically unimportant. Therefore, the experimental results are compared to the results of hydrodynamic simulations, not magneto-hydrodynamic simulations. Attempts to find temporal magnetic power spectra were made using both a magneto-optic probe and a magnetic-induction probe. After a comparison of the results of the magnetic field measurements made by the two diagnostics, data taken by the magnetic-induction probe was used to find the time varying power spectra, this decision will be explained alongside the results. The results of the measurements made using the magneto-optic probe are presented and discussed as, to the knowledge of the author, this is the first in-situ plasma measurement made using a magneto-optical probe.

5.3 The Velocity Power Spectra

In general, turbulence is examined through its statistical properties. The principal objects of interest are correlation functions. The velocity correlation tensor is defined as

$$Q_{ij} = \left\langle u_i'(\mathbf{x}+\mathbf{r}) u_j'(\mathbf{x}) \right\rangle \tag{5.1}$$

where $u_i'(\mathbf{x})$ is the fluctuations of the velocity field $u_i(\mathbf{x})$, after the mean velocity $\bar{u}_i(\mathbf{x})$ has been subtracted, $u_i'(\mathbf{x}) = u_i(\mathbf{x}) - \bar{u}_i(\mathbf{x})$. This tensor describes the correlation in the velocity field between the two points $\mathbf{x}$ and $\mathbf{x}+\mathbf{r}$. For convenience this tensor is often defined in Fourier space giving the spectrum tensor

$$\phi_{ij}(\mathbf{k}) = \frac{1}{(2\pi)^3} \int Q_{ij}(\mathbf{r}) e^{i\mathbf{k}\cdot\mathbf{x}}. \tag{5.2}$$

Over small distances, $\mathbf{r} \to 0$ it is expected that the velocity fluctuations at the two points will be highly correlated, for example they may be part of the same eddy. Over large distances however $\mathbf{r} \to \infty$, the fluctuations in the velocity at two points should be independent of each other and therefore uncorrelated. Similar correlation tensors can be constructed for other quantities such as magnetic field fluctuations or density fluctuations.

The one dimensional energy spectra of the velocity field is defined as the Fourier transform of the autocorrelation function

$$E(k) = 2\pi|u(k)|^2 = \int_{-\infty}^{\infty}\int_{0}^{\infty} dx\ dr\ u(x)u(x+r)e^{-ikr}. \tag{5.3}$$

The energy spectra picks out the amplitudes of the spatial frequency modes of the velocity autocorrelation function. It is tempting to directly relate this to the contributions of spatial structures of various sizes to the velocity field. However, the energy spectra of a saw-tooth velocity profile gives $E(k) \sim k^{-2}$, however this clearly does not imply that the velocity field is made up of eddies of all sizes. An energy spectra $E(k) \sim k^{-2}$ could, however, be constructed from a continuous distribution of eddys sizes, all with some contribution to the velocity field. This highlights the fundamental problem in the Fourier analysis of the autocorrelation function. Physically different structures can give rise to the same energy spectra in Fourier space. The integral of the energy spectra over all wavenumbers is equal to the total kinetic energy per unit mass in the system

$$\int_{0}^{\infty} E(k)dk = \frac{1}{2}\left\langle \mathbf{u}^2 \right\rangle. \tag{5.4}$$

Despite the issues highlighted above the energy spectra remains a valuable concept. It gives information on the correlation length within the plasma and is a predictable statistical quantity. Analytical models, numerical simulations and experimental ob-

servations all produce predictions for $E(k)$. A hydrodynamic model for the general study of turbulence was introduced by Burgers in 1939 [138, 139]. Considering the case where the mean flow velocity is zero, in one dimension the equation modelling the turbulent velocity fluctuations reduces to the Burgers equation

$$\frac{\partial v}{\partial t} + v\frac{\partial v}{\partial x} = \nu\frac{\partial v^2}{\partial^2 x}, \tag{5.5}$$

where v is the turbulent velocity and ν is the viscosity. Equation (5.5) is the one dimensional Navier-Stokes equation in the limiting case where the sound speed is much smaller than the turbulent velocity and therefore the pressure term can be neglected. Initial interest in the Burgers equation diminished when it was discovered that the equation could be integrated explicitly and therefore it lacked sensitivity to small changes in the initial conditions- a key property of the Navier-Stokes equation [140]. However interest in the Burgers equation was renewed in the 1980's as it was used as a simple model for supersonic turbulence.

The Burgers equation, predicts a velocity spectra, E(k) $\propto k^{-2}$ [135, 138]. This is a steeper spectrum than that found for an incompressible fluid by Kolmorogov, E(k) $\propto k^{-\frac{5}{3}}$ [31]. Burgers' model of turbulence describes a one dimensional system of randomly developing shocks, formed as the turbulent velocity is greater than the sound speed. Heuristically the velocity field can be imagined as a saw tooth profile, leading to the steepening of the spectrum E(k) $\sim k^{-2}$ [135].

5.4 Utilising the Magnetic Field as a Velocity Tracer

The measured quantity in the experiment was the temporally varying magnetic field. The measured magnetic field is directly related to the one dimensional temporal magnetic power spectra as

$$M(\omega) = \frac{1}{4\pi}|B(\omega)|^2 \sim \omega^{\xi}, \tag{5.6}$$

where ξ is a constant over the linear region of the power spectra. However, the quantity of principal interest is the exponent of the spatial velocity power spectra as defined in Equation (5.3). Therefore a relationship between the exponent of temporal magnetic power spectra and the exponent of the one dimensional spatial velocity power spectrum must be found. Schekochihin *et al* [141] related the scaling exponent of the velocity power spectrum to the scaling exponent of the magnetic power spectrum for the case of an incompressible turbulent flow. We perform a similar derivation for a compressible, turbulent flow. It is derived under the assumption that the magnetic field itself is dynamically unimportant (later shown as the ratio of the magnetic energy of the plasma to the kinetic energy of the plasma is $\sim 10^{-4}$). Following this we relate the exponent of the one dimensional spatial magnetic power spectrum to the exponent of the one dimensional temporal magnetic power spectrum.

5.4.1 The One Dimensional Spatial Velocity Power Spectrum in Terms of the One Dimensional Spatial Magnetic Power Spectrum

Consider the magnetic induction equation which relates the magnetic field and the fluid velocity

$$\frac{\partial \mathbf{B}}{\partial t} + \mathbf{u}.\nabla\mathbf{B} = \mathbf{B}.\nabla\mathbf{u} - \mathbf{B}(\nabla.\mathbf{u}) + \eta\nabla^2\mathbf{B}. \tag{5.7}$$

Initially an attempt is made to simplify Equation (5.7). In the presence of a large uniform external field $\mathbf{B}$ may be rewritten as the sum of the externally applied mean field and a small fluctuating component, $\mathbf{B} = \mathbf{B_0} + \delta\mathbf{B}$, where $\delta\mathbf{B} \ll \mathbf{B_0}$ and therefore

Equation (5.7) becomes

$$\frac{\partial \delta \mathbf{B}}{\partial t} + \mathbf{u}.\nabla \delta \mathbf{B} = (\mathbf{B_0} + \delta \mathbf{B}).\nabla \mathbf{u} - (\mathbf{B_0} + \delta \mathbf{B})(\nabla.\mathbf{u}) + \eta \nabla^2 \delta \mathbf{B}. \tag{5.8}$$

When the magnetic Reynolds number R_m is small, the diffusion term dominates the nonlinear terms and the time derivative (quasi static approximation [142]). To see that the time derivative can be neglected consider the magnetic Reynolds number. The magnetic Reynolds number is the ratio of the characteristic time scale for diffusion to the time scale for turbulent motion. Therefore at small magnetic Reynolds numbers, $R_m < 1$ the diffusion time is shorter than the time scales for turbulent motion and and the magnetic fluctuations adapt instantaneously to the velocity field. Under these assumptions

$$\eta \nabla^2 \delta \mathbf{B} = -(\mathbf{B_0}.\nabla)\mathbf{u} + \mathbf{B_0}(\nabla.\mathbf{u}). \tag{5.9}$$

By taking the spatial Fourier transform of 5.9 one finds

$$\eta k^2 \delta \tilde{\mathbf{B}} = i(\mathbf{k}.\mathbf{B_0})\tilde{\mathbf{u}} - i\mathbf{B_0}(\mathbf{k}.\tilde{\mathbf{u}}), \tag{5.10}$$

where, the $\sim$ superscript is used to denote a Fourier transformed quantity. Compared to the incompressible case [141], there is an additional term on the right-hand side as $\nabla.\mathbf{u} \neq 0$. Changing variables to absorb the constants $\tilde{\mathbf{b}} = \frac{\delta \tilde{\mathbf{B}}}{B_0}\eta k^2$, and choosing $\mathbf{B_0}$ to point only in the x-direction, Equation (5.10) becomes

$$\tilde{\mathbf{b}} = i(\mathbf{k}.\hat{\mathbf{x}})\tilde{\mathbf{u}} - i\hat{\mathbf{x}}(\mathbf{k}.\tilde{\mathbf{u}}), \tag{5.11}$$

where $\hat{\mathbf{x}} = (1, 0, 0)$.

Now the properties of the velocity field itself are considered. The velocity spectrum tensor is the Fourier transform of the real space velocity correlation function.

Assuming the dynamics of the turbulence are unaffected by $\mathbf{B_0}$ and the turbulence itself is isotropic (i.e. depends only on the magnitude of k), the velocity spectrum tensor can be written as the sum of a symmetric and an antisymmetric tensor [29]. The symmetric spectrum tensor itself is split into an incompressible and compressible component

$$\langle \tilde{u}_i \tilde{u}_j^* \rangle = I(k)\Big(\delta_{ij} - \frac{k_i k_j}{k^2}\Big) + C(k)\frac{k_i k_j}{k^2} + H(k)\epsilon_{ijl}\frac{k_l}{k}. \tag{5.12}$$

$I(k)$ is associated with the compressible component of the turbulence, $C(k)$ is associated with the incompressible component of the turbulence and $H(k)$ is associated with the helical component of the turbulence. As the turbulence is isotropic each of the terms $I(k)$, $C(k)$ and $H(k)$ depend only on $|\mathbf{k}|$. From Equation (5.11) the spectrum tensor of $\tilde{\mathbf{b}}$ can be expressed as

$$\begin{aligned} \langle \tilde{b}_i \tilde{b}_j^* \rangle = \quad & k_x^2 \langle \tilde{u}_i \tilde{u}_j^* \rangle + \hat{\mathbf{x}}_i \hat{\mathbf{x}}_j k_m k_n \langle \tilde{u}_m \tilde{u}_n^* \rangle \\ - \quad & k_x k_m \hat{\mathbf{x}}_i \langle \tilde{u}_m \tilde{u}_j^* \rangle - k_x k_n \hat{\mathbf{x}}_j \langle \tilde{u}_i \tilde{u}_n^* \rangle. \end{aligned} \tag{5.13}$$

Which upon substitution of Equation (5.12) gives

$$\langle \tilde{b}_i \tilde{b}_j^* \rangle = I(k)k_x^2(\delta_{ij} - \frac{k_i k_j}{k^2}) + H(k)k_x^2\epsilon_{ijl}\frac{k_l}{k} \tag{5.14}$$

$$+C(k)(\frac{k_x^2}{k^2}k_i k_j + k^2 \hat{\mathbf{x}}_i \hat{\mathbf{x}}_j - k_x \hat{\mathbf{x}}_i k_j - k_x \hat{\mathbf{x}}_j k_i). \tag{5.15}$$

The parallel and perpendicular components (with respect to the mean field, $\mathbf{B_0}$) of $\langle \tilde{b}_i \tilde{b}_i^* \rangle$ are now considered separately. For the direction perpendicular to the externally applied mean magnetic field (i.e. y)

$$\langle|\tilde{b}_y|^2\rangle = I(k)k_x^2(1-\frac{k_y^2}{k^2}) + C(k)\frac{k_x^2k_y^2}{k^2}. \tag{5.16}$$

To convert the components of this spectrum tensor ($\langle|\tilde{b}_y|^2\rangle$) into one dimensional energy spectra of $\tilde{\mathbf{b}}$ denoted by m_y, integration over a spherical surface is performed. Upon substitution of $k_x = k\cos\theta$ and $k_y = k\sin\theta\sin\phi$

$$\begin{aligned} m_y &= \int_0^{2\pi} d\phi \int_0^{\pi} d\theta k^2 \sin\theta \langle|\tilde{b}_y|^2\rangle & (5.17)\\ &= I(k)k^4 \int_0^{2\pi} d\phi \int_0^{\pi} d\theta \sin\theta\cos^2\theta(1-\sin^2\theta\sin^2\phi)\frac{1}{4\pi} & (5.18)\\ &+ C(k)k^4 \int_0^{2\pi} d\phi \int_0^{\pi} d\theta \sin\theta\cos^2\theta\sin^2\theta\sin^2\phi\frac{1}{4\pi}. & (5.19) \end{aligned}$$

After integration we obtain the one dimensional energy spectra

$$m_y = \frac{k^4}{15}(4I(k) + C(k)). \tag{5.20}$$

Repeating the analysis for the measurement in the direction parallel to the magnetic field (i.e. x) we get

$$\langle|\tilde{b}_x|^2\rangle = I(k)k_x^2(1-\frac{k_x^2}{k^2}) \tag{5.21}$$

$$+C(k)(\frac{k_x^4}{k^2} + k^2 - k_x^2 - k_x^2) \tag{5.22}$$

and therefore

$$m_x = k^2 \int_0^{2\pi} d\phi \int_0^{\pi} d\theta \sin\theta k^2 [I(k)\cos^2\theta(1-\cos^2\theta)\frac{1}{4\pi} \tag{5.23}$$

$$+ \quad C(k)(\cos^4\theta + 1 - 2\cos^2\theta)]\frac{1}{4\pi}. \tag{5.24}$$

Finally after the integration

$$m_x = \frac{k^4}{15}(2I(k) + 8C(k)) \tag{5.25}$$

is obtained. Solving Equations (5.20) and (5.25) simultaneously we find

$$I(k) = \frac{1}{2k^4}(8m_y - m_x) \tag{5.26}$$

$$C(k) = \frac{1}{k^4}(2m_x - m_y). \tag{5.27}$$

The helical component $H(k)$ has been lost as $< |b_x|^2 >$ and $< |b_y|^2 >$ contain repeated indices. The quantity we are interested in computing is the one dimensional velocity power spectrum. Referring back to the spectrum tensor in Equation (5.12), and substituting in $I(k)$ and $C(k)$, we obtain

$$\langle |u_y|^2 \rangle = I(k)(1 - \frac{k_y^2}{k^2}) + C(k)\frac{k_y^2}{k^2}, \tag{5.28}$$

and for the total energy

$$\langle |u_i|^2 \rangle = 2I(k) + C(k). \tag{5.29}$$

Which after inserting expressions for I(k) and C(k) from (5.26) gives

$$\langle |u_i|^2 \rangle = \frac{1}{k^4}(7m_y + m_x). \tag{5.30}$$

Once again performing the angular integration to find the one dimensional velocity power spectrum

$$E(k) = 4\pi k^2 \langle |u_i|^2 \rangle = 4\pi \frac{1}{k^2}(7m_y + m_x). \tag{5.31}$$

Finally, recalling that the power spectrum of $\tilde{\mathbf{b}}$, denoted m varies from the power spectrum of the magnetic fluctuations $\delta\tilde{\mathbf{B}}$, denoted M as

$$\frac{m_y}{M_y} \propto k^4, \tag{5.32}$$

we obtain

$$E(k) \propto k^2(7M_y + M_x). \tag{5.33}$$

Hence the velocity power spectrum can be retrieved from measurements of the magnetic power spectra both parallel and perpendicularly to the external field direction. In our experiment we find similar spectra in the two orthogonal directions, see Figure 5.14, and hence we set $M_y = M_x = M(k)$, where we have included the explicit dependence on k.

5.4.2 Relationship Between the Temporal and Spatial Power Spectra

The discussion above derived a relationship between the spatial velocity power spectra and the spatial magnetic power spectra. However, the induction loop measures temporal variations in the magnetic field. If the plasma is swept past the probe at velocities such that the evolution of the field within a fluid parcel is negligible whilst the field in that parcel is being measured the spatial and temporal spectra can be related using Taylor's hypothesis, $l \sim t$. This suggests the fluid parcels are effectively 'frozen in' over the time scales at which the field is measured. However the plasma flow does not satisfy these conditions as the plasma will stagnate around the probe due to both the collision of the jets and the presence of the probe shielding, $\sim$ 2mm. One might then argue that the outer-scale structures break around the probe and there is a flow of structures of all sizes against and past the shield. The induction loop will therefore see the Lagrangian-frequency spectrum, rather than the Eulerian one, i.e., for each scale ℓ, it will detect the lifetime of the magnetic structures of size ℓ. Therefore the eddies measured by the probe evolve at approximately the turnover time of the eddie $\omega \approx u(l)/l$.

Using this approximation a relationship between the spatial and the temporal power spectra using Equation (5.33) is derived. We begin by assuming that a simple power-law dependence holds for velocity and magnetic field at the scale ℓ, i.e.

$$u(\ell) \sim \ell^{\alpha} \quad B(\ell) \sim \ell^{\beta}, \tag{5.34}$$

where α and β are constants to be determined. The corresponding one dimensional power spectra are then described by

$$E(k) \sim k^{-(2\alpha+1)} \quad M(k) \sim k^{-(2\beta+1)}. \tag{5.35}$$

For an isotropic, steady state flow the frequency-resolved magnetic-energy spectra can similarly be written as

$$M(\omega)\omega \sim |B(\ell)|^2 \sim \ell^{2\beta}. \tag{5.36}$$

Since $\omega \sim u(\ell)/\ell \sim \ell^{\alpha-1}$, thus $\ell \sim \omega^{1/(\alpha-1)}$, we can recast (5.36) as

$$M(\omega)\omega \sim \omega^{\frac{2\beta}{\alpha-1}}. \tag{5.37}$$

Eq. 5.33 provides the relationship between α and β as $\beta = \alpha + 1$. Hence, we obtain

$$M(\omega) \sim \omega^{\xi}. \tag{5.38}$$

with $\xi = \frac{\alpha+3}{\alpha-1}$. Recall the the exponent of the spatial velocity spectrum was given by $\sigma = -(2\alpha+1)$. Thus, by measuring the spectral index of $M(\omega)$ in the experiment we can obtain a value for the coefficient α and hence the slope of the spatially resolved velocity power spectrum $E(k) \sim k^{\sigma}$.

5.5 Experimental Overview

A diagram of the interaction region is shown in Figure 5.1. Each of supersonic turbulent jets were created by firing three 2 ns, 133 $\pm$ 20 J, 527 nm drive beams onto a 15 μm thick (PVDF) target inside of a vacuum chamber with a base pressure of P $\approx 10^{-5}$ mbar. The drive beams had an approximately Gaussian profile and had a focal spot diameter of d $\approx 200 \pm 20$ μm. The jet then passed through the central hole of a 5 kG ring magnet, (2.5 cm outer diameter, 0.8 cm aperture and 0.6 cm thickness), 1.0 cm from the foil. The field of the permanent magnets was normal to the surface of the foil targets. Each jet then passed through a 0.10 cm nominal aperture and 0.05 cm filament ETFE grid, mounted on the surface of the magnets. The centre of the

apertures in one grid were aligned to the the vertices of the apertures in the second grid. Figure 5.5 shows the strength of the magnetic field on-axis (black) and 0.25 cm off-axis (red). B_x, is parallel to the direction of the flow and B_y, is perpendicular to the direction of the flow, as shown in Figure 5.1. The field strength was calculated using the FEMM finite element code [143].

The supersonic turbulent jets collided at the central point between the two magnets. The same 532 nm, $\sim$5 ns probe beam was used for both the interferometry and and Schlieren imaging systems. The interferometry and Schlieren imaged at 90° to the plasma flow, looking directly down between the two magnets, along the y direction in Figure 5.1. The interferometry was used to find the electron density and the Schlieren imaging was used to find an approximate plasma velocity. The emission spectroscopy imaged a line in the plane between the centre of the two magnets, along the x direction. All the diagnostics were triggered from the Q switch of the main drive beams. When used, both the B-dot and magneto-optic probe were placed in the centre of the interaction region, between the two magnets, at the points where the jets collided, 1.0 cm away from each magnet and 2.0 cm away from the target.

The six infrared drive beams were frequency doubled to 527 nm in order to increase laser coupling to the front surface of the target. The energy obtained from each beam was optimised by adjusting the alignment of the frequency doubling crystals. Each beam was fired onto a calorimeter whilst the beam remained expanded and the number of counts reaching the calorimeter were maximised. The final conversion efficiencies were between 40% and 50%. The six drives beams were timed on a streak camera to within 100 ps, by looking at the reflected light from a scattering target. The combined intensity of three drive beams on a single foil was, I $\approx 5 \times 10^{14}$ Wcm^{-2} and therefore the candidates for the principle absorption mechanisms were inverse bremsstrahlung in the underdense corona, resonant absorption at the critical surface

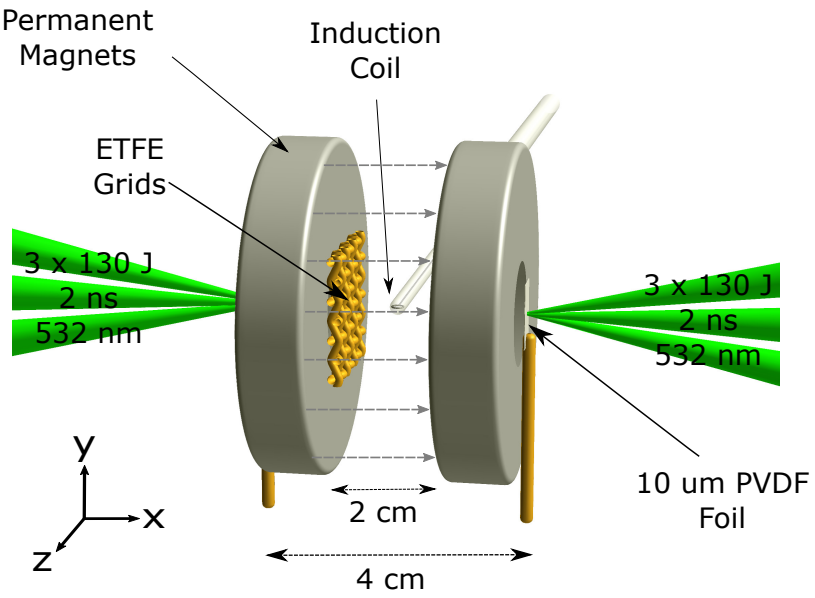

Figure 5.1: Experimental schematic, (reproduced from [11]). Two counter-propagating supersonic jets are launched through optical laser ablation of thin fluorinated plastic foils separated by 4.0 cm. Each foil is irradiated by three frequency-doubled (527-nm-wavelength) lasers, each with 130 ± 20 J in a 2 ns pulse length. The jets are passed through two misaligned plastic grids and collide forming a central region of supersonic turbulence. A magnetic field aligned parallel to the bulk flow (gray dashed lines) is used as a tracer to extract velocity fluctuations from magnetic fluctuations.

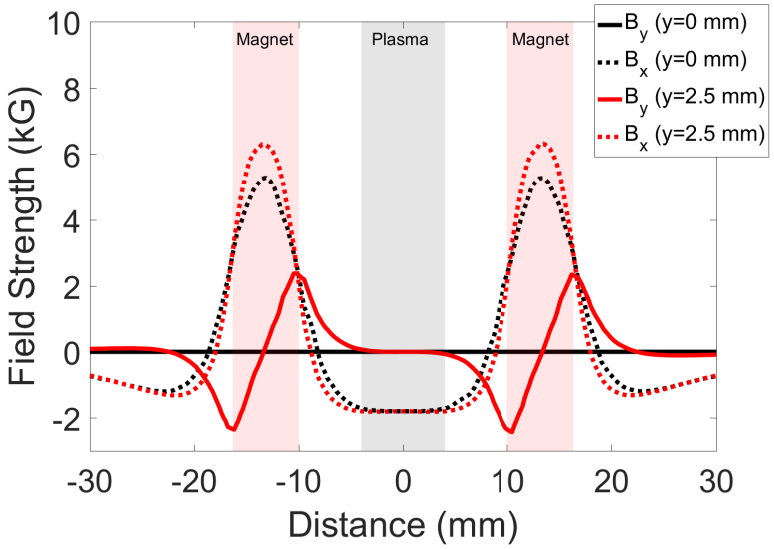

Figure 5.2: Diagram showing the variation in field strength between the two magnets, (reproduced from [11]).

and absorption due to ion acoustic turbulence [46]. Phase plates were used in order to reduce hot spots and create a more uniform plasma flow out of the rear surface. Ablation pressure created by heating at the front surface of the foil forced the dense target material inwards, launching a shock within the target. When the shock reaches the back surface of the foil, a rarefaction wave is produced and a supersonic plasma jet is formed.

5.5.1 Spectroscopy

The spectroscopy diagnostic was performed with an imaging spectrometer coupled to an intensified Princeton Instruments PI-MAX CCD camera with a 20 ns gate width. A simplified schematic of the optical path is shown in Figure 5.3 and a diagram showing the Acton SP-2750 spectrometer [12] is shown in Figure 5.4. The optical path for the spectrometer imaged out of plane and therefore required a dovetailed prism to rotate the image of the interaction region such that the direction of plasma flow was parallel to the entrance slit of the spectrometer. The overall magnification between the object and the imaged formed on the slit was 0.17.

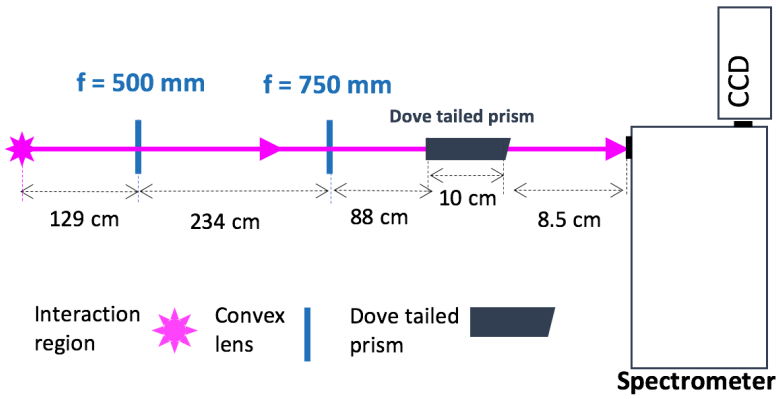

Figure 5.3: A simplified diagram of the optical path used for the optical emission spectroscopy diagnostic.

To correct for the effects caused by the transmission/reflection of optics, and for any spatial variation in the camera sensitivity, the spectrometer was calibrated using

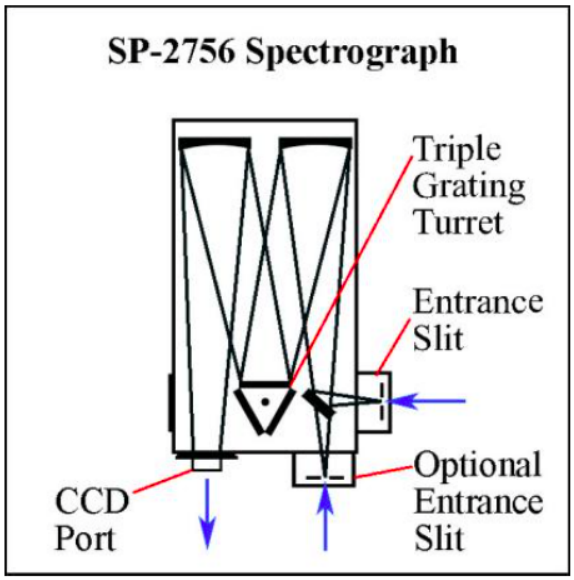

Figure 5.4: Schematic representation of the SP-2756 spectograph used in the experiment. Light emitted from the plasma is focused onto the entrance slit. The light is then collimated by the first mirror, diffracted by the 300 lines per mm grating, and finally focused onto the CCD. Reproduced from [12].

a known while light source. The calibration is performed by placing the known white light source in the region where the plasma is formed and directing the source along the optical path towards the spectrometer. The resultant measured spectra can then be divided by the known transmission curve, producing a correction factor to be applied to the data. Due to the interest in spatial variation of the spectra the white light calibration image, Figure 5.5 a had to be 'sliced' along the spatial direction before the division of the spectrum by the known white light source could be performed. Over the region of interest there was found to be negligible spatial variation in the transmission function. A typical transmission function is shown in Figure 5.5 b. The spectral calibration of the spectrometer was performed with a mercury lamp using the 404.6 nm, 407.8 nm and 435.8 nm lines giving 17.6 pixels/nm dispersion. The raw calibration image is shown in Figure 5.6 a and a figure showing a line out taken with pixels converted to wavelength is shown in Figure 5.6 b. This region was chosen as it contains the spectral lines with the highest intensities in the optical region. In

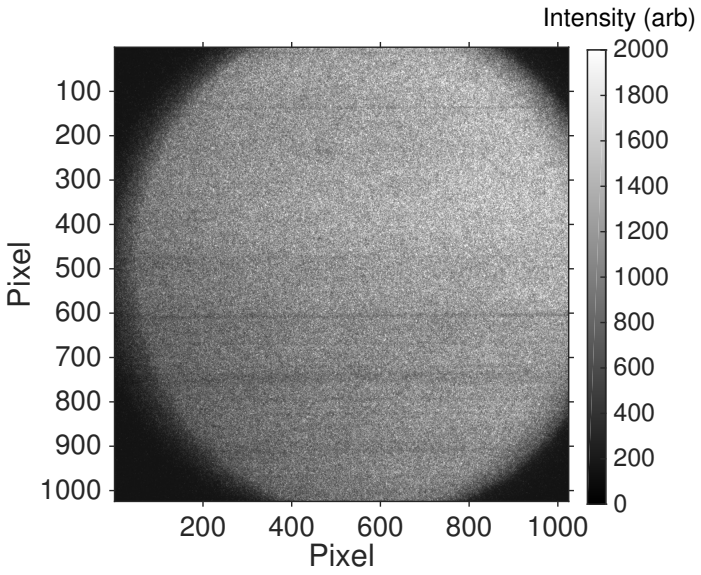

(a)

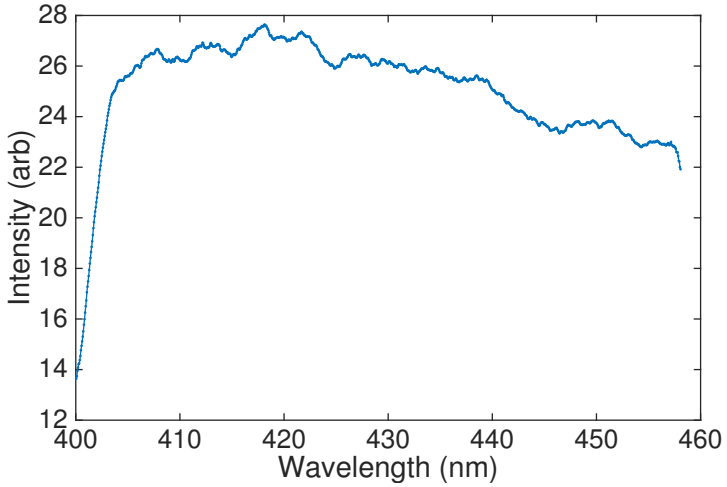

(b)

Figure 5.5: a) The raw image of a white light source taken using the spectroscopy diagnostic. b) The transmission curve for the spectroscopy diagnostic.

order to find the spectral resolution of the spectrometer a Gaussian was fitted to the to the highest intensity peak of the mercury spectrum, at 435.8 nm. The full width half maximum of the peak was found to be ~ 0.25 nm, giving a spectral resolution of $\lambda/\Delta\lambda \sim 2000$. The spatial resolution was set by the 50 μm slit of the spectrometer.

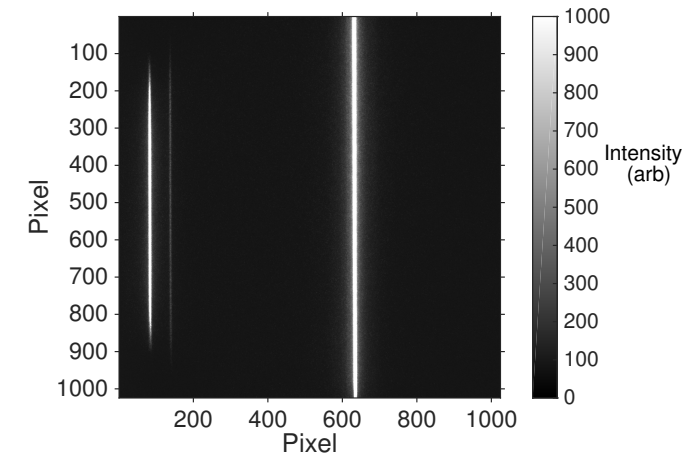

(a)

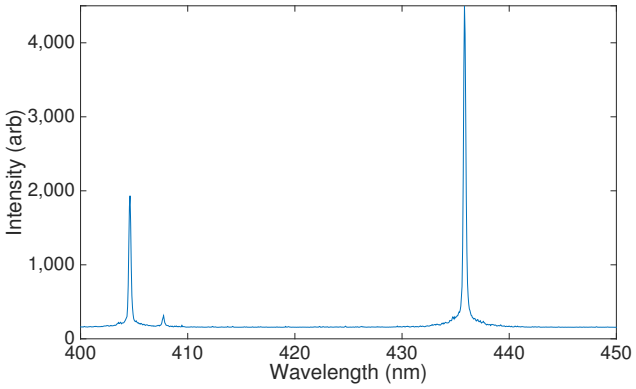

(b)

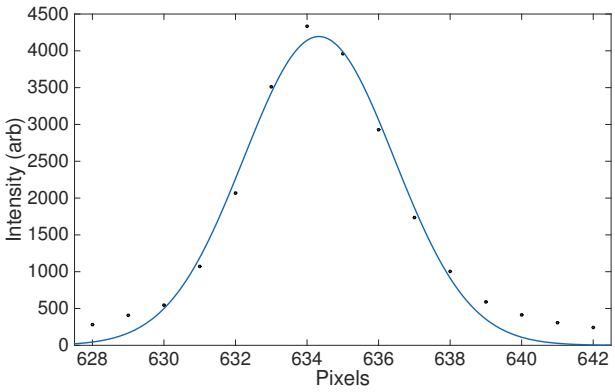

(c)

Figure 5.6: The spectral calibration of the spectrometer. a) The raw image of a mercury source taken using the spectroscopy diagnostic. b) The calibrated mercury spectrum. c) A Gaussian line profile (blue line) fitted to the instrument function of the spectrometer (black data points).

5.5.2 Interferometry

The probe beam for the interferometer was a Photonic Solutions Powerlite Nd:YAG Laser frequency doubled to 532 nm with a ∼5 ns pulse length. The interferometry setup is shown in Figure 5.7. The probe beam was expanded using an f = 100 m concave lens and then re-collimated using a f = 750 convex lens, expanding the beam diameter to 60 mm, and allowing the entire interaction region to be imaged. The expanded probe beam was then sent into the chamber where the Mach-Zender interferometer was constructed. The two f = 950 mm lenses after the interferometer were part of the Schlieren setup built using the same optical path. The fringe pattern was demagnified, M ∼ 0.27, onto the CCD using an f = 750 mm followed by a f = 200 mm lens 750 mm apart. The images were recorded on an intensified Princeton Instruments PI-MAX CCD camera with a 4 ns gate width.

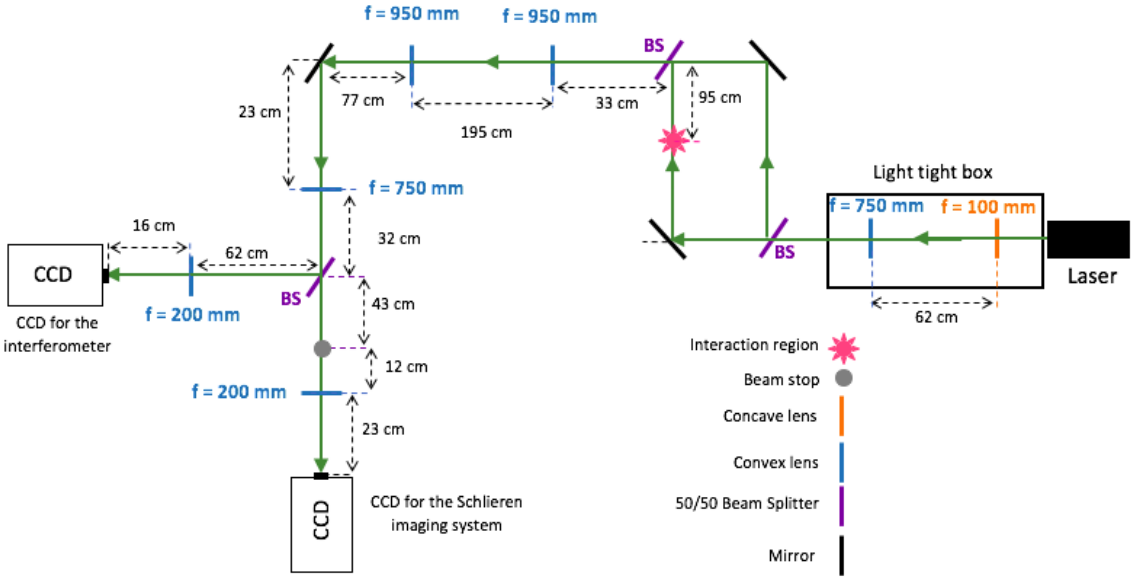

Figure 5.7: Diagram showing the setup of both the Schlieren imaging and interferometer setup

5.5.3 Schlieren

The Schlieren imaging set-up can be seen in Figure 5.7. In the case of the Schlieren diagnostic only the light travelling through the interaction region contributes to the final image, the light in the reference arm is undeflected and therefore blocked by the knife edge. The two 950 mm focal length lenses transport the image formed by the deflected light. Three inch (76.2 mm) diameter lenses were used to capture as much light as possible from the interaction region. The 750 mm focal, length 2 inch (50.8 mm) diameter lens then focused the undeflected light onto the knife edge. Finally the 200 mm focal length, 2 inch (50.8 mm) diameter lens, brought the image formed by the deflected light to focus on the CCD. The magnification of the entire system was M $\sim$ 0.27.

5.5.4 Magnetic Probes

The terbium gallium garnet (Verdet) crystal was held in the centre of the colliding jets using an open-ended ceramic tube (outer diameter 2.5 mm, inner diameter 1.3 mm), with the axis of the crystal perpendicular to the incoming jets. It was only possible to measure $B(z)$ using the magneto-optic probe, $B(z)$ however, can be equated to $B(y)$ due to the cylindrical symmetry. The crystal had a diameter of 1 mm and a length of 10 mm. The purpose of the ceramic tube was to protect the Verdet crystal from direct exposure to the plasma flow, as thermal heating can change its birefringence properties [144]. Indeed, we estimate the time taken for heat from the plasma to diffuse through the ceramic tube to be approximately 70 μs, much longer than the duration of the experiment. The probe laser had a power of 100 mW, a wavelength of 532 nm (different from that of the drive beams on the PVDF foils) and was focused with a 1 m lens to a focal spot of $\approx$ 0.5 mm. The polarisation of the probe beam was rotated using a half-wave plate to ensure it was at 45° to the optical axis of the beam-splitter before it passed through the crystal.

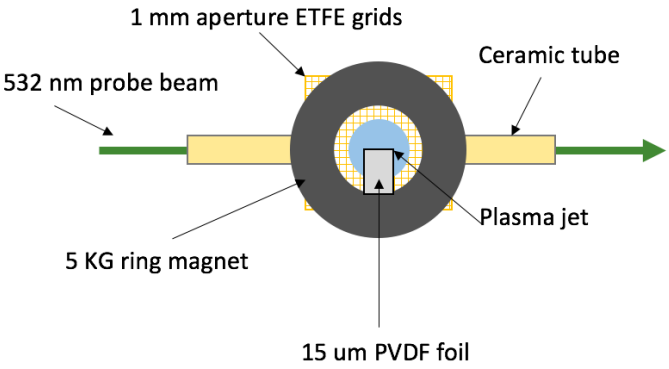

(a)

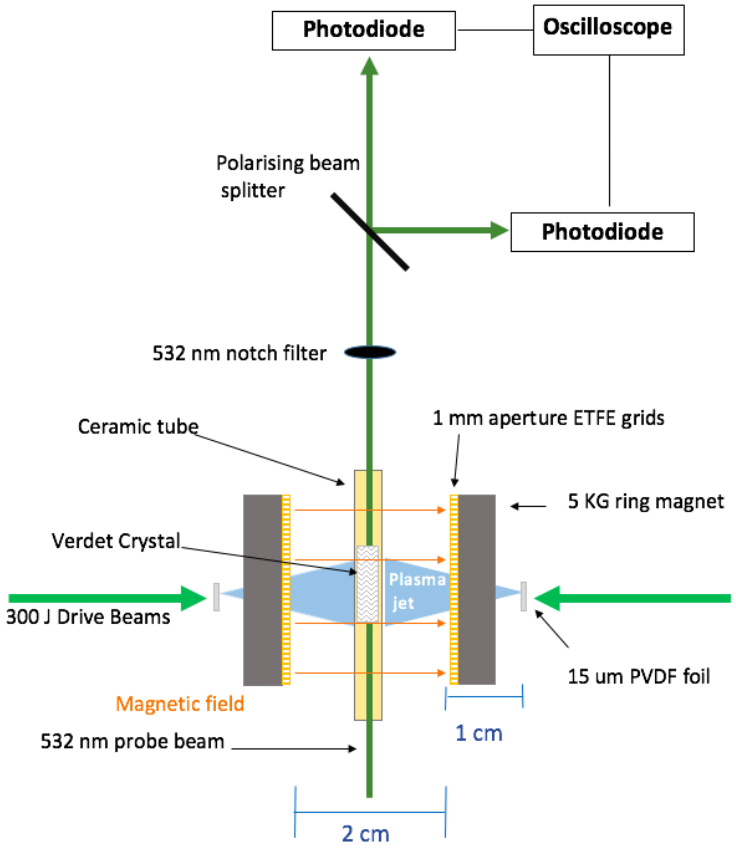

(b)

Figure 5.8: (a) View of the target from the direction of incoming drive beams showing the ceramic tube, containing the Verdet crystal.(b) Top-down view of target and magneto-optic probe setup. Once the jets have passed through the gird they collide with each other around the probe. The probe beam passes through the verdet crystal in the centre of the two jets before entering the detection system. Reproduced from [8].(Not to scale)

A optical line filter with a FWHM $\approx$ 1 nm was used to block any stray light from the target before the probe beam was divided by a 50/50 polarising beam splitter; each polarisation was then detected separately having been focused onto a 2 GHz (DET0.25A Thorlabs) photo-diode connected to a 1 GHz Lecroy oscilloscope.

The magnetic induction probe was placed with the coil between the magnets as shown in Figure 5.8. The coil was wrapped around a vespel core and housed in an glass housing. The b-dot was then connected to a differential amplifier to protect against electric fields which was then connected to a 1 GHz Lecroy oscilloscope. The impedance of the oscilloscope, differential amplifier an probe were matched to 50 ohms to prevent ringing. The two probes could not be placed in the plasma at the same time.

5.6 Results

5.6.1 Spectroscopy

The spectroscopy diagnostic was used to find the electron temperature and ion density in order to calculate the plasma sound speed and the turbulent velocity, both of which were needed to calculate the Mach number. At the conditions achieved in this experiment the line ratios of the emission spectra are independent of electron density for optically thin plasmas as the collisional deexcitation from the atomic levels dominates over spontaneous radiative decay [38, 145]. This occurs when the electron density $n_e < 1.7 \times 10^{14} T_e^{1/2} (\Delta E)^3$ cm^{-3}, where T_e is the electron temperature (in electronvolts) and ΔE is the transition energy (in electronvolts).

The analysis focused on the most intense spectral line in the optical region, the CII line at 426.7 nm and the two neighbouring FII lines at 426.8 nm and 429.9 nm. The spatially resolved spectroscopy data, an example of which is shown at the top of

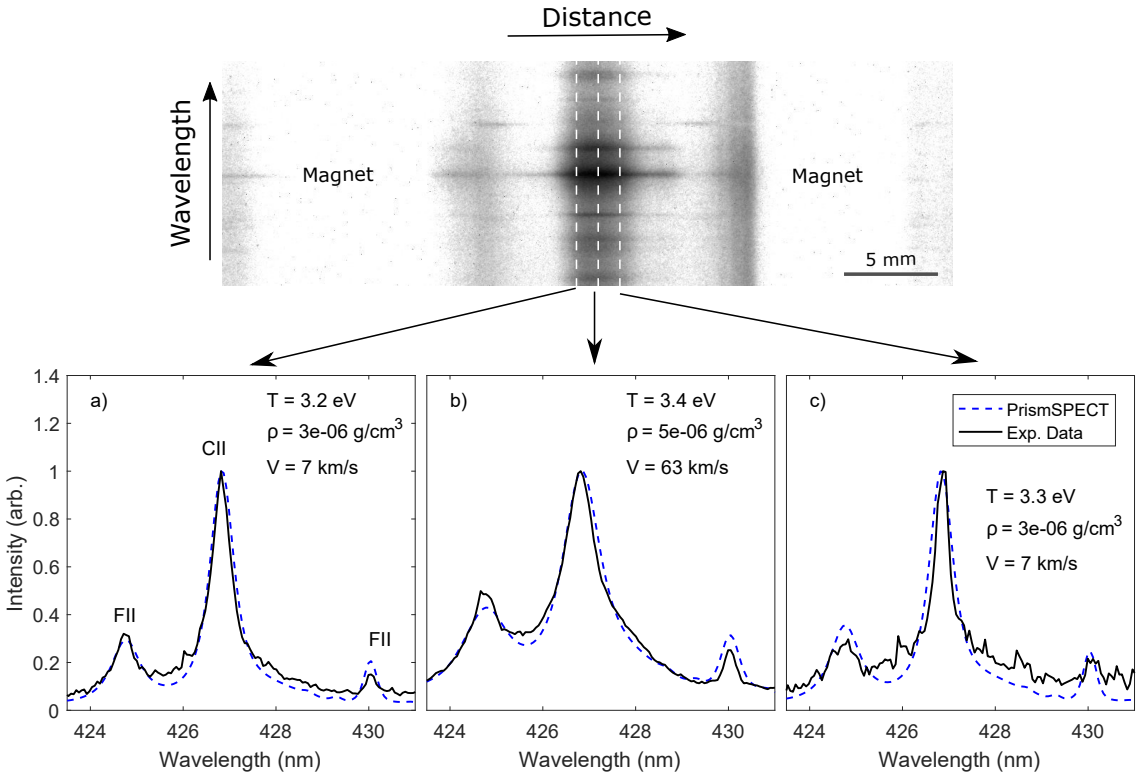

Figure 5.9: The spatial variation of the emission spectra taken 600 ns after the collision of the two supersonic jets. The raw data image shows the two permanent magnets, one on each side of the image. The jets can be seen colliding in the centre of the image. The three dotted lines show the slice along which the emission spectra shown were take. The data (black line) clearly broadens in the centre of the plasma. Simulated spectra were fitted to each spectra (blue lines). An increase in both density and turbulent velocity were seen in the centre of the interaction region. The turbulent velocity increases from $\sim$ 10 kms^{-1} at the edges of the plasma to $\sim$ 60 kms^{-1} in the centre. Reproduced from [11].

Figure 5.9, was sliced spatially into 2 mm strips before being analysed in order to retain spatial information. The spectroscopy data presented in this subsection was analysed using PrismSPECT [80]. The model includes Doppler, natural and Stark broadening. PrismSPECT was discussed in detail in Section 2.3.2. PrismSPECT was used to create 221 spectra over a range of temperatures (2.8 eV to 4 eV) and densities (0.05 $\times 10^{-5}$ gcm^{-3} to 1 $\times 10^{-5}$ gcm^{-3}). The simulated spectra were then imported into MATLAB where the turbulent broadening was added, as a convolution of the spectra with a Gaussian, for turbulent velocities ranging from 0 kms^{-1} to 200 kms^{-1}.

The broadening due to the instrument function of the spectrometer was also included as a convolution with a Gaussian, the magnitude of each of the two broadening mechanisms being added in quadrature. The simulated spectra were then fitted to the sliced data using the method of least squares. Broadening mechanisms other than those accounted for in PrismSPECT and MATLAB are shown to be negligible in the theory Section 3.4, calculated using parameters from the experiment. Fits to three different axial positions at 600 ns are shown in Figure 5.9 a, clear broadening of the central peak is seen in Figure 5.9 b.

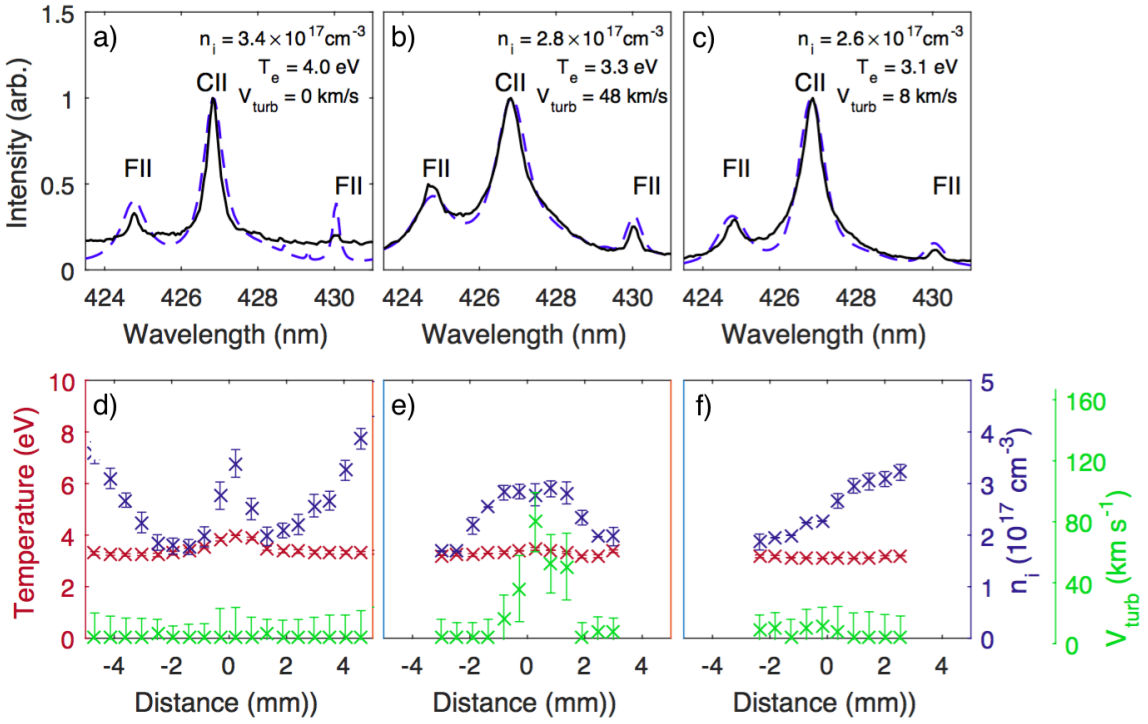

Figure 5.10: Both the fitted computer simulated spectra (blue line) overlaid with the data (black line) in the center of the collision region. a) 400 ns. b) 600 ns. c) 800 ns. The spatial variation of the plasma temperature, ion density and turbulent velocity found from the spectroscopic fits. d) 400 ns. e) 600 ns. f) 800 ns. Modified from [11].

The top row of Figure 5.10 shows the synthetic spectra fitted to the data in the centre of the collision region at 400 ns, 600 ns, and 800 ns after the drive beams fired. The broadening of the spectra clearly increases between 400 ns and 600 ns. The bottom row of Figure 5.10 show how the ion density, electron temperature and

turbulent velocity varied spatially between the magnets at each of the times after the collision. Figure 5.10 d shows the density increase as the two jets started to collide in the centre, around $d = 0$. At early times the plasma density is elevated closer to the foil targets. The electron temperature remained constant throughout the plasma, ~ 4 eV and the turbulent velocity was approximately ~ 0 kms^{-1}. In Figure 5.10 e the ion density near to the foils drops and the plasma becomes concentrated in the centre of the interaction region. The electron temperature remains constant across the interaction region, however there is a clear increases in turbulent velocity due to the collision of the jets, peaking around 60 kms^{-1}. At 800 ns, (Figure 5.10 f), the turbulent velocity has again decreased to zero. The temperature remains almost constant over 400 ns across the entire plasma. The error bars show in Figure 5.10 represent a 10 percent variation from the minimum of the sum of the residuals, found in the least mean squares fit. The PrismSPECT simulations calculate an ionisation state of Z $\sim$ 1.5 – 2.5. Post collision a turbulent Mach number is defined, M_{turb}, as the ratio between the three-dimensional turbulent velocity and the local sound speed, $M_{turb} = V_{jet}/c_s$. From the increase in Mach number ($M_{turb} \sim 1$ at 400 ns to $M_{turb} \sim 6$ at 600 ns) it was concluded that the interaction of the two plasma jets continuously drives turbulence for a duration much longer than the pulse duration of laser beams (~ 2 ns).

5.6.2 Interferometry

The interferometry diagnostic was used to find the electron density needed in the calculation of the ionisation state of the plasma, and thus the plasma sound speed. The electron density measured at different times throughout the experiment is shown in Figure 5.11. The several cuts across the images are the branch cuts, as discussed in Section 4.3, which indicate large variations in the electron density in small spatial regions, leading to broken fringes. The plasma continued to flow out from the grids

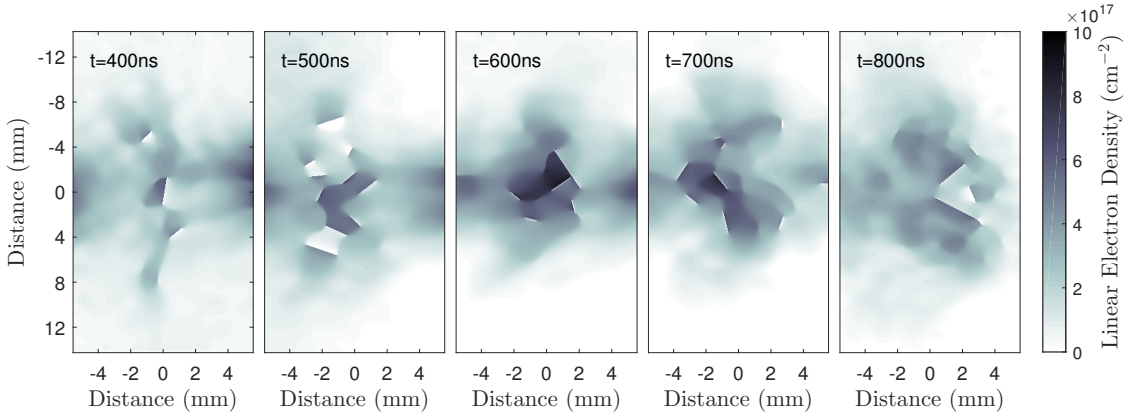

Figure 5.11: Time evolution of the plasma density between 400 and 800 ns. The peak density $\sim 6 \times 10^{17}$ cm^{-3} occurs after 600 ns. Reproduced from [11].

up to around 700 ns after the drive beams have fired. The plasma flow from the grids accrues in the centre of the collision region, with an electron density of $n_e \sim 2 \times 10^{17}$ cm^{-3} at around 400 ns and a peak value of $n_e \sim 6 \times 10^{17}$ cm^{-3} at 700 ns. Line integrated electron densities up to $\sim 6 \times 10^{17}$ cm^{-3} are measured over the course of the experiment. Combining this with the ion density measurement obtained from the optical spectroscopy an average ionisation state of $Z \sim 2$ was found. This is in agreement with the mean charge state calculated using the collisional radiative code PrismSPECT. The plasma sound speed was therefore found as $c_s = (ZT_e/m_i)^{1/2} \sim$ 10–12 km s^{-1} where m_i is the mean ion mass.

5.6.3 Schlieren Imaging

The Schlieren data were used to give an indication of the jet velocity needed to calculate the Mach number of the jet. The collision occurs after $\sim$ 300 ns, suggesting a maximum jet velocity of, $V_{jet} \sim 66 \pm 10$ kms^{-1}. Images of the colliding jets taken at 200 ns intervals are shown in Figure 5.12.

Plasma can be seen still flowing out from the grids 600 ns after the drive beams fired. The jets can be seen colliding in the centre, between the two magnets. After 400 ns a narrow strip of plasma can be seen in the centre of the interaction region. This

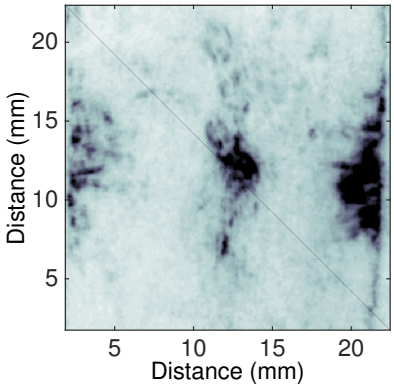

(a)

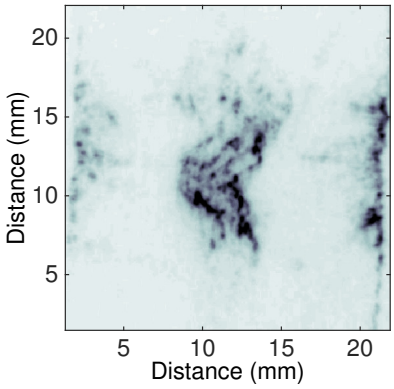

(b)

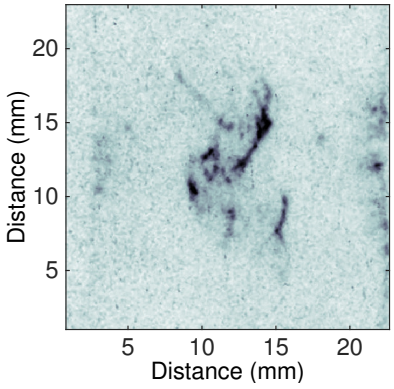

(c)

Figure 5.12: The collision of the two supersonic jets at times. a) 400 ns. b) 600 ns. c) 800 ns.

time coincides with the density increase seen in the emission spectroscopy, Figure 5.10 d. A larger turbulent plasma can be seen at 600 ns and 800 ns. At the later times they also showed the formation of the small shock like structures associated

with supersonic turbulence, see Figures 5.12 b and 5.12 c. The measurement of the jet velocity is used to calculate the jet Mach number $M_{jet} = V_{jet}/c_s \sim 6$ at ~ 600 ns.

5.6.4 The Magnetic Induction Probe

The magneto-optic probe provided a spatially integrated measurement of the magnetic field. The integration was performed on a scale over which the turbulence could not be considered isotropic. Therefore data taken by the magnetic-induction probe was used to find the exponent of the velocity power spectra. To examine the evolution of the spectra with changing Mach number the signal was analysed in 100 ns windows, the windows overlaid on the field are shown in Figure 5.13.

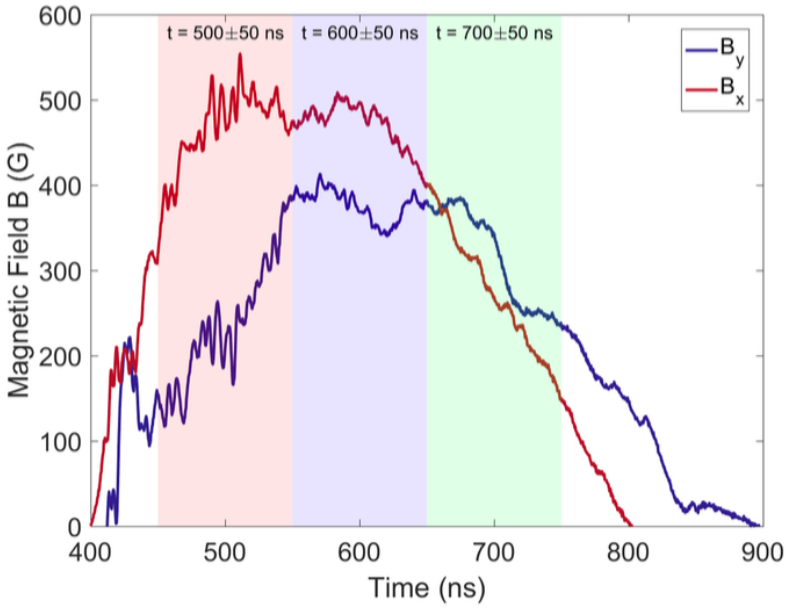

Figure 5.13: The magnetic fields B_x and B_y measured using the magnetic induction probe. Reproduced from [11].

Figure 5.13 shows the temporal evolution of the magnetic field over the course of the experiment. A sharp increase in the field is seen at 400 ns, corresponding to the time at which the plasma reached the probe. The magnetic field reached a maximum value of $B_y \sim 400$ G and $B_x \sim 500$ G. The magnetic field decreased again at ~ 700 ns. This agrees with both time scales found from the other diagnostics. To calculate

the magnetic power spectra a Hanning window was applied to the time dependent field measurement shown in Figure 5.13. If no windowing is applied the spectra will be dominated by the hard edges created by region selection. The windowed region was then discretely fast Fourier transformed in MATLAB. Due to the correlation between the individual points in the spectrum it is not possible to put error bars on the points themselves. Examples of the resulting power spectra are shown in Figure 5.14. The spectra were calculated for the 100 ns sections of the magnetic field as illustrated by the coloured regions shown in Figure 5.13. The red line at 50 MHz on each spectra shows the cut off below which the fit was performed. This was chosen after consideration of both the probe calibration (discussed in Section 4.4) and the region over which the spectra remains linear. The spectral scaling exponents are found from fitting a power law to the linear region of each spectra when the magnitude of $|B^2(\omega)|$ is plotted on a semilogarithmic plot. In both the x and y direction the spectra clearly steepen at later times, this is shown by the growth in the exponents. The spectral index grows from 5.0–5.4 at 500 $\pm$ 50 ns to 6.1–6.4 between 550 ns and 750 ns. The increase in exponent occurs alongside with an increase in turbulent Mach number from $M_{turb} < 1$ at 500 $\pm$ 50 ns to $M_{turb} > 1$ between 550 ns and 750 ns. The spectral exponents are also similar in the two cases, suggesting that the turbulence is isotropic as assumed in Section 4.2. Taking the fitted exponents of the temporal magnetic power spectra, ξ, the exponents of the velocity spectrum σ, were found using the relationship derived in Section 4.3

$$\xi = \frac{\alpha + 3}{\alpha - 1}, \tag{5.39}$$

$$\sigma = -(2\alpha + 1). \tag{5.40}$$

This leads to an E(k) $\sim k^{-1.67} - k^{-1.75}$ with $M_{turb} < 1$ and E(k) $\sim k^{-1.87} - k^{-1.91}$

with $M_{turb} \sim 6$. The values of E(k) at $M_{turb} < 1$ show a scaling similar to that found by Kolmogorov for subsonic turbulence. At $M_{turb} \sim 6$ the exponent grows in magnitude towards the result predicted by Burger [135, 138], E(k) $\sim k^{-2}$. The observed steepening of the velocity power spectrum can be attributed to the formation of shock structures, where the step-like velocity profile across the shock dominates the power-spectrum.

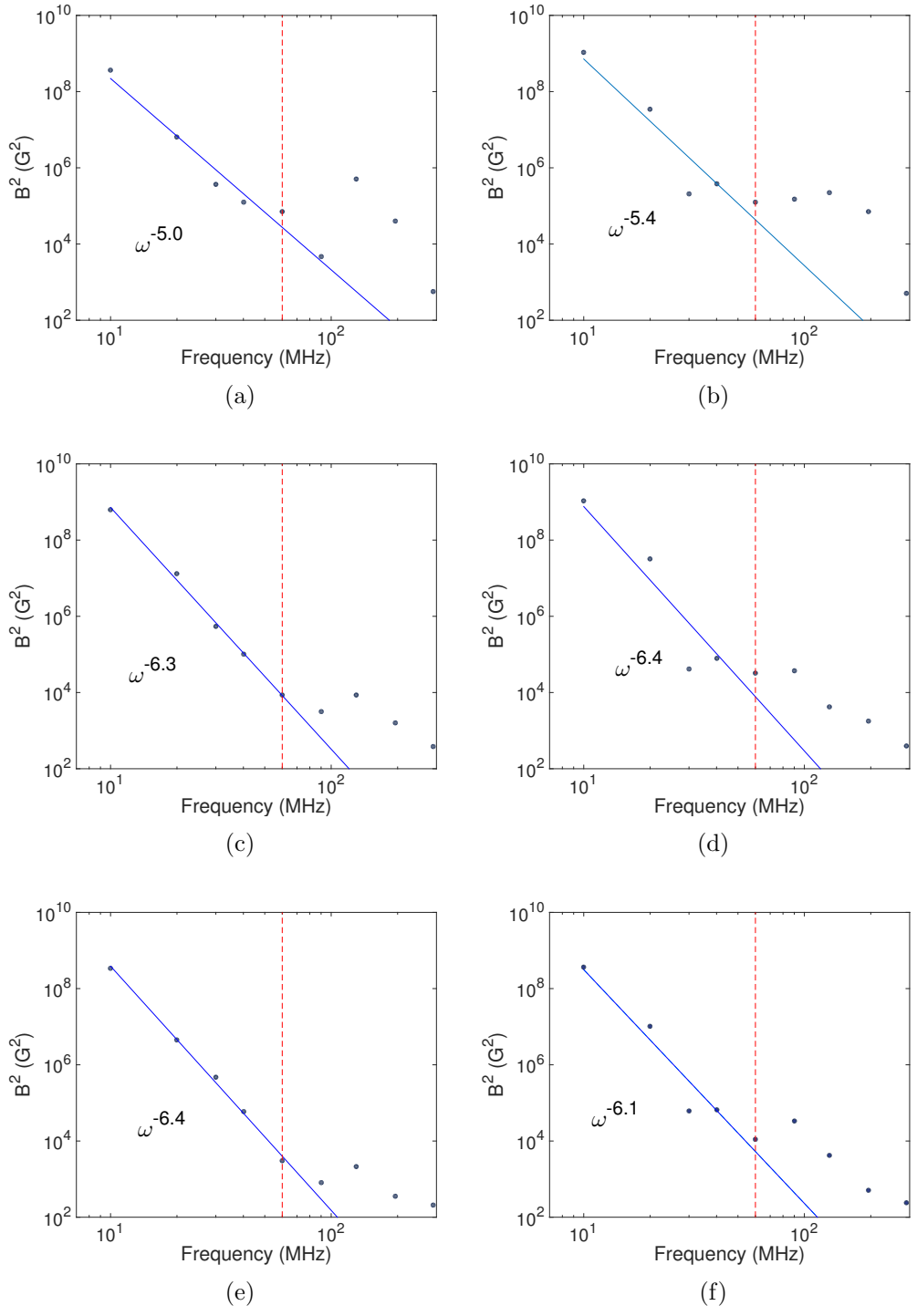

Figure 5.14: Temporal magnetic field spectra and the fitted power law perpendicular (B_y) and parallel to (B_x) the mean field. a) B_y at 500 $\pm$ 50 ns. b) B_x at 500 $\pm$ 50 ns. c) B_y at 600 $\pm$ 50 ns. d) B_x at 600 $\pm$ 50 ns. e) B_y at 700 $\pm$ 50 ns. f) B_x at 700 $\pm$ 50 ns.

5.6.5 The Magneto-Optic Probe

This section discusses the results obtained by the magneto-optic probe, including a comparison between the magneto-optic and magnet induction probe measurements.

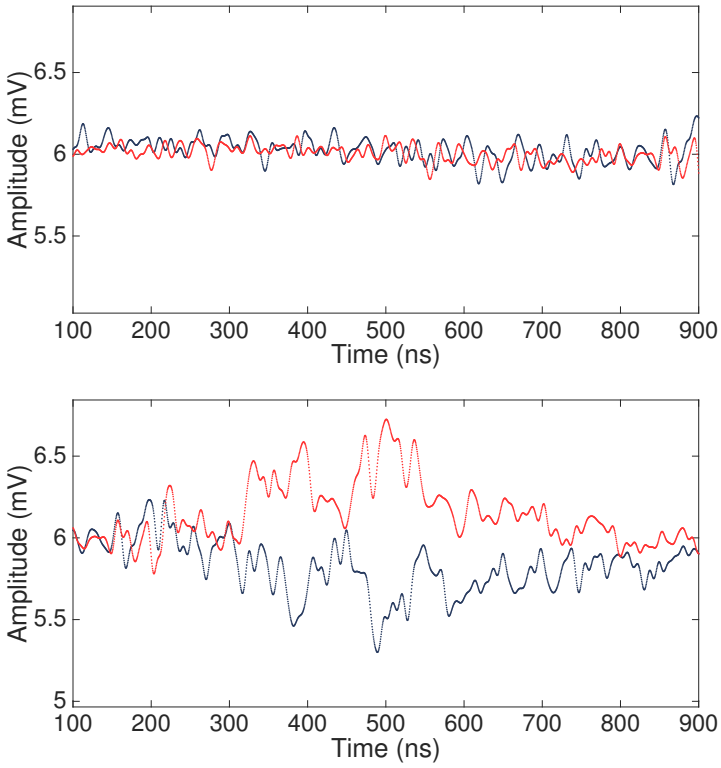

Figure 5.15: Measurements of the light intensity in both the horizontal (dark blue) and vertical (red) polarisations over 900 ns. a) no magnetised plasma around the probe (before the drive beams fired). b) In the presence of a single plasma jet. Reproduced from [8].

Figure 5.15 shows the intensity of the measured polarisations over a 800 ns period both before the plasma jet arrives at the probe (Figure 5.15 a) and in the presence of a single plasma jet (Figure 5.15 b). When no time varying magnetic field is present the intensity of each polarisation arriving at each diode equal. In the presence of the magnetised plasma the polarisation of the light is rotated through the Verdet crystal. The figure clearly shows the intensity of the two polarisations varying contrary to each other as the jet flows past. A low pass filter with a cut-off frequency of 10 MHz has been applied to the data shown in the figure. The magnetic field calculated from

these polarisations are shown in Figure 5.16. For the data shown the scale factor ϵ defined in Section 4.5 is found to be 0.98. The noise in the signal was caused by the low light intensity reaching the detector, this was due to the relatively poor intensity of the probe beam and the short duration of the experiment. Before the drive beams fired no time varying magnetic field should be measured by the probe. Therefore oscillations in the signal in Figure 5.15 a are noise. In this time range the maximum amplitude of the oscillations in the signal is ~ 30 G, suggesting an error in the measurements of around 10% of the peak field.

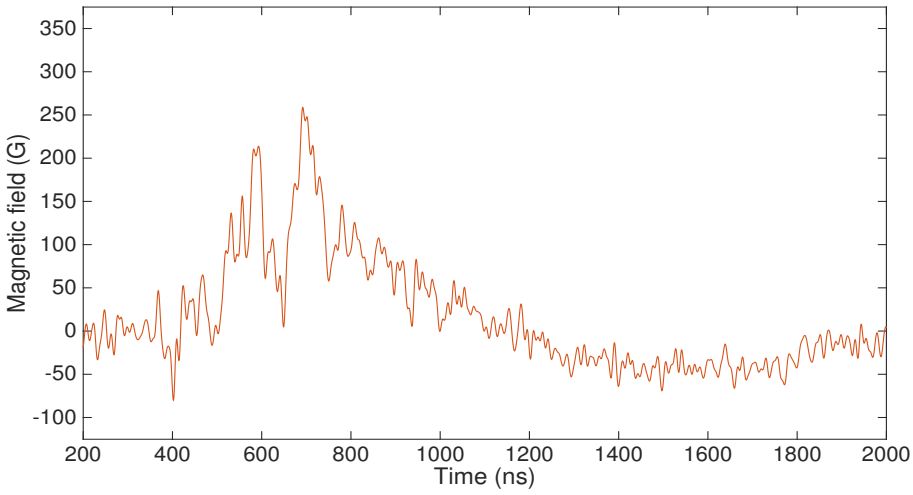

Figure 5.16: The magnetic field calculated from the data presented in Figure 5.15 b.

Figure 5.17 shows the measured magnetic field intensity (B_y) over the course of the experiment perpendicular to the externally applied field for both a single jet (a) and the collision of two turbulent jets (b). In both cases the field measured by the Verdet and the B-dot probes is similar, although the Verdet measurement shows larger-amplitude oscillations than the B-dot probe. Peak values of the magnetic fields are similar $B \approx 200$–300 G. However, it should be pointed out that the magnetic field measured by the Verdet crystal is averaged over the length of the crystal, while in the case of the B-dot the field measurement occurs locally in the collision centre. Whilst

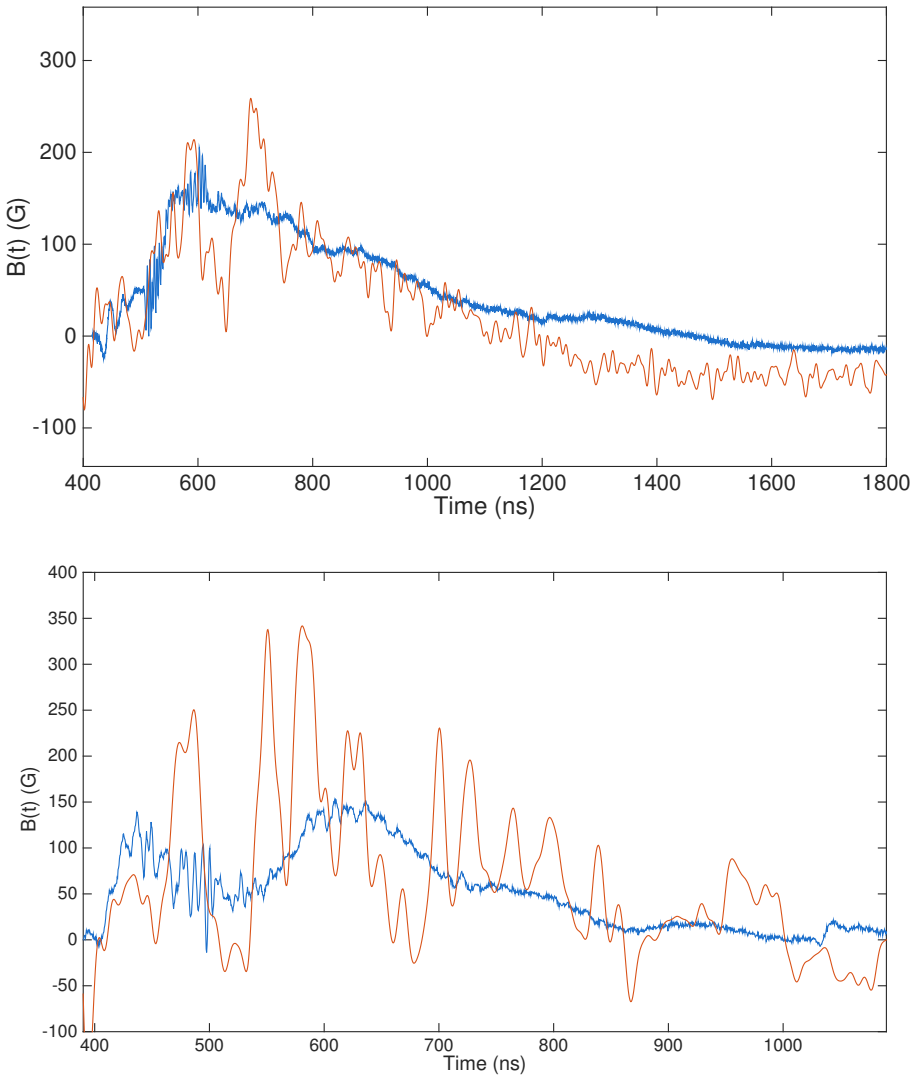

Figure 5.17: The blue line shows the magnetic field measured by the B-dot probe and the orange line shows the magnetic field measured by the magneto-optic probe. a) A measurement taken for a single jet that has not passed through a grid. b) A measurement taken for two colliding, turbulent jets as the plasma collides and stagnates around the probe. Reproduced from [8].

intuitively it would appear that the time-varying magnetic field should be smoother for a measurement integrated along a line of sight (i.e. the Verdet probe) than for the corresponding measurement made at a single point, this is not seen in the data. It is clear from the Schlieren data (see Figure 5.18) that the spatial structure of the plasma density varies significantly on the scale of the TGG crystal (10 mm). As the

field from the permanent magnets is at least partly advected along with the plasma flow, an anisotropic density distribution suggests there will also be a inhomogeneous magnetic field. The difference between the two probe measurements may be due to the inhomogeneity and anisotropy of the plasma.

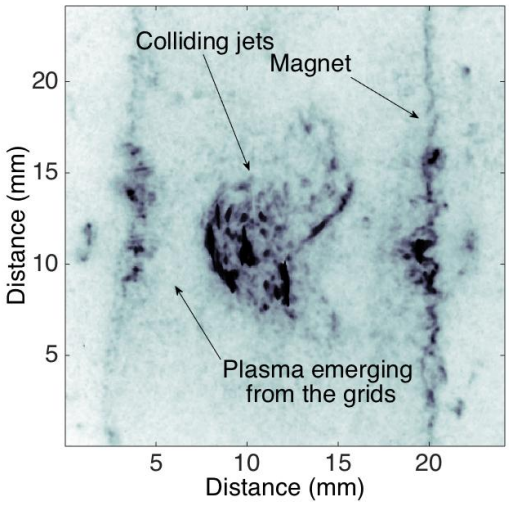

Figure 5.18: Schlieren images of the collision area. The magnets can be seen at the sides of the image. Plasma is seen emerging from the grids, bordering the magnets. The collision of the two turbulent jets appears in the centre of the image ($n_e \approx 10^{18}\,\mathrm{cm}^{-3}$). The turbulent plasma at 700 ns (no Verdet probe present). Modified from [8].

To calculate the magnetic power spectra a Hanning window was applied to the time dependent field measurements shown in Figures 5.17a and 5.17b. An example of the resulting spectrum is shown in Figure 5.19. The data was then binned. Median binning was chosen as it is less affected by noise and outliers, which may have an amplitude several orders of magnitude lower than neighboring points. Due to the correlation between the individual points in the spectrum it is not possible to put error bars on the points themselves. Figure 5.20 shows the magnetic power spectra, $|B(\omega)|^2$ against $\omega/2\pi$ for an 800 ns sections of the fields shown in Figure 5.17. The bandwidth of the B-dot probe, $\sim$ 40 MHz, is highlighted in the figure. The time

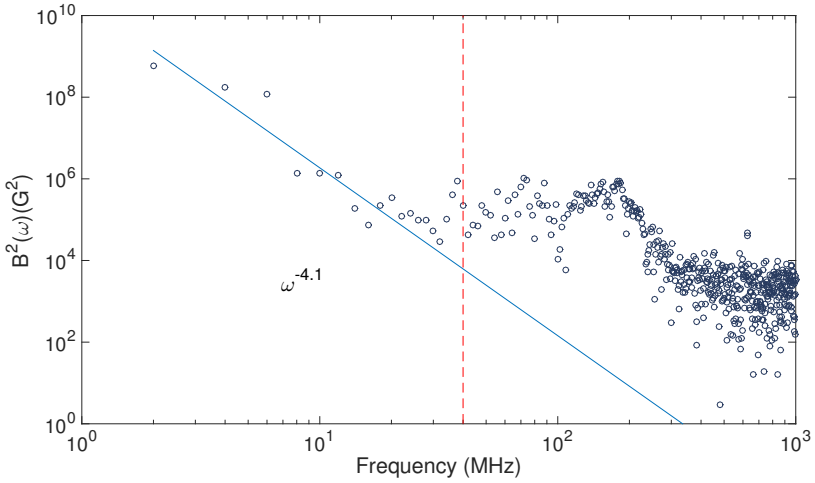

Figure 5.19: An example of a magnetic power spectrum, taken from the magnetic induction probe, before the binning. Reproduced from [8].

resolution of the magneto-optic probe in the experiment is limited by the (low) intensity of the probe laser light reaching the photo-diodes. Indeed, in Figure 5.20 we notice that the signal flattens between 60–100 MHz, indicating the start of the noise floor. The bandwidth of the magneto-optical probe was ~ 100 MHz, comparable to the B-dot. A power law has been fitted to the linear part of the spectra, giving $\omega^{-4.3}$ and $\omega^{-4.1}$ for the B-dot case, and $\omega^{-2.2}$ and $\omega^{-1.5}$ for the Verdet measurement.

To attempt to explain the difference consider the case of the single jet that has not passed through a grid, let us assume that at any given time t, the magnetic field at a point ℓ_0 is related to the magnetic field at a point ℓ along the axis of the TGG crystal by a power law relationship

$$B(t, \ell) \sim B(t, \ell_0)\ell^p, \tag{5.41}$$

where ℓ_0 can be assumed to be the center of the Verdet crystal, where the B-dot measurement is taken, and p is a constant to be determined. From Equations (4.2) and (5.41), we obtain

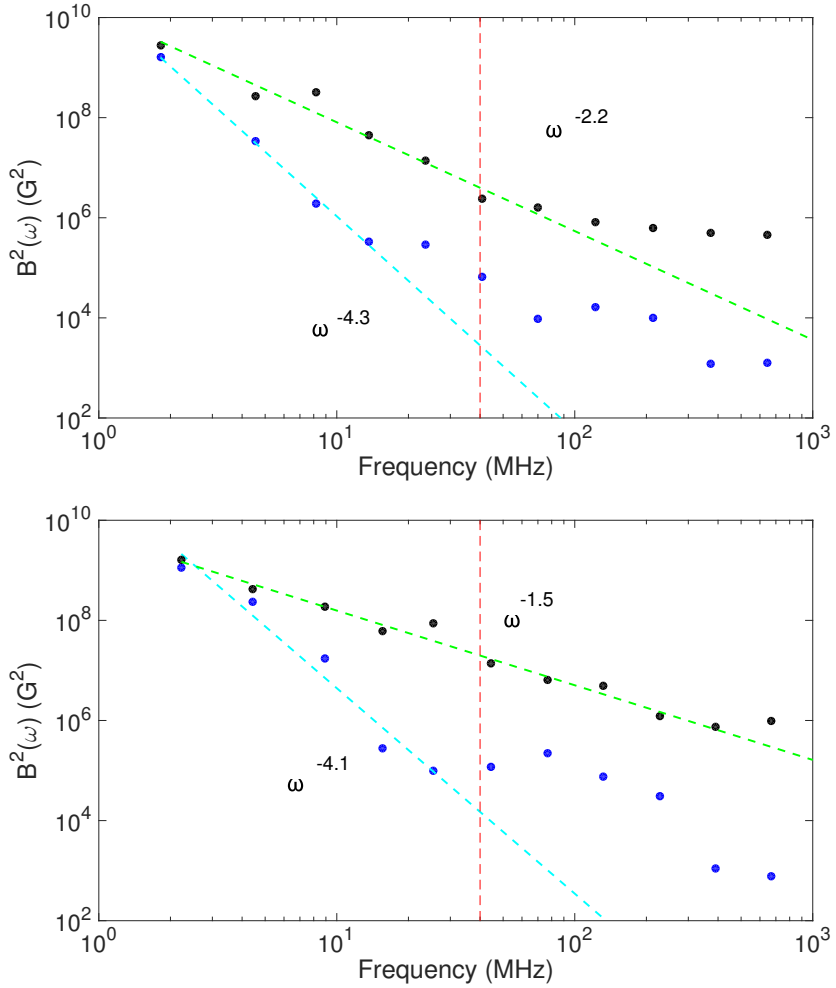

Figure 5.20: The magnetic power spectra as a function of the frequency for both the B-dot (black markers) and magneto-optic (blue markers) probes. Power laws are fitted to the measured spectra. The red line shows the bandwidth of the B-dot probe. a) Spectra for a single jet. b) Spectra for the collision of two turbulent jets. Reproduced from [8].

$$\langle B(t) \rangle \sim B(t, \ell_0) \ell^{p+1}. \tag{5.42}$$

Now, the power spectrum of the magnetic field measured at position ℓ_0 (as obtained from the B-dot data) is

$$M_0(\omega)\omega \sim |B(t, \ell_0)|^2 \sim \omega^{-\alpha+1}, \tag{5.43}$$

with $\alpha \sim 4.3$. The power spectrum of the magnetic field integrated along ℓ (as obtained from the Magneto-optic probe data) is

$$M(\omega)\omega \sim \langle B(t)\rangle^2 \sim |B(t,\ell_0)|^2 \ell^{2(p+1)} \sim \omega^{-\beta+1}. \tag{5.44}$$

As the mean flow velocity in the plasma is larger than the velocity fluctuations, according to Taylor's hypothesis, $\ell \sim t$. As a result of this proportionality relation, $\beta = \alpha + 2(p+1)$. Since the measurement gives $\beta \sim 2.2$, we deduce that $p \sim -2$. That is, the magnetic field has a real space distribution as

$$B(t,\ell) \sim \frac{B(t,\ell_0)}{\ell^2}, \tag{5.45}$$

indicating that the magnetic field rapidly decays away from the central region. This suggests that the combination of Verdet and B-dot measurements could retrieve information on both the temporal and spatial structure of the magnetic field in certain cases. The above discussion considered the case of a single jet that has not passed through a grid. For the collision between the two supersonic jets Taylor's hypothesis is invalid, this is shown from the similarity of the turbulent velocity of the colliding jets, $V_{turb} \sim 10 - 50$, and the jet velocity, $V_{jet} \sim 70$.

5.7 Conclusion

The plasma parameters measured during the experiment are presented in Table 5.1. These values were then used to find the additional plasma parameters shown in Table 5.2. (The equations used to calculate each additional quantity are also shown). The calculated values for the electron thermal collision time (0.5 ps) and the ion thermal collision time (24 ps) show that the fluid approximation is valid for the plasma as they

Quantity	Origin	Value
Average atomic weight (A)		10.66 a.m.u.
Ion density (n_i)	Spectroscopy	2 - 3×10^{17} cm^{-3}
Electron density (n_e)	Interferometry	5 - 7×10^{17} cm^{-3}
Average ion charge	$\frac{n_e}{n_i}$	2 - 2.5
Temperature ($T_e = T_i$)	Spectroscopy	3 - 4 eV
Static magnetic field (B_0)	Permanent Magnets	1.8 kG
Advected magnetic field (ΔB)	Induction Loop	500 G

Table 5.1: **Plasma Parameters.** Summary of the plasma parameters measured during the experiment. Values correspond to data taken 600 ns after the start of the drive laser.

are both much smaller than the plasma turnover time. The high fluid Reynolds number $R_e \sim 10^5$ demonstrates that the plasma is turbulent and the high turbulent Mach number ($M_{turb} \sim 6$) shows that the turbulence was indeed supersonic. The calculated values for both the thermal $\beta_{ther} \sim 37$, (the ratio of the thermal pressure to the magnetic pressure), and turbulent $\beta_{turb} \sim 150$, (the ratio of the turbulent pressure to the magnetic pressure), show that the advected externally applied magnetic field utilised as a tracer was indeed dynamically unimportant, as was assumed in the derivation outlined in Section 4.3. The derivation also assumed a low magnetic Reynolds number which is also justified, $R_m \sim 0.2$. At early times, when the turbulence was transonic ($M_{turb} \sim 1$) the energy spectra was found to be E(k) $\sim k^{-1.67} - k^{-1.75}$ similar to that predicted by Kolmogorov [31] for subsonic turbulence, i.e. E(k) $\sim k^{-5/3}$. The similarity of the power spectra at 600 and 700 ns suggests that the turbulence was

fully developed with and E(k) $\sim k^{-1.87} - k^{-1.91}$ and $M_{turb} \sim 6$. Similar to the result predicted by Burger [135, 138], E(k) $\sim k^{-2}$. The observed steepening of the velocity power spectrum can be attributed to the formation of shock structures, where the step-like velocity profile across the shock dominates the power-spectrum.

A radiative cooling rate of 0.5 eV/ns per ion was calculated in PrismSPECT and the measured electron temperature remained $\sim$ 4 eV over the course of the experiment, ($\sim$ 400 ns). As shown in previous experimental work [38, 146], the colliding turbulent plasmas exhibited an energy balance between radiative cooling and heating, the latter due to turbulent or shock dissipation. Such isothermal conditions are analogous to those found in Molecular clouds, albeit in the astrophysical case the balance is maintained between cosmic ray heating and cooling via emission from molecular lines [147]. Molecular clouds in the ISM have both large Reynolds numbers, $R_e \sim 10^8$ and turbulent Mach numbers $M_{turb} \leq 20$ [148]. The velocity power spectrum of the Perseus MC was found in the literature to be $E(k) \sim k^{-1.81 \pm 0.1}$ for $M_{turb} \sim 6$ [136] similar to the power spectrum measured during our experiment.

The high plasma β's also demonstrate that the experimental results should be compared to hydrodynamic simulations and observations, rather than magnetohydrodynamic simulations. Simulations of non-magnetised supersonic turbulence performed in three dimensions at $M_{turb} \sim 6$, found $E(k) \sim k^{-1.95}$ [133] and $M_{turb} \sim 10$, $E(k) \sim k^{-1.9} - k^{-2.0}$ [137], one dimensional simulations at $M_{turb} \sim 13$, found $E(k) \sim k^{-2}$ [135].

In this chapter we have demonstrated that the behaviour of supersonic compressible turbulence can be investigated experimentally through the collision of two laser-driven, high-velocity, turbulent, plasma jets. The velocity power spectra were ex-

tracted along with the thermodynamic properties of the plasma. Such experiments are able to provide information in addition to astrophysical observations as well as rigorous bench-marks for comparison to computational simulations. Future experiments could use high resolution, spatially resolved spectroscopy to find the spatial velocity power spectra directly. The density probability density distribution, another important statistical quantity [149], could also be measured with other diagnostics, e.g. Schlieren imaging or interferometry.

The comparison of the magnetic field measurements made by the magnetic induction and the magneto optic probe shows the magneto-optic probe can be used to make in situ-plasma measurements. The case of the measurements made for a single plasma jet are particularly compelling. The obvious benefits of the probe are its simple construction and it being unaffected by electrical noise. However we suggest the principal improvement over the magnetic-induction probe may be the probes ability to reach high frequency resolutions and not be affected by electronic noise, though it was not possible to demonstrate this clearly in the experiment. In the experiment, the frequency resolution, was limited by noise, primarily due to low light levels reaching the detector. In principle using a higher intensity laser, it should be possible to achieve a resolution limited by the photo diodes or oscilloscope, (i.e. a frequency resolution of 2 GHz). Care would need to taken to ensure that heating caused by the probe beam does not alter the transmission properties of the crystal. An improved spatial resolution can be achieved by using a smaller crystal however, the measurement will remain an integrated measurement along the crystal axis, thus the spatial resolutions achieved using B-dot probes are likely unobtainable.

Quantity	Origin	Value	
Thermal β_{ther}	$2\mu_0 \frac{n_i T + n_e T}{B_0^2}$	40	
Turbulent β_{turb}	$2\mu_0 \frac{\frac{1}{2} A n_i V_{\text{turb}}^2}{B_0^2}$	150	
Alfvén Velocity	$\frac{B_0}{\sqrt{\mu_0 A n_i}}$	2.5 km/s	
Sound speed (c_s)	$\sqrt{\frac{Z T_e + \frac{5}{3} T_i}{A}}$	10-12 km/s	
Debye Length (λ_D)	$\sqrt{\frac{\epsilon_0 / e^2}{\frac{n_e}{T_e} + \frac{Z^2 n_i}{T_i}}}$	10 nm	
Coulomb Logarithm ($\log\Delta$)	$\log \frac{\lambda_D}{\left(\frac{e^2}{4\pi\epsilon_0 T_e}\right)}$	3	
Ion thermal collision time (τ_i)	$(4\pi\epsilon)^2 \frac{3\sqrt{m_i} T_i^{\frac{3}{2}}}{4\sqrt{\pi}\log\Delta e^4 Z^4 n_i}$	25 ps	
Electron thermal collision time (τ_e)	$(4\pi\epsilon)^2 \frac{3\sqrt{m_e} T_e^{\frac{3}{2}}}{4\sqrt{\pi}\log\Delta e^4 Z^2 n_i}$	0.5 ps	
Viscosity (ν)	$\frac{0.96 n_i T_i \tau_i}{m_i n_i}$	5 cm^2/s	
Resistivity (μ)	$\frac{1}{\mu_0} \frac{0.44 m_e}{n_e e^2 \tau_e}$	4×10^5 cm^2/s	
Electron-ion equilibration time (τ_{ie}^{ϵ})	$\frac{(4\pi\epsilon_0)^2}{1.8} \frac{(m_e T_i + m_i T_e)^{\frac{3}{2}}}{(m_i m_e)^{\frac{1}{2}} Z^2 e^4 n_i \log\Delta}$	$\sim$20 ns	
Scale Length (L)		0.5 mm	200 μm
Velocity (V_{turb})		$< V_{jet}$ =66 km/s	10-50 km/s
Eddie turnover time	$\frac{L}{\text{V}_{\text{turb}}}$	15 ns	4 ns
Mach number (M_{turb})	$\text{V}_{\text{turb}}/c_s$	$\sim$6	$\sim$1-6
Fluid Reynolds number (Re)	$\text{V}_{\text{turb}} L/\nu$	$\sim 10^5$	$\sim 10^4$
Magnetic Reynolds number (Rm)	$\text{V}_{\text{turb}} L/\mu$	$\sim$1	$\sim$0.2

Table 5.2: **Plasma Parameters.** Summary of relevant plasma parameters. Values correspond to data taken 600 ns after the start of the drive laser. The 0.5 mm scale length corresponds to half the grid aperture, while 200 μm corresponds to regions spatially averaged by the optical spectroscopy line.

Chapter 6

Conclusion

6.1 Conclusions and Future Work

Chapters 2 and 3 discuss the theoretical background and experimental investigation into temperature and density measurements using emission spectroscopy inside of a capacitively coupled RF discharge. The discharge itself contained a bi-Maxwellian electron distribution supported by two different heating methods, ohmic heating and stochastic heating, whilst ionisation was principally due to high energy electrons accelerated across the oscillating sheaths. The results presented show that the temperature of the hot electron fraction within an RF discharge can be found by comparing emission spectra to synthetic spectra created using PrismSPECT. However this method cannot be used to accurately infer the electron density within the plasma. The success of the method appears to rely on the choice of the high neutral states of helium in order to avoid the effects of the metastable states within the discharge. This is supported by the large error in simulating the 501.6 nm emission line. To accurately predict the intensity of other emission lines would require a model which accounts correctly for particle diffusion and the ionisation mechanisms sustaining the discharge. This may require a model including both the ionisation due to γ electrons and the losses due to electron diffusion, of both the hot and cold electron population. Such models are starting to appear, with details of a full collisional-radiative model for a single temperature electron distribution being published in late 2017 [61]. The method presented could be attempted in different helium plasma sources, including helicons with only a single electron temperature and thus a simpler distribution function, which may improve accuracy.

Whilst density and temperature measurements within the RF discharge could be made using a Langmuir probe the temporal and spatial resolution required in the experiment presented in Chapters 4 and 5 rendered the Langmuir probe unusable. A huge amount of information could however still be inferred from an optical emission

spectroscopy diagnostic. As in the RF plasma OES was used to find the temperature and density of the laser produced plasma. In this instance the emission lines were broadened by various mechanisms (i.e. Doppler broadening, electron impact broadening) providing more information about the plasma than could be inferred using only the line ratio technique. In effect the plasma temperature was again found using the ratio of the emission lines. The plasma density and turbulent velocity were then found from the broadening. The density measured using the spectroscopy could also be corroborated by the interferometry diagnostic. The magnetic fields in the supersonic turbulent plasma were measured using the magneto-optic and magnetic induction probes as the Zeeman broadening was smaller than the instrument function of the spectrometer.

Chapters 4 and 5 discuss the theoretical background and experimental investigation into the magneto-optic probe and supersonic turbulence. To the knowledge of the author, this was the first instance where a magneto-optic probe was used to perform in-situ plasma measurements. The integrated field measurement for the single jet demonstrated excellent agreement for measurements made using both the magnetic-induction and magneto-optic probe. However, due to the nature of the supersonic turbulent plasma, direct comparisons for the measurements in the case of two colliding jets were not easily interpretable. In particular, the relationship between the magnetic power spectra of the path integrated and the point measurement of the magnetic field remains unclear. The diagnostic should be implemented again with a higher power probe laser in order to improve the frequency resolution and demonstrate clearly that it is an improvement over the widely used magnetic-induction probe. In the same experiment a supersonic plasma was successfully produced and diagnosed. The turbulent Mach number, found from spectroscopic broadening clearly showed that the turbulence was supersonic. Again, to the authors knowledge, this

was the first experiment performed on boundary free supersonic plasma turbulence. The scaling exponent of the spatial velocity power spectra was found through its relationship to the exponent of the temporal magnetic power spectra. The calculated value was similar to both astrophysical observations and theoretical predictions. Similar experiments attempted with improved diagnostics could be performed to measure the scaling exponent of the spatial velocity power spectra directly. A spectroscopy diagnostic with an improved resolution should be able to achieve this.

Hopefully the submitted papers, describing the investigation into optical emission spectroscopy in the radio frequency discharge and supersonic turbulence in laser produced plasma jets will both soon be published.

Appendix A

A.1 Ionization Balance in the γ Mode

This section closely follows the theory presented by Godyak and Khanneh published in [3]. If the loss of the thermal population of charged particles within the bulk plasma can be modelled by ambipolar diffusion the ionisation balance within the discharge can be written as

$$D_a \nabla^2 n + v_{iz} n(x) + G(x) = 0. \tag{A.1}$$

Where D_a is the ambipolar diffusion coefficient, $G(x)$ is a source term due to the ionisation caused by the secondary electrons and v_{iz} is the ionisation caused by thermal charged particles. In a symmetrically driven discharge where the electron mean free path for ionisation is much smaller than either the radius of the discharge r_0, or the distance between the electrodes $2d$, Equation (A.1)s can be solved leading to an expression for the variation in the axial plasma density within the discharge. If the origin ($x = 0$, $r = 0$) is chosen to be in the centre of the plasma, at the centre $n(0,0) = n_0$ and secondary electrons are injected at $x = \pm d$ the source term $G(x)$ is given by [3]

$$G(x) = \Gamma \frac{2 n_d v_1 \cosh(x/\lambda)}{\lambda \exp(d/\lambda)} \tag{A.2}$$

where n_d is the ion density at the plasma boundary, λ is the mean free path for the ionisation caused by a γ electron and Λ is a constant determined by the the number of electrons created in the sheath per ion reaching an electrode. Inserting Equation (A.2) in Equation (A.1) one finds

$$D_a \nabla^2 n + v_{iz} n(x) + \Gamma \frac{2 n_d v_1 \cosh(x/\lambda)}{\lambda \exp(d/\lambda)} = 0. \tag{A.3}$$

To solve Equation (A.3) using the separation of variables the plasma density $n(x, r)$ is given by

$$n(x, r) = n_0 Y(x) R(r), \tag{A.4}$$

upon this substitution, in cylindrical polar coordinates Equation, (A.4) becomes

$$D_a n_0 \left(Y \frac{1}{r} \frac{\partial}{\partial r} \left(r \frac{\partial R(r)}{\partial r} \right) + R(r) \frac{\partial^2 Y(x)}{\partial x^2} \right) \quad + \tag{A.5}$$

$$v_{iz}Y(x)R(r) + \Gamma\frac{2n_0Y(d)R(r)v_1\cosh(x/\lambda)}{\lambda\exp(d/\lambda)} = 0. \tag{A.6}$$

Dividing Equation (A.6) by $n_0Y(x)R(r)$ gives

$$-\frac{1}{rR(r)}\frac{\partial}{\partial r}\Big(r\frac{\partial R(r)}{\partial r}\Big) = \frac{1}{Y(x)}\frac{\partial^2 Y(x)}{\partial x^2} \quad + \tag{A.7}$$

$$\frac{v_{iz}}{D_a} + \Gamma\frac{2Y(d)v_1\cosh(x/\lambda)}{Y(x)\lambda\exp(d/\lambda)} = 0. \tag{A.8}$$

As the equation is now written in the form $f(x) = g(r)$ both $f(x)$ and $g(r)$ must be equal to a constant and therefore

$$-\frac{1}{rR(r)}\frac{\partial}{\partial r}\Big(r\frac{\partial R(r)}{\partial r}\Big) = \text{constant} = \mu^2. \tag{A.9}$$

Solutions to Equation (A.9) are given by Bessel's equations $R(r) = J_0(\mu r)$. The axial density is then described by

$$\frac{\partial^2 Y(x)}{\partial x^2} + (\frac{v_{iz}}{D_a} - \mu^2)Y(x) + \Gamma\beta\frac{2Y_1v_1\cosh(\beta x)}{D_a\exp(d\beta)} = 0, \tag{A.10}$$

where $Y_1 = Y(d)$ and $\beta = 1/\lambda$ in line with [3]. This equation must now be solved to find the normalised axial density distribution. The complementary solution to Equation (A.10) is given by

$$\frac{\partial^2 Y_c(x)}{\partial x^2} + (\frac{v_{iz}}{D_a} - \mu^2)Y_c(x) = 0. \tag{A.11}$$

This can be solved to give solutions to Y_c in the form

$$Y_c = A\cos\Big(\frac{mx}{d}\Big) + B\sin\Big(\frac{mx}{d}\Big), \tag{A.12}$$

where

$$\Big(\frac{m}{d}\Big)^2 = \frac{v_{iz}}{D_a} - \mu^2. \tag{A.13}$$

Searching for a particular solution and defining Y_p where

$$Y_p = \psi\Gamma\beta\frac{2Y_1v_1\cosh(\beta x)}{D_a\exp(\beta d)} = \psi\xi\cosh(\beta x), \tag{A.14}$$

leads to an equation for ψ given by

$$\beta^2\psi + \frac{m^2}{d^2}\psi + 1 = 0, \tag{A.15}$$

and therefore

$$\psi = -\frac{1}{\beta^2 + \frac{m^2}{d^2}}, \tag{A.16}$$

and

$$Y(x) = A\cos\left(\frac{mx}{d}\right) + B\sin\left(\frac{mx}{d}\right) + \psi\xi\cosh(\beta x). \tag{A.17}$$

Applying the boundary conditions $Y(\pm d) = Y_1$ and $Y(0) = 1$ one finds

$$Y = \cos\left(\frac{mx}{d}\right) - \Gamma\frac{2Y_1 v_1 \cosh(\beta x)}{\beta D_a \exp(\beta d)}, \tag{A.18}$$

in the limit where $\lambda << r_0, d$. Assuming that the flux of ions leaving the discharge at the plasma boundary

$$-\frac{d}{dx}(DY(d)) = Y_1 v_1, \tag{A.19}$$

leads to the conditions

$$\cos(m) = Y_1\left(1 + \frac{\Gamma v_1}{\beta D_a}\right), \tag{A.20}$$

and

$$m\tan(m) = \beta d\frac{1-\Gamma}{\Gamma}. \tag{A.21}$$

The plot in Section 2.1.3 is then produced from the equation

$$Y(x) = \cos\left(\frac{mx}{d}\right) - \frac{m\sin(m)\Gamma 2\cosh(\beta x)}{d\beta(\exp(\beta d) - \Gamma 2\sinh(\beta d))} \tag{A.22}$$

for a chosen value of Γ between $\Gamma = 0$ and a maximum value of $\Gamma = 1.31$.

A.2 Parameterized Ion Curves

The ion current collection models outlined in Chapter 2 are impractical for data analysis. Therefore in order to find and fit the ion current to the data presented in Chapter 3 parameterized curves were used. In a collision less plasma the ion current drawn by the probe I_i^{cless} can be expressed as [70]

$$I_i^{cless} = I_0 a(-X)^b \tag{A.23}$$

where I_0 is the ion current at the sheath edge, $X = q_e(V - V_p)/(k_b T_e)$ is the dimensionless probe potential (V_p) is the plasma potential and a, b are analytical parameters measured by Narasimhan and Steinbruchel [70], for a cylindrical probe

$$a_{cyl} = 1.18 - 0.00080\left(\frac{r_p}{\lambda_D}\right)^{1.35} = 1.146, \tag{A.24}$$

$$b_{cyl} = 0.0684 + \left(0.722 + 0.928\frac{r_p}{\lambda_D}\right)^{0.729} = 0.203, \tag{A.25}$$

for a cylindrical probe and

$$a_{sph} = 1.58 + 4.49\left(\frac{r_p}{\lambda_D}\right)^{-1.31} = 2.1, \tag{A.26}$$

$$b_{phs} = -2.95 + 3.61\left(\frac{r_p}{\lambda_D}\right)^{-0.0394} = 0.29. \tag{A.27}$$

for a spherical probe where $= 2 \times 10^{-4}$ m is the probe radius and $\lambda_D \approx 1.2 \times 10^{-5}$ m is the Debye length. A real cylindrical probe is modeled by the sum of the currents for both a cylindrical and a spherical probe. Where the inclusion of the spherical current is due to the end effect of the cylinder. The collision less current can be solved at a large ion current to find I_0. For a collisional model the ion current is then expressed as [67]

$$I_i^c = I_i^{cless}\gamma_1\gamma_2. \tag{A.28}$$

γ_1 is given by

$$\gamma_1 = \frac{I_{ABR}}{I_i^{cless}}, \tag{A.29}$$

where I_{ABR} is the current as found from ABR theory which is parameterized by [71, 150]

$$I_{ABR} = A\left(\frac{-X}{B}\right)^{C}, \tag{A.30}$$

where

$$A = \left(\left(\frac{r_p}{\lambda_D}\right) + 0.6\right)^{0.05} + 0.04 = 1.19, \tag{A.31}$$

$$B = 0.09\left(\exp\left(\frac{-\lambda_D}{r_p}\right) + 0.08\right) = 0.92, \tag{A.32}$$

$$C = \left(\left(\frac{r_p}{\lambda_D}\right) + 3.1\right)^{-0.6} = 0.17. \tag{A.33}$$

γ_2 is given by

$$\gamma_2 = \frac{3 - e^{\chi_i}}{2(1 + \chi_i)}, \tag{A.34}$$

where χ_i is the number of collisions a ion undergoes within the probe sheath defined as

$$\chi_i = \frac{r_s - r_p}{\lambda_i} \tag{A.35}$$

where r_s is the radius of the probe sheath and $\lambda_i \sim 0.01$ cm is the ion mean free path for collisions with the neutrals. The sheath radius is given by yet another analytical expression [71, 150]

$$r_s - r_p = \sqrt{(0.59 + 1.86(r_p/\lambda_D)^{0.47})(-X + 3.5) - 4} \tag{A.36}$$

These equations are used to fit Equation (A.28) to the ion current using n_e alone as the fitting parameter, the resultant fit is shown in Section 3.3.1.

Appendix B

B.1 Shocks

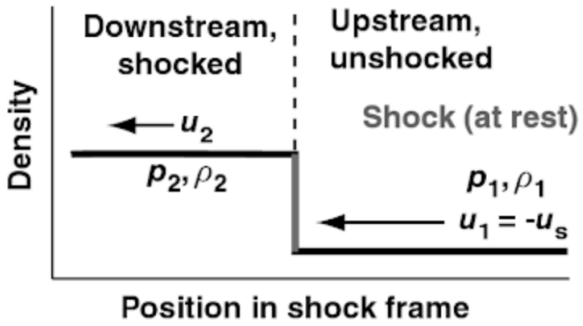

Figure B.1: A diagram showing the change in conditions across a shock front. Taken from [13].

In the previous section the plasma was described as a single fluid. This section discusses an important example of fluid like behaviour that is ubiquitous with plasma physics, the formation of shock waves. A shock refers to a sudden change in the plasma properties across a thin transition layer, approximately the width of the mean free collision path. In a nonmagnetised plasma, in the rest frame of the shock, the one dimensional steady state fluid equations are

$$\frac{\partial}{\partial x}(\rho u) = 0, \tag{B.1}$$

$$\frac{\partial}{\partial x}(\rho u^2 + p) = 0, \tag{B.2}$$

$$-\frac{\partial}{\partial x}\left(\rho u\left(\frac{u^2}{2} + \epsilon\right)u + pu\right) = 0. \tag{B.3}$$

As the transition layer is small it is neglected and the equations are integrated across the discontinuity giving

$$\rho_2 u_2 = \rho_1 u_1, \tag{B.4}$$

$$\rho_2 u_2^2 + p_2 = \rho_1 u_1^2 + p_1, \tag{B.5}$$

$$\rho_1 u_1\left(\frac{u_1^2}{2} + \epsilon_1\right)u_1 + p_1 u_1 = \rho_2 u_2\left(\frac{u_2^2}{2} + \epsilon_2\right)u_2 + p_2 u_2, \tag{B.6}$$

where the indicies represent whether the value is 'upstream' or 'down' stream of the

shock, for instance u_1 is the velocity in the pre-shock region. The above relationships are refered to as the Rankine-Hugoniot jump conditions [151, 152].Assuming the plasma can be modelled as an ideal gas with adiabatic index γ_{ad} the equation of state is $p/\rho_{ad} = \mathrm{C}$, where C is a constant. Equations (B.4) - (B.6) can then be solved to find the density jump across the shock

$$\frac{\rho_2}{\rho_1} = \frac{(\gamma_{ad}+1)M^2}{(\gamma_{ad}+1)+(\gamma_{ad}-1)(M^2-1)} \tag{B.7}$$

where $M = u_1/c_s$ is the sonic Mach number in the upstream flow. For Mach numbers $M >> 1$, Equation (B.8) becomes

$$\frac{\rho_2}{\rho_1} = \frac{\gamma_{ad}+1}{\gamma_{ad}-1}. \tag{B.8}$$

For a monatomic gas $\gamma_{ad} = \frac{5}{3}$, the density jump at a shock front is limited to $p_2/p_1 = 4$. Conversely the temperature jump across the shock is unbounded.

B.2 The Terbium Gallium Garnet (TTG) Crystal

The transmission properties of the TTG crystal can be affected by heating of the crystal. Here we show that the crystal is heated by neither the plasma nor the probe beam on the time scales over which the experiment is performed (~ 500 ns) in Chapter 5.

B.2.1 Absorption of the Probe Beam

The energy deposited in the TTG crystal by the probe beam E is given by

$$E = P_L \alpha_V t L = 375 \ \mu\text{J}, \tag{B.9}$$

where $P_L \sim 50mW$ is the power of the probe beam, $\alpha_V = 0.0015$ cm^{-3} is the absorption coefficient of the TTG crystal at 532 nm, $t \sim 5$ s is the duration over which the crystal is exposed to the probe beam and $L \sim 1$ cm is the length of the crystal. The specific heat capacity of the crystal is $C_p = 385$ Jkg^{-1}K^{-1} and the mass of the crystal $m_V = 0.055$ g, therefore the heat capacity of the TTG crystal is $C_V \sim 21600$ μJK^{-1}. This leads to a heating of the crystal due to the probe beam of

$$\Delta T \sim \frac{E}{C_V} \sim 0.02 \text{ K}, \tag{B.10}$$

which has a negligible effect on the transmission properties of the crystal.

B.2.2 Heating of the Crystal due to the Surrounding Plasma

As the crystal is surrounded by an Aliminia ceramic tube heat from the plasma must travel through the ceramic before it reaches the TGG crystal. The heat equation is given by

$$\frac{\partial T}{\partial t} = \alpha \nabla^2 T, \tag{B.11}$$

where T is the temperature of the ceramic and α is the thermal diffusivity. Equation (B.11) can be approximated as

$$\frac{\Delta T}{\Delta t} = \alpha \frac{T}{L^2} = \frac{\kappa T}{\rho C_p L^2} = 14500 \text{ Ks}^{-1}, \tag{B.12}$$

where $\kappa \sim 30$ $\mathrm{Wm^{-1}K^{-1}}$ is the thermal conductivity of Aliminia at 300 K, $\rho = 3920/\mathrm{kgm^{-3}}$ is the density of Aliminia, $C_p = 880$ $\mathrm{Jkg^{-1}K^{-1}}$ is the specific heat capacity of Aliminia and $L = 0.6$ mm is the thickness of the ceramic tube. Therefore to raise the temperature ΔT by 1 K takes a time of 70 μs, a time far longer then the duration of the experiment.

Bibliography

[1] J. D. Huba. *NRL PLASMA FORMULARY Supported by The Office of Naval Research*. Naval Research Laboratory, Washington, DC, 2013.

[2] Michael A. Lieberman and Allan J. Lichtenberg. *Principles of Plasma Discharges and Materials Processing: Second Edition*. Wiley, 2005.

[3] V. A. Godyak and A. S. Khanneh. Ion Bombardment Secondaty Electron Maintenance of Steady RF Discharge. *Plasma Science, IEEE Transactions on*, 14(2):112–123, 1986.

[4] F. F. Chen. Lecture Notes on Langmuir probe diagnostics. *Mini-Course on Plasma Diagnostics, IEEE-ICOPS Meeting*, page 42, 2003.

[5] R. F. Boivin, J. L. Kline, and E. E. Scime. Electron temperature measurement by a helium line intensity ratio method in helicon plasmas. *Physics of Plasmas*, 8(12):5303–5314, 2001.

[6] *https://impedans.com/langmuir-probe. Impedans Plasma Measurement Langmuir Probe Installation and User Guide.*

[7] M. J. Druyvesteyn. De invloed der energieverliezen bij elastische botsingen in de theorie der electronendiffusie. *Physica*, 10:61, 1930.

[8] M. Oliver, T. White, P. Maybe, M. Kühn-Kauffeldt, L. Döhl, R. Bingham, R. Clarke, P. Graham, R. Heathcote, M. Koenig, Y. Kuramitsu, D. Q. Lamb, J. Meinecke, T. Michel, F. Miniati, M. Notley, B. Reville, S. Sarkar, Y. Sakawa, A. A. Schekochihin, P. Tzeferacos, N. Woolsey, H. S. Park, and G. Gregori. Magneto-optic probe measurements in low density-supersonic jets. *Journal of Instrumentation*, 12(12), 2017.

[9] M. Hipp and P. Reiterer. *User manual for IDEA 1.7*. 2003.

[10] P. K. Panigrahi and K. Muralidhar. *Schlieren and Shadowgraph Methods in Heat and Mass Transfer*, 2:139, 2012.

[11] T. White, M. Oliver, P. Maybe, M. Kühn-Kauffeldt, L. Döhl, R. Bingham, R. Clarke, P. Graham, R. Heathcote, M. Koenig, Y. Kuramitsu, D. Q. Lamb, J. Meinecke, T. Michel, F. Miniati, M. Notley, B. Reville, S. Sarkar, Y. Sakawa, A. A. Schekochihin, P. Tzeferacos, N. Woolsey, H. S. Park, and G. Gregori. Supersonic Plasma Turbulence in the Laboratory. 2018 (Submitted).

[12] Princeton Instruments. *Operating instructions Acton Series SP-2750*.

[13] R P Drake. *High-Energy-Density Physics: Fundamentals, Inertial Fusion, and Experimental Astrophysics. Shock Wave and High Pressure Phenomena.* Springer 1 st edition, 2006.

[14] A. Siliotti and Z. Hawass. *Guide to the Pyramids of Egypt*. AUC Press, 1997.

[15] M. Carabatea. *Greek Mythology Gods And Heroes. Iliad. Odyssey*. Adam Editions, 1997.

[16] B. W. Carroll and D. A. Ostlie. *An Introduction to Modern Astrophysics*. Pearson, 2nd (international) edition, 2007.

[17] S-I. Akasofu. *Physics of magnetospheric substorms*. D. Reidel Pub. Co Dordrecht, Holland ; Boston, 1977.

[18] J.W. Chamberlain. *Physics of the Aurora and Airglow*. International geophysics series. Academic Press, 1961.

[19] V.A. Rakov and M.A. Uman. *Lightning: Physics and Effects*. Cambridge University Press, 2003.

[20] B. Zohuri. *Inertial Confinement Fusion Driven Thermonuclear Energy*. Springer International Publishing, 2017.

[21] M. Oliver, T. White, A. Dyson, P. Kozlowski, and G. Gregori. Electron temperature and density measurements using optical emission spectroscopy in a helium capacitively coupled radio frequency discharge. 2018 (In Preparation).

[22] F.F. Chen. *Introduction to Plasma Physics and Controlled Fusion*. Introduction to Plasma Physics and Controlled Fusion. Springer, 1984.

[23] H. Alfvén. Existence of Electromagnetic-Hydrodynamic Waves. *Nature*, (150):405406, 1942.

[24] Isaac Newton. *The mathematical principles of Natural philosophy*. 1713.

[25] H. Alfvén. Cosmical Electrodynamics. *American Journal of Physics*, 28(7):613–618, 1960.

[26] T. J. M. Boyd and J. J. Sanderson. *The physics of plasmas*. Cambridge University Press, 2003.

[27] D. Ryutov, R. P. Drake, J. Kane, E. Liang, B. A. Remington, and W. M. Wood-Vasey. Similarity criteria for the laboratory simulation of supernova hydrodynamics. *The Astrophysical Journal*, 518(2):821, 1999.

[28] D. D. Ryutov, B. A. Remington, H. F. Robey, and R. P. Drake. Magnetohydrodynamic scaling: From astrophysics to the laboratory. *Physics of Plasmas*, 8(5 II):1804–1816, 2001.

[29] P. Davidson. *Turbulence: An Introduction for Scientists and Engineers*. Oxford University Press, 1 st edition, 2015.

[30] O. Reynolds. An experimental investigation of the circumstances which determine whether the motion of water shall be direct or sinuous, and of the law of resistance in parallel channels. *Philosophical Transactions of the Royal Society of London*, 174:935–982, 1883.

[31] A. N. Kolmogorov. The local structure of turbulence in incompressible viscous fluid for very large Reynolds numbers. *Proceedings of the Royal Society of London. Series A-Mathematical and Physical Sciences*, 434(1890):9–13, 1991.

[32] J. M. Dawson. On the Production of Plasma by Giant Pulse Lasers. *Physics of Fluids*, 7(7):981, 1964.

[33] B. H. Ripin, E. A. McLean, C. K. Manka, C. Pawley, J. A. Stamper, T. A. Peyser, A. N. Mostovych, J. Grun, A. B. Hassam, and J. Huba. Large-Larmor-radius interchange instability. *Physical Review Letters*, 59(20):2299–2302, 1987.

[34] AR Bell, P Choi, AE Dangor, O Willi, DA Bassett, and CJ Hooker. Collisionless shock in a laser-produced ablating plasma. *Physical Review A*, 38(3):1363, 1988.

[35] JOSEPH E Borovsky, MORRIS B Pongratz, ROBERT A Roussel-Dupre, and T-H Tan. The laboratory simulation of unmagnetized supernova remnants absence of a blast wave. *The Astrophysical Journal*, 280:802–808, 1984.

[36] H. Takabe. Inertial confinement fusion and supernova explosion. *Purazuma, Kaku Yugo Gakkai-Shi*, 69(11):1285–1300, 1993.

[37] B. A. Remington, R. P. Drake, H. Takabe, and D. Arnett. A review of astrophysics experiments on intense lasers. *Physics of Plasmas*, 7(5):1641–1652, 2000.

[38] J. Meinecke, P. Tzeferacos, A. Bell, R. Bingham, R. Clarke, E. Churazov, R. Crowston, H. Doyle, R. P. Drake, R. Heathcote, M. Koenig, Y. Kuramitsu, C. Kuranz, D. Lee, M. MacDonald, C. Murphy, M. Notley, H-S. Park, A. Pelka, A. Ravasio, B. Reville, Y. Sakawa, W. Wan, N. Woolsey, R. Yurchak, F. Miniati, A. Schekochihin, D. Lamb, and G. Gregori. Developed turbulence and nonlinear amplification of magnetic fields in laboratory and astrophysical plasmas. *Proceedings of the National Academy of Sciences*, 112(27):8211–8215, 2015.

[39] J. Meinecke, H. W. Doyle, F. Miniati, A. R. Bell1, R. Bingham, R. Crowston, R. P. Drake, M. Fatenejad, M. Koenig, Y. Kuramitsu, C. C. Kuranz, D. Q. Lamb, D. Lee, M. J. MacDonald, C. D. Murphy, H-S. Park, A. Pelka, A. Ravasio, Y. Sakawa, A. A. Schekochihin, A. Scopatz, P. Tzeferacos, W. C. Wan, N. C. Woolsey, R. Yurchak, B. Reville, and G. Gregori. Turbulent amplification of magnetic fields in laboratory laser-produced shock waves. *Nature Physics*, 10(June):2–6, 2014.

[40] D. Papamoschou. Evidence of shocklets in a counterflow supersonic shear layer. *Physics of Fluids*, 7(2):233, 1995.

[41] T. H. Maiman, R. H. Hoskins, I. J. D'Haenens, C. K. Asawa, and V. Evtuhov. Stimulated optical emission in fluorescent solids. II. Spectroscopy and stimulated emission in ruby. *Physical Review*, 123(4):1151–1157, 1961.

[42] H. W. Mocker and R. J. Collins. Mode competition and self-locking effects in a q-switched ruby laser. *Applied Physics Letters*, 7(10):270–273, 1965.

[43] F. J. McClung and R. W. Hellwarth. Giant optical pulsations from ruby. *Journal of Applied Physics*, 33(3):828–829, 1962.

[44] Donna Strickland and Gerard Mourou. Compression of amplified chirped optical pulses. *Optics Communications*, 55(6):447–449, 1985.

[45] M. Pessot, P. Maine, and G. Mourou. 1000 times expansion/compression of optical pulses for chirped pulse amplification. *Optics Communications*, 62(6):419–421, 1987.

[46] C. E. Max. *Theory of the coronal plasma in laser fusion targets.* Lawrence Livermore Laboratory, University of California, 1981.

[47] William L Kruer. The physics of laser plasma interactions. 1988.

[48] Yaakov Shima and Haim Yatom. Inverse bremsstrahlung energy absorption rate. *Physical Review A*, 12:21062117, 1975.

[49] W. M. Manheimer, D. G. Colombant, and B. H. Ripin. Efficient light absorption by ion-acoustic fluctuations in laser-produced plasmas. *Physical Review Letters*, 38(20):1135–1138, 1977.

[50] D. R. Gray and J. D. Kilkenny. The measurement of ion acoustic turbulence and reduced thermal conductivity caused by a large temperature gradient in a laser heated plasma. *Plasma Physics*, 22(2):81, 1980.

[51] W. M. Manheimer and D. G. Colombant. Light absorption by ion acoustic turbulence in laserproduced plasmas. *Physics of Fluids*, 21(1978):1818, 1978.

[52] M. A. Lieberman, Allan J. Lichtenberg, and S.E. Savas. Model of magnetically enhanced, capacitive rf discharges. *IEEE Transactions on Plasma Science*, 19(2):189–196, 1991.

[53] Y. P. Raizer. Gas discharge physics. 1991.

[54] D. B. Graves and K. F. Jensen. A continuum model of dc and rf discharges. *IEEE Transactions on plasma science*, 14(2):78–91, 1986.

[55] R. F. Boivin, S. D. Loch, C. P. Ballance, D. Branscomb, and M. S. Pindzola. Line ratio diagnostics in helium and helium seeded argon plasmas. *Plasma Sources Science and Technology*, 16(3):470–479, 2007.

[56] F. F. Chen. Saturation ion currents to langmuir probes. *Journal of Applied Physics*, 36(3):675–678, 1965.

[57] F. F. Chen, J. D. Evans, and W. Zawalski. Low Temperature Plasma Technology Laboratory probes. 2012.

[58] V. Godyak, R. Piejak, and B Alexandrovich. Measurements of electron energy distribution in low-pressure R F discharges. *Plasma Sources Science and Technology*, 1:36–58, 1992.

[59] Z. Chen, V. M. Donnelly, D. J. Economou, L. Chen, M. Funk, and R. Sundararajan. Measurement of electron temperatures and electron energy distribution functions in dual frequency capacitively coupled CF4/O2 plasmas using trace rare gases optical emission spectroscopy. *J. Vac. Sci. Technol. A*, 27(5):1159–1165, 2009.

[60] V. A. Godyak, R. B. Piejak, and B. M. Alexandrovich. Evolution of the Electron-Energy-Distribution Function during rf Discharge Transition to the High-Voltage Mode. *Physical Review*, 68(1):1–4, 1992.

[61] J. Claustre, C. Boukandou-Mombo, J. Margot, J. P. Matte, and F. Vidal. An advanced time-dependent collisional-radiative model of helium plasma discharges. *Plasma Sources Science and Technology*, 26(10), 2017.

[62] J. J. Shi and M. G. Kong. Mechanisms of the α and γ modes in radio-frequency atmospheric glow discharges. *Journal of Applied Physics*, 97(2):1–7, 2005.

[63] V. Lisovskiy, J. P. Booth, K. Landry, D. Douai, V. Cassagne, and V. Yegorenkov. Modes and the alpha-gamma transition in rf capacitive discharges in N 2O at different rf frequencies. *Physics of Plasmas*, 13(10):1–8, 2006.

[64] F. A. Haas and N. St J. Braithwaite. Simple analysis of a capacitive discharge with a bi-Maxwellian electron distribution. *Plasma Sources Science and Technology*, 9(1):77–81, 2000.

[65] V. A. Godyak. Nonequilibrium EEDF in gas discharge plasmas. *IEEE Transactions on Plasma Science*, 34(3 PART 2):755–766, 2006.

[66] J. Wilhelm and W. Kind. On the theory of a cathode glow of a low pressure discharge. *Beitr. Plasmaphys*, 5:395–403, 1965.

[67] Z. Zakrzewski and T. Kopiczynski. Effect of collisions on positive ion collection by a cylindrical Langmuir probe. *Plasma Physics*, 16(12):1195–1198, 1974.

[68] R. L. F. Boyd. The Collection of Positive Ions by a Probe in an Electrical Discharge. *Proceedings of the Royal Society A: Mathematical, Physical and Engineering Sciences*, 201(1066):329–347, 1950.

[69] I. B. Bernstein and I. N. Rabinowitz. Theory of Electrostatic Probes in a Low-Density Plasma. *Physics of Fluids*, 2(2):112, 1959.

[70] G. Narasimhan and Ch. Steinbrüchel. Analysis of Langmuir probe data: Analytical parametrization, and the importance of the end effect. *Journal of Vacuum Science and Technology A: Vacuum, Surfaces, and Films*, 19(1):376, 2001.

[71] S. Klagge and M. Tichý. A contribution to the assessment of the influence of collisions on the measurements with Langmuir probes in the thick sheath working regime. *Czechoslovak Journal of Physics*, 35(9):988–1006, 1985.

[72] J. G. Laframboise. Theory of spherical and cylindrical langmuir probes in a collisionless, maxwellian plasma at rest. *Aerospace Engineering reports*, (100):1–216, 1966.

[73] S. Sasaki, S. Takamura, S. Watanabe, S. Masuzaki, T. Kato, and K. Kadota. Helium I line intensity ratios in a plasma for the diagnostics of fusion edge plasmas. *Review of Scientific Instruments*, 67(10):3521–3529, 1996.

[74] Wolfgang L Wiese, Melvin William Smith, and BM Glennon. Atomic transition probabilities. volume i. hydrogen through neon. Technical report, National Standard Reference Data System, 1966.

[75] U. Fantz. Basics of plasma spectroscopy. *Plasma Sources Science and Technology*, 15(4):S137—-S147, 2006.

[76] R Mewe. Note on the singlet and triplet population in helium. *British Journal of Applied Physics*, 17(9):1239, 1966.

[77] Hans-Joachim Kunze. *Introduction to plasma spectroscopy*, volume 56. Springer Science & Business Media, 2009.

[78] C. P. Ballance, D. C. Griffin, S. D. Loch, R. F. Boivin, and M. S. Pindzola. Collisional-radiative calculations of He line emission in low-temperature plasmas. *Physical Review A - Atomic, Molecular, and Optical Physics*, 74(1):1–8, 2006.

[79] Takashi Fujimoto and Takako Kato. Collisional-radiative model for helium-like ions: Application to intermediate-density plasmas. *Physical Review A*, 30(1):379, 1984.

[80] J. J. MacFarlane, I. E. Golovkin, P. R. Woodruff, D. R. Welch, B. V. Oliver, T. A. Mehlhorn, and R. B. Campbell. Simulation of the ionization dynamics of aluminum irradiated by intense short-pulse lasers. *Proceedings of Inertial Fusion and Science Applications (American Nuclear Society, La Grange Park, IL)*, pages 1–4, 2003.

[81] S. P. Cunningham. Conference on Thermonuclear Reactors, US Atomic Energy Commission Report No. 279. *Conference on Thermonuclear Reactors, US Atomic Energy Commission Report No. 279*, 80(11):1–8, 1995.

[82] R. Flohr, H. Schirmer, and A. Piel. Investigation of an Enhanced Glow Structure in a Low Pressure rf Discharge in Helium. *Contributions to Plasma Physics*, 33(3):153–168, 1993.

[83] R. W. Lee. The How To for FLY. (November), 1995.

[84] Z. Navrátil, P. Dvořák, O. Brzobohatỳ, and D. Trunec. Determination of electron density and temperature in a capacitively coupled rf discharge in neon by oes complemented with a cr model. *Journal of Physics D: Applied Physics*, 43(50):505203, 2010.

[85] V. A. Godyak and V. I. Demidov. Probe measurements of electron-energy distributions in plasmas: What can we measure and how can we achieve reliable results? *Journal of Physics D: Applied Physics*, 44(23), 2011.

[86] T. S. V. K. Popov, M. Dimitrova, M. A. Pedrosa, D. López-Bruna, J. Horacek, J. Kovačič, R. Dejarnac, J. Stöckel, M. Aftanas, P. Böhm, P. Bílková, C. Hidalgo, and R. Panek. Bi-Maxwellian electron energy distribution function in the vicinity of the last closed flux surface in fusion plasma. *Plasma Physics and Controlled Fusion*, 57(11):13, 2015.

[87] H. Morkoç, S. Strite, G. B. Gao, M. E. Lin, B. Sverdlov, and M. Burns. Large-band-gap SiC, III-V nitride, and II-VI ZnSe-based semiconductor device technologies. *Journal of Applied Physics*, 76(3):1363–1398, 1994.

[88] R. Franklin and C. Diaz. Research status of the variable specific impulse magnetoplasma rocket. *Fusion Technology*, 35(1T):87–93, 1999.

[89] R. Franklin and C. Diaz. The vasimir rocket. *Scientific American*, 283(5):90–97, 2000.

[90] Y. Andrew, S. J. Davies, D. Elder, L. D. Horton, G. F. Matthews, A. Meigs, P. D. Morgan, M. O'Mullane, M. Stamp, R. Prentice, and P. C. Stangeby. Interpretative modelling of JET's thermal helium diagnostic. *Journal of Nuclear Materials*, 266:1234–1239, 1999.

[91] G. Franz. *Low pressure plasmas and microstructuring technology*. Springer Science & Business Media, 2009.

[92] User Manual. AE {®} CESAR {®} 1310 Generator. (November), 2008.

[93] Advanced Energy. Navio Match Network. (June), 2015.

[94] R. R.J. Gagné and A. Cantin. Investigation of an rf plasma with symmetrical and asymmetrical electrostatic probes. *Journal of Applied Physics*, 43(6):2639–2647, 1972.

[95] T.E. Sheridan, M. J. Goeckner, and J. Goree. Observation of two-temperature electrons in a sputtering magnetron plasma. *Journal of Vacuum Science & Technology A: Vacuum, Surfaces, and Films*, 9(3):688–690, 1991.

[96] V. A. Godyak, R. B. Piejak, and B. M. Alexandrovich. Electron energy distribution function measurements and plasma parameters in inductively coupled argon plasma. *Plasma Sources Science and Technology*, 11(4):525, 2002.

[97] M.B. Hopkins. Langmuir probe measurements in the gaseous electronics conference rf reference cell. *Journal of research of the National Institute of Standards and Technology*, 100(4):415, 1995.

[98] L. J. Overzet and M. B. Hopkins. Spatial variations in the charge density of argon discharges in the gaseous electronics conference reference reactor. *Applied physics letters*, 63(18):2484–2486, 1993.

[99] D.A. Kondratyev and L.A. Vainshtein. Calculation of electron impact excitation and ionization cross sections for light elements.

[100] A. A. Schekochihin and S. C. Cowley. Turbulence, magnetic fields, and plasma physics in clusters of galaxies. *Physics of Plasmas*, 13(5), 2006.

[101] D. Ryu, H. Kang, J. Cho, and S. Das. Turbulence and magnetic fields in the large-scale structure of the universe. *Science*, 320(5878):909–912, 2008.

[102] E. G. Zweibel and C. Heiles. Magnetic fields in galaxies and beyond. *Nature*, 385(6612):131, 1997.

[103] A. Marcowith, A. Bret, A. Bykov, M. E. Dieckman, L. OC. Drury, B. Lembège, M. Lemoine, G. Morlino, G. Murphy, G. Pelletier, I. Plotnikov, B. Reville, M. Riquelme, L. Sironi, and A. Stockem Novo. The microphysics of collisionless shock waves. *Reports on progress in physics. Physical Society (Great Britain)*, 79(4):046901, 2016.

[104] R. J. van Weeren, Huub J. A. Röttgering, M. Brüggen, and M. Hoeft. Particle acceleration on megaparsec scales in a merging galaxy cluster. *Science*, 330(6002):347, 2010.

[105] R. Blandford and D. Eichler. Particle acceleration at astrophysical shocks: A theory of cosmic ray origin. *Physics Reports*, 154(1):1–75, 1987.

[106] N. L. Kugland, D. D. Ryutov, P-Y. P.-Y. Chang, R. P. Drake, G. Fiksel, D. H. Froula, S. H. Glenzer, G. Gregori, M. Grosskopf, M. Koenig, Y. Kuramitsu, C. Kuranz, M. C. Levy, E. Liang, J. Meinecke, F. Miniati, T. Morita, A. Pelka, C. Plechaty, R. Presura, A. Ravasio, B. A. Remington, B. Reville, J. S. Ross, Y. Sakawa, A. Spitkovsky, H. Takabe, and H-S. H.-S. Park. Self-organized electromagnetic field structures in laser-produced counter-streaming plasmas. *Nature Physics*, 8(11):809–812, 2012.

[107] H. S. Park, C. M. Huntington, F. Fiuza, R. P. Drake, D. H. Froula, G. Gregori, M. Koenig, N. L. Kugland, C. C. Kuranz, D. Q. Lamb, M. C. Levy, C. K. Li, J. Meinecke, T. Morita, R. D. Petrasso, B. B. Pollock, B. A. Remington, H. G. Rinderknecht, M. Rosenberg, J. S. Ross, D. D. Ryutov, Y. Sakawa, A. Spitkovsky, H. Takabe, D. P. Turnbull, P. Tzeferacos, S. V. Weber, and A. B. Zylstra. Collisionless shock experiments with lasers and observation of Weibel instabilities. *Physics of Plasmas*, 22(5), 2015.

[108] G. Gregori, A. Ravasio, C. D. Murphy, K. Schaar, A. Baird, A. R. Bell, A. Benuzzi-Mounaix, R. Bingham, C. Constantin, R. P. Drake, M. Edwards, E. T. Everson, C. D. Gregory, Y. Kuramitsu, W. Lau, J. Mithen, C. Niemann, H.-S. Park, B. A. Remington, B. Reville, A. P. L. Robinson, D. D. Ryutov, Y. Sakawa, S. Yang, N. C. Woolsey, M. Koenig, and F. Miniati. Generation of scaled protogalactic seed magnetic fields in laser-produced shock waves. *Nature*, 481(7382):480–483, 2012.

[109] C. Niemann, W. Gekelman, C. G. Constantin, E. T. Everson, D. B. Schaeffer, A. S. Bondarenko, S. E. Clark, D. Winske, S. Vincena, B. Van Compernolle, and P. Pribyl. Observation of collisionless shocks in a large current-free laboratory plasma. *Geophysical Research Letters*, 41(21):7413–7418, 2014.

[110] E. T. Everson, P. Pribyl, C. G. Constantin, A. Zylstra, D. Schaeffer, N. L. Kugland, and C. Niemann. Design, construction, and calibration of a three-axis, high-frequency magnetic probe (B-dot probe) as a diagnostic for exploding plasmas. *Review of Scientific Instruments*, 80(11):1–8, 2009.

[111] F. C. Jahoda, F. L. Ribe, and G. A. Sawyer. Zeeman-effect magnetic field measurement of a high-temperature plasma. *Physical Review*, 131(1):24–29, 1963.

[112] E. A. McLean, J. A. Stamper, C. K. Manka, H. R. Griem, D. W. Droemer, and B. H. Ripin. Observation of magnetic fields in laser-produced plasma using the Zeeman effect. *Physics of Fluids*, 27(5):1327, 1984.

[113] I. H. Hutchinson. Principles of Plasma Diagnostics: Second Edition. *Plasma Physics and Controlled Fusion*, 44(12):2603–2603, 2002.

[114] J. O. Stenflo. The Hanle effect and the diagnostics of turbulent magnetic fields in the solar atmosphere. *Solar Physics*, 80(2):209–226, 1982.

[115] R. Presura. Hanle effect as candidate for measuring magnetic fields in laboratory plasmas. *Review of Scientific Instruments*, 83(10), 2012.

[116] S. E. Clark, D. B. Schaeffer, A. S. Bondarenko, E. T. Everson, C. G. Constantin, and C. Niemann. Magnetic field measurements in low density plasmas using paramagnetic Faraday rotator glass. *Review of Scientific Instruments*, 83(10):1–4, 2012.

[117] W. S. Przybysz, J. Ellis, S. Chakraborty Thakur, A. Hansen, R. A. Hardin, S. Sears, and E. E. Scime. A magneto-optic probe for magnetic fluctuation measurements. *Review of Scientific Instruments*, 80(10):1–4, 2009.

[118] S. Fujioka, Z. Zhang, K. Ishihara, K. Shigemori, Y. Hironaka, T. Johzaki, A. Sunahara, N. Yamamoto, H. Nakashima, T. Watanabe, H. Shiraga, H. Nishimura, and H. Azechi. Kilotesla magnetic field due to a capacitor-coil target driven by high power laser. *Scientific Reports*, 3:1170, 2013.

[119] A. B. Villaverde, D. A. Donatti, and D. G. Bozinis. Terbium gallium garnet Verdet constant measurements with pulsed magnetic field. *Journal of Physics C: Solid State Physics*, 11(12):L495—-L498, 2001.

[120] David Salzmann. *Atomic physics in hot plasmas*, volume 97. Oxford University Press on Demand, 1998.

[121] N. Larbi-Terzi, S. Sahal-Bréchot, N. Ben Nessib, and M. S. Dimitrijević. Stark-broadening calculations of singly ionized carbon spectral lines. *Monthly Notices of the Royal Astronomical Society*, 423(1):766–773, 2012.

[122] Johan Holtsmark. Über die verbreiterung von spektrallinien. *Annalen der Physik*, 363(7):577–630, 1919.

[123] S. Redfield and J. L. Linsky. The Structure of the Local Interstellar Medium. IV. Dynamics, Morphology, Physical Properties, and Implications of Cloud-Cloud Interactions. *The Astrophysical Journal*, 673(1999):283, 2008.

[124] E. A. McLean and S. A. Ramsden. Optical interferometric and spectroscopic measurements of electron density in a plasma. *Physical Review*, 140(4A), 1965.

[125] C. E. Shannon. Communication in the presence of noise. *Proceedings of the IRE*, 37(1):10–21, Jan 1949.

[126] R. M. Goldstein, H. A. Zebker, and C. L. Werner. Satellite radar interferometry: Two-dimensional phase unwrapping. *Radio Science*, 23(4):713–720, 1988.

[127] J. M. Huntley. Noise-immune phase unwrapping algorithm. *Appl. Opt.*, 28(16):3268–3270, Aug 1989.

[128] M. Hipp, J. Woisetschlaeger, P. Reiterer, and T. Neger. Digital evaluation of interferograms. *Measurement*, 36(36):5366, 2004.

[129] R. B. Larson. Turbulence and star formation in molecular clouds. *Monthly Notices of the Royal Astronomical Society*, 194(4):809–826, 1981.

[130] P. Padoan, J. Bally, Y. Billawala, M. Juvela, and Å. Nordlund. Supersonic Turbulence in the Perseus Molecular Cloud. *The Astrophysical Journal*, 525:318–329, 1999.

[131] S. Boldyrev. Kolmogorov-Burgers Model for Star-forming Turbulence. *The Astrophysical Journal*, 569(2):841–845, 2002.

[132] Paolo Padoan and Åke Nordlund. The stellar initial mass function from turbulent fragmentation. *The Astrophysical Journal*, 576(2):870, 2002.

[133] A. G. Kritsuk, M. L. Norman, P. Padoan, and R. Wagner. The Statistics of Supersonic Isothermal Turbulence. *The Astrophysical Journal*, 665:416–431, 2007.

[134] C. Federrath. On the universality of supersonic turbulence. *Monthly Notices of the Royal Astronomical Society*, 436(2):1245–1257, 2013.

[135] J. Kim and D. Ryu. Density Power Spectrum of Compressible Hydrodynamic Turbulent Flows. *The Astrophysical Journal*, 630(1):4548, 2005.

[136] P. Padoan, M. Juvela, A. Kritsuk, and M. L. Norman. The Power Spectrum of Supersonic Turbulence in Perseus. *The Astrophysical Journal*, 653:L125, 2006.

[137] P. Padoan, A. Nordlund, A. G. Kritsuk, M. L. Norman, and P. S. Li. Two Regimes of Turbulent Fragmentation and the Stellar Initial Mass Function from Primordial to PresentDay Star Formation. *The Astrophysical Journal*, 661(2):972–981, 2007.

[138] J. M. Burgers. *Some considerations on turbulent flow with shear*. Koninklijke Nederlandse Akademie van Wetenschappen, 1953.

[139] A. I. Saichev and W. A. Woyczynski. Density fields in burgers and kdv–burgers turbulence. *SIAM Journal on Applied Mathematics*, 56(4):1008–1038, 1996.

[140] U. Frisch and J. Bec. *Burgulence*. Springer, 2001.

[141] A.A. Schekochihin, A.B. Iskakov, S.C. Cowley, J.C. McWilliams, M.R.E. Proctor, and T.A. Yousef. Fluctuation dynamo and turbulent induction at low magnetic prandtl numbers. *New Journal of Physics*, 9(8):300, 2007.

[142] B. Knaepen, S. Kassinos, and D. Carati. Magnetohydrodynamic turbulence at moderate magnetic Reynolds number. *Journal of Fluid Mechanics*, 513:199–220, 2004.

[143] D. Meeker. Finite element method magnetics. *FEMM User Manual*, (4.2), 2010.

[144] N. P. Barnes and L. B. Petway. Variation of the verdet constant with temperature of terbium gallium garnet. *JOSA B*, 9(10):1912–1915, 1992.

[145] R . W. P. McWhirter. Review paper a5. data needs, priorities and accuracies for plasma spectroscopy. *Physics Reports*, 37(2):165–209, 1978.

[146] I. Zhuravleva, E. Churazov, A. A. Schekochihin, S. W. Allen, P. Arévalo, A. C. Fabian, W. R. Forman, J. S. Sanders, A. Simionescu, R. Sunyaev, A. Vikhlinin, and N. Werner. Turbulent heating in galaxy clusters brightest in x-rays. *Nature*, 515(7525):85, 2014.

[147] P. F. Goldsmith and W. D. Langer. Molecular cooling and thermal balance of dense interstellar clouds. *The Astrophysical Journal*, 222:881, 1978.

[148] B. G. Elmegreen and J. Scalo. Interstellar turbulence i: observations and processes. *Annu. Rev. Astron. Astrophys.*, 42:211–273, 2004.

[149] A. A. Deshpande, K. S. Dwarakanath, and W. M. Goss. Power Spectrum of the Density of Cold Atomic Gas in the Galaxy toward Cassiopeia A and Cygnus A. *The Astrophysical Journal*, 543(1):227–234, 2000.

[150] A. Rousseau, E. Teboul, and S. Béchu. Comparison between Langmuir probe and microwave autointerferometry measurements at intermediate pressure in an argon surface wave discharge. *Journal of Applied Physics*, 98(8), 2005.

[151] W. J. M. Rankine. On the thermodynamic theory of waves of finite longitudinal disturbance [philos. trans. 160 (1870), part ii, 277–288]. *Classic papers in shock compression science, High-press. Shock Compression Condens. Matter*, pages 133–147, 1998.

[152] Henri Hugoniot. *Mémoire sur la propagation du mouvement dans les corps et spécialement dans les gaz parfaits.* Gauthier-Villars, 1887.